

TURBULENCE-INDUCED RELATIVE VELOCITY OF DUST PARTICLES I: IDENTICAL PARTICLES

LIUBIN PAN

Harvard-Smithsonian Center for Astrophysics, 60 Garden St., Cambridge, MA 02138; lpan@cfa.harvard.edu

AND

PAOLO PADOAN

ICREA & ICC, University of Barcelona, Martí i Franquès 1, E-08028 Barcelona, Spain; ppadoan@icc.ub.edu

Draft version June 12, 2018

ABSTRACT

We study the relative velocity of inertial particles suspended in turbulent flows and discuss implications for dust particle collisions in protoplanetary disks. We simulate a weakly compressible turbulent flow, evolving 14 particle species with friction timescale, τ_p , covering the entire range of scales in the flow. The particle Stokes numbers, St , measuring the ratio of τ_p to the Kolmogorov timescale, are in the range $0.1 \lesssim St \lesssim 800$. Using simulation results, we show that the model by Pan & Padoan (PP10) gives satisfactory predictions for the rms relative velocity between identical particles. The probability distribution function (PDF) of the relative velocity is found to be highly non-Gaussian. The PDF tails are well described by a 4/3 stretched exponential function for particles with $\tau_p \simeq 1 - 2T_L$, where T_L is the Lagrangian correlation timescale, consistent with a prediction based on PP10. The PDF approaches Gaussian only for very large particles with $\tau_p \gtrsim 54T_L$. We split particle pairs at given distances into two types with low and high relative speeds, referred to as continuous and caustic types, respectively, and compute their contributions to the collision kernel. Although amplified by the effect of clustering, the continuous contribution vanishes in the limit of infinitesimal particle distance, where the caustic contribution dominates. The caustic kernel per unit cross section rises rapidly as St increases toward $\simeq 1$, reaches a maximum at $\tau_p \simeq 2T_L$, and decreases as $\tau_p^{-1/2}$ for $\tau_p \gg T_L$.

1. INTRODUCTION

The dynamics of particles of finite inertia suspended in turbulent flows is a fundamental problem with applications ranging from industrial processes (e.g. spray combustion engines) to geophysical flows (e.g., atmospheric clouds). The interaction between turbulence and particles has been studied to understand rain initiation in warm terrestrial clouds (e.g., Pinsky & Khain 1997; Falkovich, Fouxon, & Stepanov 2002; Shaw 2003), cloud evolution in the atmospheres of planets, cool stars and brown dwarfs (e.g., Rossow 1978; Pruppacher & Klett 1997; Freytag et al. 2010; Helling et al. 2011), collisions and growth of dust particles in protoplanetary disks (e.g., Dullemond & Dominik 2005; Zsom et al. 2010, 2011; Birnstiel et al. 2011) and in the interstellar medium (e.g., Ormel et al. 2009).

The evolution of the particle size depends on the particle collision rate which may be significantly enhanced by turbulent motions in the carrier flow, as illustrated by recent numerical and theoretical advances in this field (e.g., Wang et al. 2000; Zhou et al. 2001; Falkovich et al. 2002; Zaichik & Alipchenkov 2003, 2009; Zaichik et al. 2003, 2006; Wilkinson et al. 2005, 2006; Falkovich & Pumis 2007; Gustavsson & Mehlig 2011; Gustavsson et al. 2012). An accurate evaluation of the collision rates requires understanding the effects of two interesting phenomena: the preferential concentration or clustering of inertial particles (e.g., Maxey 1987 and Squires & Eaton 1991) and the turbulence-induced collision velocity. In this work, we will focus on the statistics of turbulence-induced relative velocities, and briefly discuss the role of turbulent clustering on the collision rate (see Pan et al. 2011 for a detailed discussion of turbulent clustering

in the context of planetesimal formation). We restrict our discussion to the relative velocity between same-size particles, usually referred to as the monodisperse case, and will address the general bidisperse case (collisions between particles of different sizes) in a follow-up paper.

The main motivation of our study is to improve the modeling of the evolution of dust particles in protoplanetary disks, which sets the stage for the formation of planetesimals, the likely precursors to fully-fledged planets. For example, the planetesimal formation model by Johansen et al. (2007, 2009, 2011) requires particle growth up to decimeter to meter size, in order to achieve good frictional coupling to the disk rotation and hence the maximum clustering effect by the streaming instability. Cuzzi et al. (2008, 2010) and Chambers (2010) proposed an alternative model of planetesimal formation based on the strong turbulent clustering of chondrule-size particles. Other studies (e.g. Lee et al. 2010) focus on the possibility that small particles settle to the disk midplane, where gravitational instability can result in planetesimal formation (e.g. Goldreich & Ward 1973; Youdin 2011), despite the turbulence stirring caused by the Kelvin-Helmholtz instability induced by the vertical settling of the particles (e.g. Weidenschilling 1980; Chiang 2008).

The evolution of the size distribution of dust particles is controlled by collisions. Small particles tend to stick together when colliding, and thus their size grows by coagulation. As the size increases, the particles become less sticky (Blum & Wurm 2010), and, depending on the collision velocity, the collisions may result in bouncing or fragmentation. A detailed summary of experimental results for the dependence of the collision outcome on the

particle properties (such as the particle size and porosity) and on the collision velocity can be found in Guttler et al. (2010). The coagulation, bouncing and fragmentation processes may lead to a quasi-equilibrium distribution of particle sizes (e.g., Birnstiel et al. 2011; Zsom et al. 2010, 2011). Due to the dependence of the collision outcome on the collision velocity, an accurate evaluation of the turbulence-induced relative velocity is important for modeling the size distribution of dust particles.

Saffman and Turner (1956) studied the relative velocity in the limit of small particles with the particle friction or stopping time, τ_p , much smaller than the Kolmogorov timescale, τ_η , of the turbulent flow. This limit, known as the Saffman-Turner limit, is usually expressed as $St \ll 1$, where the Stokes number is defined as $St \equiv \tau_p/\tau_\eta$. Saffman and Turner (1956) predicted that, at a given distance, r , the relative velocity of identical particles is independent of St , and, at a given St , it scales linearly with r for small r . In the opposite limit of large particles with τ_p larger than the largest timescale of the turbulent flow, Abrahamson (1975) showed that the relative velocity scales with the friction time as $\tau_p^{-1/2}$. A variety of models have been developed to bridge the two limits and to predict the relative velocity for particles of any size, i.e., with τ_p covering the entire scale range of the carrier flow (Williams & Crane 1983, Yuu 1984, Kruis & Kusters 1997, & Alipchenkov 2003, Zaichik et al. 2006, Ayala et al. 2008). Among these models, the formulation of Zaichik and collaborators is particularly impressive, as it examines turbulent clustering and turbulence-induced relative velocity simultaneously. The model prediction for the relative velocity agrees well with simulation results at low resolutions. However, the model lacks a transparent physical picture.

Pan & Padoan (2010) developed a new model for the relative velocity of inertial particles of any size that provides an insightful physical picture of the problem. Their formulation illustrates that the relative velocity of identical particles is determined by the memory of the flow velocity difference along their trajectories in the past. The model also shows that the separation of inertial particle pairs backward in time plays an important role in their relative velocity. The model prediction can correctly reproduce the scaling behaviors of the relative speed in the extreme limits of small and large particles, and was found to successfully match the simulation data of Wang et al. (2000).

Falkovich et al. (2002) discovered an interesting effect, named the sling effect, which provides an important contribution to the collision rate. The basic physical picture of this effect is that inertial particles may be shot out of fluid streamlines with high curvature, causing their trajectories to cross with those of other particles (see Fig. 1 of Falkovich & Pumir 2007). In particular, in flow regions with large negative velocity gradients, fast particles can catch up with the slower ones from behind. The trajectory crossing causes the particle velocity to be multivalued at a given point. This gives rise to folds, usually referred to as caustics, in the momentum-position phase space of the particles (Wilkinson et al. 2006; see Fig. 1 of Gustavsson & Mehlig 2011 for a clear illustration). For small particles with $St \ll 1$, the sling events correspond to high-order statistics of the flow velocity gradient, and

the effect is not reflected in the prediction of Saffman and Turner (1956). The formulations of Falkovich et al. (2002) and Gustavsson & Mehlig (2011) for the collision kernel of $St \lesssim 1$ particles consist of two contributions. Following Wilkinson et al. (2006), we name them as continuous and caustic contributions, corresponding to two types of particle pairs with low and high relative velocities, respectively. In the continuous contribution, the relative speed follows the Saffman-Turner prediction and decreases linearly with the particle distance, r . The contribution is amplified by turbulent clustering. However, the scaling exponents of the relative speed and the degree of clustering suggest that the continuous contribution approaches zero in the limit $r \rightarrow 0$, as pointed out by Hubbard (2012). The caustic contribution to the collision kernel per unit cross section was predicted to be independent of the particle size or distance, r , and is thus expected to dominate at sufficiently small r . The effect of slings or caustics causes a rapid rise in the collision rate as St approaches 1, which has been proposed to be responsible for the initiation of rain shower in terrestrial clouds (Wilkinson et al. 2006). Applying this effect to dust particle collisions in protoplanetary disks, one may expect that the collision rate greatly accelerates as the particle grows past sub-mm to mm size, corresponding to $St \simeq 1$ for typical protoplanetary turbulence conditions.

The recent developments mentioned above have not been considered in coagulation models for dust particles in circumstellar disks. We will show that the general formulation of the collision kernel commonly used in the astrophysical literature for dust coagulation is inaccurate. In particular, the dust coagulation models usually adopt collision velocities from the work of Volk et al. (1980) and its later extensions (e.g., Markiewicz, Mizuno & Volk 1991, Cuzzi and Hogan 2003, and Ormel & Cuzzi 2007), which have a number of limitations. Pan & Padoan (2010) pointed out a weakness in the physical picture of these models. Roughly speaking, these models assume that the velocities of two particles induced by turbulent eddies with turnover time significantly smaller (larger) than τ_p are independent (correlated). As shown by Pan & Padoan (2010), whether the particle velocities contributed by turbulent eddies of a given size are correlated or not also depends on how the eddy size compares to the separation of the particles at the time the eddies were encountered. Therefore, the eddy turnover time is not the only factor that determines the degree of correlation. The role of the particle separation relative to the eddy size is not captured by the approach of Volk et al. We also find that the model of Volk et al. overestimates the relative velocity by a factor of 2 for particles with τ_p on the order of the large eddy turnover time of the turbulent flow.

In this paper, we conduct a 512^3 numerical simulation to study inertial particle dynamics in a hydrodynamic turbulent flow. In the simulated flow, we evolve inertial particles in an extended size range, with τ_p covering the entire scale range of the turbulent flow. To our knowledge, such a systematic simulation of a significant resolution has not been previously conducted in the astrophysical literature. Using the simulation data, we first test the model prediction of Pan & Padoan (2010) for the rms relative velocity of inertial particles as a function of St , and validate the physical picture revealed by

the model. We then apply the Pan & Padoan (2010) model to interpret the probability distribution function (PDF) of the relative velocity. The PDF study is motivated by the importance of the PDF of the collision speed in modeling dust particle collisions (Windmark et al. 2012, Garaud et al. 2013), which determines the fractions of collisions leading to sticking, bouncing or fragmentation. The relative velocity PDF of inertial particles has been shown to be highly non-Gaussian by numerical, experimental and theoretical studies (e.g., Sundaram and Collins 1997, Wang et al. 2000, Gustavsson et al. 2008, Bec et al. 2009, de Jong et al. 2010, Gustavsson & Mehlig 2011, Hubbard 2012). Our simulation further confirms high non-Gaussianity, which should be incorporated into coagulation models for dust particles in protoplanetary disks. We will also investigate the particle collision kernel as a function of St .

Due to the computational cost, the number of particles included in our simulation is limited and only allows to accurately measure the relative velocity statistics at significant particle distances. The distance range explored is $\eta/4 \leq r \leq \eta$ where η is the Kolmogorov scale of the simulated flow. This raises the question concerning the direct applicability of our measured statistics to dust particle collisions. The size of dust particles is many orders of magnitudes smaller than the Kolmogorov scale ($\eta \sim 1$ km) in protoplanetary turbulence. Therefore, dust particles should be viewed as nearly point particles, and one is required to examine the $r \rightarrow 0$ limit in order to model their collisions (Hubbard 2012, 2013). This suggests that the relative velocity measured in our simulation at $r \simeq \eta$ would be distinct from the collision speed of dust particles, unless the statistics have already converged at $\simeq \eta$. We find that the measured relative velocity statistics for particles with $St \gtrsim 10$ actually converge at $r \simeq \eta$, and are thus directly applicable for the collision velocity of dust particles. On the other hand, for small to intermediate particles with $St \lesssim 10$, the measured statistics show an r -dependence in the r range explored in this study. For these particles, an appropriate extrapolation to the $r \rightarrow 0$ limit is needed for applications to dust particle collisions.

In the current paper, we focus on understanding the fundamental physics of turbulence-induced relative velocity at finite distances ($\lesssim 1\eta$). Our theoretical and numerical results provide an important step toward the final goal of estimating the dust particle collision velocity at $r \rightarrow 0$. To underhand the $r \rightarrow 0$ limit, we make an initial and preliminary attempt to separate particle pairs into two types, i.e., continuous and caustic types, which show different scalings with r . In particular, we evaluate the contributions of two types of pairs to the collision kernel and examine their behaviors as $r \rightarrow 0$. A systematical study for the $r \rightarrow 0$ limit is deferred to a future work.

In this work, we will consider the particle dynamics only in statistically homogeneous and isotropic turbulence. This is clearly an idealized situation, considering various complexities in protoplanetary disks. For example, the disk rotation induces large-scale anisotropy, which may have significant effects on the prediction for particles with friction time close to the rotation period. Nevertheless, the idealized problem is a very useful tool to understand the fundamental physics. We also neglect

the vertical settling and radial drift. These processes do not directly affect the relative velocity between identical particles, although they may provide important contributions for particles of different sizes that we address in a follow-up work.

The paper is organized as follows. In §2, we present a simple model for the rms velocity of a single particle, which provides an illustration for our formulation of the particle relative velocity. In §3, we introduce the model of Pan & Padoan (2010) for the relative velocity of nearby particles. Our simulation setup and the statistical properties of the simulated turbulent flow are described in §4. §5 presents simulation results for the one-particle rms velocity. In §6, we test the model prediction of Pan & Padoan (2010) for the rms relative velocity, and discuss in details the probability distribution of the relative velocity as a function of the particle inertia. In §7, we evaluate the collision kernel. The conclusions of our study are summarized in §8.

2. THE VELOCITY OF INERTIAL PARTICLES

The dynamics of inertial particles depends crucially on its friction or stopping timescale, τ_p . To evaluate of the friction timescale, we first need to compare the particle size, a_p , with the mean free path of the gas particles in the carrier flow. If the particle size is larger than the mean free path, the friction timescale is given by the Stokes law $\tau_p = \frac{2}{9} \left(\frac{\rho_d}{\rho} \right) \left(\frac{a_p^2}{\nu} \right)$, where ρ_d ($\simeq 1$ g cm $^{-3}$) is the density of the dust material, ρ is the gas density, and ν is the kinematic viscosity of the flow. On the other hand, if a_p is smaller than the gas mean free path, the particle is in the Epstein regime and $\tau_p = \left(\frac{\rho_d}{\rho} \right) \left(\frac{a_p}{C_s} \right)$, where C_s is the sound speed in the flow. For example, for a typical gas density in protoplanetary discs, $\rho \simeq 10^{-9}$ g cm $^{-3}$, at 1 AU, the mean free path of the gas particles is ~ 1 cm, and thus particles with a_p larger (smaller) than 1 cm are in the Stokes (Epstein) regime.

The velocity, $\mathbf{v}(t)$, of an inertial particle suspended in a turbulent velocity field, $\mathbf{u}(\mathbf{x}, t)$, obeys the equation,

$$\frac{d\mathbf{v}}{dt} = \frac{\mathbf{u}(\mathbf{X}(t), t) - \mathbf{v}}{\tau_p}, \quad (1)$$

where $\mathbf{X}(t)$ is the position of the particle at time t , and $\mathbf{u}(\mathbf{X}(t), t)$ corresponds to the flow velocity “seen” by the particle. Eq. (1) has a formal solution,

$$\mathbf{v}(t) = \frac{1}{\tau_p} \int_{t_0}^t \mathbf{u}(\mathbf{X}(\tau), \tau) \exp\left(-\frac{t-\tau}{\tau_p}\right) d\tau, \quad (2)$$

where it is assumed that $t - t_0 \gg \tau_p$ and the particle has already lost the memory of its initial velocity at t_0 . The formal solution indicates that the velocity of an inertial particle is determined by the memory of the flow velocity along its trajectory within a timescale of $\simeq \tau_p$ in the past.

Although the aim of the present work is the relative velocity of inertial particle pairs, we start with a discussion of the single-particle (or “1-particle”) velocity induced by turbulent motions. We provide a simple model for the 1-particle rms velocity as a function of τ_p . The derivation of this model helps to illustrate our formulation for the relative velocity between two nearby particles.

The 1-particle rms velocity can be calculated using the formal solution of eq. (2). We assume the turbulent flow is statistically stationary, and the particle statistics eventually relax to a steady state. We consider a time when the steady state is already reached and denote this time as time 0. Using eq. (2) at $t = 0$, we have,

$$\langle v_i v_j \rangle = \int_{-\infty}^0 \frac{d\tau}{\tau_p} \int_{-\infty}^0 \frac{d\tau'}{\tau_p} B_{Tij}(\tau, \tau') \exp\left(\frac{\tau}{\tau_p}\right) \exp\left(\frac{\tau'}{\tau_p}\right), \quad (3)$$

where $\langle \cdot \cdot \rangle$ denotes the ensemble average and $B_{Tij}(\tau, \tau') \equiv \langle u_i(\mathbf{X}(\tau), \tau) u_j(\mathbf{X}(\tau'), \tau') \rangle$ is the temporal correlation tensor of the flow velocity along the trajectory, $\mathbf{X}(\tau)$, of the inertial particle. The subscript ‘‘T’’ stands for ‘‘trajectory’’. We changed the lower integration limit (t_0) in eq. (2) to $-\infty$, based on the assumption that the particle dynamics is fully relaxed at time 0 (i.e., $t_0 \ll -\tau_p$).

With statistical stationarity and isotropy, the trajectory correlation tensor can be written as $B_{Tij}(\tau, \tau') = u'^2 \Phi_1(\tau' - \tau) \delta_{ij}$, where u' is the 1D rms velocity of the turbulent flow and the correlation coefficient Φ_1 is a function of the time lag only. The subscript ‘‘1’’ is used to indicate that the correlation is along the trajectory of *one* particle. The correlation coefficient, Φ_1 , is unknown, and a common assumption is to approximate it with the Lagrangian correlation function, Φ_L , of tracer particles (or fluid elements), which has been extensively studied. The assumption is likely valid for small particles, but cannot be justified for large particles on a theoretical basis. We will validate the assumption *a posteriori* using simulation results.

The simplest choice for Φ_L is an exponential function, $\Phi_L(\Delta\tau) = \exp(-|\Delta\tau|/T_L)$, where $\Delta\tau = \tau' - \tau$ is the time lag and T_L the Lagrangian correlation timescale. Setting $B_{Tij} = u'^2 \exp(-|\tau' - \tau|/T_L) \delta_{ij}$ in eq. (3), we have $\langle v_i v_j \rangle = u'^2 \delta_{ij}$, where the 1D rms particle velocity, v' , is given by,

$$v' = u' \left(\frac{T_L}{T_L + \tau_p} \right)^{1/2}. \quad (4)$$

This result shows that the particle rms velocity approaches the flow velocity for $\tau_p \ll T_L$ and decreases as $(T_L/\tau_p)^{1/2}$ for $\tau_p \gg T_L$ (e.g., Abrahamson 1975). In the large particle limit, $\tau_p \gg T_L$, the action of even the largest turbulent eddies on the particle would appear to be random kicks when viewed on a timescale of τ_p . In that case, eq. (1) is essentially a Langevin equation, and the particle motions are similar to Brownian motions. The $\tau_p^{-1/2}$ scaling corresponds to an ‘‘equilibrium’’ between the velocity of these particles and the turbulent motions of the flow.

Numerical simulations have shown that the Lagrangian correlation function, $\Phi_L(\Delta\tau)$, is better fit by a bi-exponential form (e.g., Sawford 1991). A single-exponential form does not reflect the smooth part of the correlation function for $\Delta\tau$ smaller than the Taylor micro timescale, τ_T . The Taylor timescale is defined as $(2u'^2/a^2)^{1/2}$, where a is the rms acceleration of the turbulent velocity field. The bi-exponential form

for $\Phi_L(\Delta\tau)$ is,

$$\Phi_L(\Delta\tau) = \frac{1}{2\sqrt{1-2z^2}} \left\{ (1 + \sqrt{1-2z^2}) \times \exp\left[-\frac{2|\Delta\tau|}{(1 + \sqrt{1-2z^2})T_L}\right] - (1 - \sqrt{1-2z^2}) \times \exp\left[-\frac{2|\Delta\tau|}{(1 - \sqrt{1-2z^2})T_L}\right] \right\}, \quad (5)$$

where the parameter z is defined as $z = \tau_T/T_L$. From the above equation, it is easy to show that $T_L = \int \Phi_L(\Delta\tau) d\Delta\tau$, and the bi-exponential function is smooth, $\simeq 1 - (\Delta\tau/\tau_T)^2$, at $\Delta\tau \ll \tau_T$. In the limit $z \rightarrow 0$, eq. (5) reduces to the single exponential with a timescale of T_L .

Adopting the bi-exponential form, eq. (5), for the trajectory correlation coefficient, Φ_1 , we find that the 1-particle rms velocity is given by,

$$v' = u' \left(\frac{\Omega + z^2/2}{\Omega + \Omega^2 + z^2/2} \right)^{1/2}, \quad (6)$$

where Ω is defined as $\Omega \equiv \tau_p/T_L$. In the limits $\Omega \ll 1$ and $\Omega \gg 1$, eq. (6) has the same behavior as eq. (4) from the single exponential correlation. In fact, the two predictions, eqs. (4) and (6), are close to each other at all values of Ω , differing only by a few percent at $\Omega \simeq 1$. This suggests that, for a given correlation timescale, T_L ($\equiv \int \Phi_L(\Delta\tau) d\Delta\tau$), the integral in eq. (3) is insensitive to the exact function form of $\Phi_1(\Delta\tau)$. We will measure z and T_L using Lagrangian tracer particles in our simulated turbulent flow, and test the predictions, eqs. (4) and (6), against the simulation data.

3. TURBULENCE-INDUCED RELATIVE VELOCITY OF INERTIAL PARTICLES

We briefly review the 2-point Eulerian statistics of the velocity field in fully-developed turbulence, which is crucial to understand the relative velocity of two inertial particles. We consider the structure tensor of a turbulent flow, defined as $S_{ij}(\ell) = \langle \Delta u_i \Delta u_j \rangle$ where $\Delta u_i = u_i(\mathbf{x} + \ell, t) - u_i(\mathbf{x}, t)$ is the velocity increment across a separation ℓ . The statistics of Δu_i is independent of \mathbf{x} and t from the assumption of homogeneity and stationarity. With statistical isotropy, the velocity structure tensor takes the form (e.g., Monin and Yaglom 1975),

$$S_{ij}(\ell) = S_{nn}(\ell) \delta_{ij} + [S_{ll}(\ell) - S_{nn}(\ell)] \frac{\ell_i \ell_j}{\ell^2} \quad (7)$$

where the longitudinal and transverse structure functions, S_{ll} and S_{nn} , are functions of the amplitude, ℓ , but not the direction (ℓ/ℓ) of ℓ . From eq. (7), we see $S_{ll} = S_{ij}(\ell) \ell_i \ell_j / \ell^2 = \langle \Delta u_r^2 \rangle$, where $\Delta u_r = \Delta u_i \ell_i / \ell$ is the radial component of Δu . Similarly, S_{nn} can be written as $S_{nn} = \langle (\Delta u_t)^2 \rangle$ with Δu_t being one of the two components of Δu on the tangential/transverse plane perpendicular to ℓ . The statistical isotropy indicates that the probability distribution of Δu_t is invariant under any rotation about the direction ℓ/ℓ . In incompressible turbulence, which is approximately the case for

gas flows in protoplanetary disks, we have the relation $S_{\text{nn}} = S_{\text{ll}} + \frac{1}{2} \ell d S_{\text{ll}} / d\ell$, which can be derived from the incompressibility condition: $\partial_j S_{ij}(\ell) = 0$ (Monin and Yaglom 1975).

The structure functions exhibit different scaling behaviors in different scale ranges. There are three sub-ranges divided by two length scales, the Kolmogorov length scale, η , and the integral length scale L . The Kolmogorov scale, η , is defined as $\eta = (\nu^3/\bar{\epsilon})^{1/4}$, where ν and $\bar{\epsilon}$ are, respectively, the kinematic viscosity and the average energy dissipation rate in the turbulent flow. It essentially corresponds to the size of the smallest eddies. Scales below η are called the viscous or dissipation range, where the velocity field is laminar and differentiable due to the smoothing effect of the viscosity. In the dissipation range, the velocity difference scales linearly with ℓ , and the longitudinal structure function is $S_{\text{ll}} = \frac{\bar{\epsilon}}{15\nu} \ell^2$. S_{nn} is twice larger, i.e., $S_{\text{nn}} = \frac{2\bar{\epsilon}}{15\nu} \ell^2$, as required by the incompressibility constraint. In the inertial range, $\eta \lesssim \ell \lesssim L$, S_{ll} follows the Kolmogorov scaling, $S_{\text{ll}} = C_K (\bar{\epsilon} \ell)^{2/3}$, where C_K is the Kolmogorov constant. The typical value of C_K is $\simeq 2$. The incompressibility condition gives $S_{\text{nn}} = 4S_{\text{ll}}/3$ in the inertial range. The integral scale, L , is essentially the correlation length of the velocity field. At $\ell \gg L$, the velocity field is uncorrelated, and both $S_{\text{ll}}(\ell)$ and $S_{\text{nn}}(\ell)$ are constant and equal to $2u'^2$ with u' the 1D rms velocity of the flow.

To bridge the scalings of S_{ll} in the three scale ranges, we adopt a connecting formula (Zaichik et al. 2006),

$$S_{\text{ll}} = 2u'^2 \left[1 - \exp\left(-\frac{(\ell/\eta)}{(15C_K)^{3/4}}\right) \right]^{4/3} \times \left[\frac{(\ell/\eta)^4}{(\ell/\eta)^4 + (2u'^2/C_K u_\eta^2)^6} \right]^{1/6}, \quad (8)$$

where u_η is the Kolmogorov velocity scale defined as $(\nu\bar{\epsilon})^{1/4}$. With eq. (8) for S_{ll} , we can obtain S_{nn} using the incompressibility condition (see above). Alternatively, one may adopt a separate connecting formula for S_{nn} (see §4.3).

The goal of this work is to understand the relative velocity of two nearby inertial particles. The relative velocity across a distance, r , equal to the sum of the particle radii corresponds to the speed at which the two particles collide (Saffman and Turner 1956). As mentioned earlier, dust particles in protoplanetary disks are nearly point-like, as their size is much smaller than the Kolmogorov length scale, η . The collision speed of dust particles is therefore the relative velocity at $r \rightarrow 0$. In this paper, we focus on the relative speed at finite distances, $r \lesssim \eta$, and the $r \rightarrow 0$ limit will be examined systematically in a future work.

We label two particles coming together with superscripts (1) and (2). For example, we denote their positions as $\mathbf{X}^{(1)}(t)$ and $\mathbf{X}^{(2)}(t)$, and their velocities as $\mathbf{v}^{(1)}(t)$ and $\mathbf{v}^{(2)}(t)$ (see Fig. 1 for illustration). When the superscripts (1) and (2) are not used, the discussion is general and not referring to a specific particle. At a given time t , we consider the relative velocity $\mathbf{w} \equiv \mathbf{v}^{(2)}(t) - \mathbf{v}^{(1)}(t)$, of particle pairs at a given separation, \mathbf{r} , which corresponds to a constraint $\mathbf{X}^{(2)}(t) - \mathbf{X}^{(1)}(t) = \mathbf{r}$

for the particle positions. We first present a theoretical model for the second-order moment of \mathbf{w} , and then use simulations to explore its full statistics including the probability distribution function (PDF).

Similar to the structure tensor of the flow velocity, we characterize the second-order statistics of the particle relative velocity \mathbf{w} by a structure tensor,

$$S_{\text{pij}} \equiv \langle w_i w_j \rangle = \left\langle \left(v_i^{(2)} - v_i^{(1)} \right) \left(v_j^{(2)} - v_j^{(1)} \right) \right\rangle, \quad (9)$$

which was referred to as the particle velocity structure tensor by Pan and Padoan (2010). Here $\langle \dots \rangle$ denotes the average over all particle pairs at a separation of \mathbf{r} .

Once the particle dynamics is fully relaxed, the particle velocity is expected to possess the same statistical symmetries as the flow, including stationarity, homogeneity and isotropy. With these symmetries, S_{pij} can be written in a similar form as the structure tensor of the flow (eq. 7),

$$S_{\text{pij}}(\mathbf{r}) = \langle w_t^2 \rangle \delta_{ij} + (\langle w_r^2 \rangle - \langle w_t^2 \rangle) \frac{r_i r_j}{r^2}, \quad (10)$$

where $\langle w_r^2 \rangle$ and $\langle w_t^2 \rangle$ are the variances of the radial/longitudinal component, w_r ($\equiv w_i r_i / r$), and a tangential/transverse component, w_t , of the relative velocity, respectively. For particle collisions, we are interested in S_{pij} at small distances only, with r in the dissipation range of the flow. Under the assumption of isotropy, the tangential component, w_t , is expected to be statistically invariant for any rotations about the axis \mathbf{r} . We can thus measure the statistics of the tangential relative velocity by projecting \mathbf{w} into an arbitrary direction on the plane perpendicular to \mathbf{r} .

In the rest of this section, we consider theoretical models for the variances, $\langle w_r^2 \rangle$ and $\langle w_t^2 \rangle$, of the relative velocity, which can be computed from the particle structure tensor S_{pij} . For example, $\langle w_r^2 \rangle = S_{\text{pij}} r_i r_j / r^2$. The 3D variance, $\langle w^2 \rangle$, of the relative velocity, is given by the contraction of the tensor, i.e., $S_{\text{pii}} = \langle w_r^2 \rangle + 2\langle w_t^2 \rangle$. We point out that the relative velocity variances cannot be directly applied to estimate the collision kernel, which depends on $\langle |w_r| \rangle$ or $\langle |\mathbf{w}| \rangle$ (see §7). One may use $\langle w_r^2 \rangle$ to approximately estimate the collision rate by a conversion to $\langle |w_r| \rangle$ under an assumption for the PDF shape of w_r (e.g., Wang et al. 2000).

Furthermore, the 3D variance $\langle w^2 \rangle$ does not accurately reflect the average collisional energy for each collision. As pointed out by Hubbard (2012), a collision-rate weighting is needed to evaluate the average collisional energy per collision. In particular, $\langle w^2 \rangle$ is defined as the variance over all particle pairs at a distance, r . But not all the pairs may give a significant contribution to the collision rate in the $r \rightarrow 0$ limit (see §7.2), and in that case $\langle w^2 \rangle$ does not provide a reliable estimate for the average collision energy for those pairs that dominate the collision rate at $r \rightarrow 0$. Despite these limitations in the practical use of the overall rms (or variance) of the relative speed, its theoretical modeling is an important step toward understanding the fundamental physics. As mentioned earlier, we focus on the monodisperse case with equal-size particles.

3.1. The Limits of Small and Large Particles

We first consider small particles in the Saffman-Turner limit (hereafter the S-T limit). In this limit, the friction timescale, τ_p , is much smaller than the Kolmogorov timescale, τ_η , of the carried flow, which is defined as $\tau_\eta \equiv (\nu/\bar{\epsilon})^{1/2}$. The Kolmogorov timescale is the smallest timescale in a turbulent flow, corresponding to the turnover time of the smallest eddies. Therefore, the velocity of particles with $\tau_p \ll \tau_\eta$ can be approximated by a Taylor expansion of eq. (1), $\mathbf{v}(t) \simeq \mathbf{u}(\mathbf{X}, t) + \tau_p \mathbf{a}(\mathbf{X}, t)$, where $\mathbf{a} = D\mathbf{u}/Dt$ is the acceleration of the local fluid element. Applying the approximation to both particles (1) and (2), we have $\mathbf{w} = (\mathbf{u}^{(2)} - \mathbf{u}^{(1)}) + (\mathbf{a}^{(2)} - \mathbf{a}^{(1)}) \tau_p$, where $\mathbf{u}^{(1,2)} (\equiv \mathbf{u}(\mathbf{X}^{(1,2)}, t))$ and $\mathbf{a}^{(1,2)} (\equiv \mathbf{a}(\mathbf{X}^{(1,2)}, t))$ are the flow velocity and acceleration at the positions of particles (1) and (2), respectively. Saffman and Turner (1956) assumed that the correlation coefficient of the flow accelerations, $\mathbf{a}^{(1)}$, and $\mathbf{a}^{(2)}$, across a small distance, r , is unity, which is equivalent to assuming $\mathbf{a}^{(1)} \simeq \mathbf{a}^{(2)}$. The acceleration terms then cancel out for identical particles, and the particle structure tensor, S_{pij} , is simply equal to the flow structure tensor, S_{ij} , defined in eq. (7). Using the flow structure functions S_{11} and S_{nn} at $r \ll \eta$ in incompressible turbulence, we have the Saffman-Turner formula,

$$\langle w_r^2 \rangle = \frac{1}{15} \frac{\bar{\epsilon}}{\nu} r^2, \quad \langle w_t^2 \rangle = \frac{2}{15} \frac{\bar{\epsilon}}{\nu} r^2, \quad (11)$$

for identical particles with $St \ll 1$. The equation shows that in the S-T limit the relative speed is caused by the flow velocity difference across the particle separation. The effect is usually referred to as the shear contribution¹. From eq. (11), the 3D variance of the relative velocity is given by $\langle w^2(r) \rangle = \frac{\bar{\epsilon}}{3\nu} r^2$.

The S-T formula predicts that the tangential variance of the relative velocity, $\langle w_t^2 \rangle$, is twice larger than that in the radial direction, $\langle w_r^2 \rangle$. Eq. (11) also indicates a constant relative speed at a given separation, r , and a linear scaling with r at a given $St \ll 1$. The accuracy of the Saffman-Turner formula for the small particle limit has been questioned, as it neglects the effect of slings and caustic formation (e.g., Falkovich et al. 2002, Wilkinson et al. 2006). We will test the S-T prediction against our simulation data. In the S-T limit, the particle memory is short and the relative speed is determined largely by the local flow velocity at small scales. The memory effect becomes more important for larger particles with $\tau_p > \tau_\eta$ (see §3.2).

We next consider the other extreme limit, i.e., large particles with τ_p much larger than the Lagrangian correlation time, T_L , of the flow. As discussed in §2, the motions of these particles are similar to Brownian motions, and the velocities of any two particles are statistically independent. This is because the velocity of a large particle has a significant contribution from its memory of the flow velocity long time ago, and the flow velocities “seen” by the two particles at that time were uncorrelated because the particle separation was likely larger than the flow in-

tegral length scale, L . With the independence of $\mathbf{v}^{(1)}$ and $\mathbf{v}^{(2)}$, the particle structure tensor defined in eq. (9) can be written as $S_{pij} = \left[(v'^{(1)})^2 + (v'^{(2)})^2 \right] \delta_{ij}$, where $v'^{(1)}$ and $v'^{(2)}$ are the (1D) rms velocities of particles (1) and (2), respectively. As shown in §2, for particles with $\tau_p \gg T_L$, the rms velocity is given by $\simeq u' (T_L/\tau_p)^{1/2}$. We therefore have (e.g., Abrahamson 1975),

$$\langle w_r^2 \rangle = \langle w_t^2 \rangle = 2u'^2 \frac{T_L}{\tau_p}, \quad (12)$$

for identical particles with $\tau_p \gg T_L$. The equation suggests that the rms relative speed decreases with St as $St^{-1/2}$. The physical picture for the large particle limit is clear, and eq. (12) is thus robust.

In between the two extreme limits are particles in the inertial range, i.e., particles with friction timescale $\tau_\eta \lesssim \tau_p \lesssim T_L$, corresponding to inertial-range scales in the turbulent flow. Unlike the two extreme limits where the velocities of two nearby particles are either highly correlated (small particles) or essentially independent (large particles), the velocity correlation of nearby inertial-range particles is at an intermediate level. We will show that a key physics for the relative velocity of these particles is their memory of the flow velocity difference in the past and the separation of the particle pair backward in time.

As mentioned in the Introduction, a variety of models for the particle relative velocity covering the whole range of particle sizes have been developed (e.g., Volk et al. 1980, Ormel & Cuzzi 2007, Zaichik & Alipchenkov 2003, Zaichik et al. 2006, and Pan & Padoan 2010). The models listed here all predict a $St^{1/2}$ scaling for inertial-range particles in turbulent flows with an extended inertial range. The $St^{1/2}$ scaling may be obtained by a simple scale-invariant assumption for inertial-range particles (e.g., Hubbard 2012), which we argue, however, does not provide a sufficient physical picture to understand the full statistics, e.g., the PDF shape, of the relative velocity. The models of Zaichik and collaborators and Pan and Padoan (2010) can reproduce both the S-T limit (eq. (11)) and the large particle limit (eq. (12)). We will focus on the model of Pan and Padoan (2010), which provides a clearer physical picture than that of Zaichik et al. The physical differences between various models have been summarized in Pan and Padoan (2010).

3.2. The Model of Pan and Padoan (2010)

We review the formulation and the physical picture of the model by Pan & Padoan (2010; hereafter PP10) for the relative velocity of identical particles. The PP10 model aimed at predicting the variance or rms of the relative velocity. As mentioned earlier, although the rms relative velocity does not directly enter the collision kernel or the average collisional energy per collision, its theoretical modeling is essential for understanding the underlying physics. For example, the physical picture revealed by the PP10 model is very successful in the interpretation of the probability distribution of the relative velocity (§6.2), which, in turn, is helpful for the evaluation of the collision kernel (§7). The main idea of the PP10 model was to compute the particle velocity structure tensor,

¹ The term “shear contribution” is as opposed to the “acceleration contribution” from the acceleration terms mentioned above, which do not vanish for particles of different sizes. The acceleration contribution in the bidisperse case will be discussed in a separate paper.

$S_{p_{ij}}(\mathbf{r})$, using the formal solution (eq. (2)) for the particle velocity. Applying eq. (2) to the velocities of particles (1) and (2) at $t = 0$, we have,

$$v_i^{(2)} - v_i^{(1)} = \frac{1}{\tau_p} \int_{-\infty}^0 [u_i^{(2)}(\tau) - u_i^{(1)}(\tau)] \exp\left(\frac{\tau}{\tau_p}\right) d\tau, \quad (13)$$

where $\mathbf{u}^{(1,2)}(\tau) (\equiv \mathbf{u}(\mathbf{X}^{(1,2)}(\tau), \tau))$ are the flow velocities “seen” by the two particles at time τ . Again we have changed the lower integration limit in the formal solution, eq. (2), to $-\infty$.

Inserting eq. (13) into the definition (eq. (9)) of $S_{p_{ij}}$, it is straightforward to find that,

$$S_{p_{ij}}(\mathbf{r}) = \int_{-\infty}^0 \frac{d\tau}{\tau_p} \int_{-\infty}^0 \frac{d\tau'}{\tau_p} S_{T_{ij}}(\mathbf{r}; \tau, \tau') \times \exp\left(\frac{\tau}{\tau_p}\right) \exp\left(\frac{\tau'}{\tau_p}\right), \quad (14)$$

where $S_{T_{ij}}$, named the trajectory structure tensor by PP10, is defined as,

$$S_{T_{ij}}(\mathbf{r}, \tau, \tau') = \left\langle [u_i^{(2)}(\tau) - u_i^{(1)}(\tau)] [u_j^{(2)}(\tau') - u_j^{(1)}(\tau')] \right\rangle. \quad (15)$$

This tensor represents the correlation of the flow velocity differences on the trajectories of the two particles at two times τ and τ' . $S_{T_{ij}}$ depends on the separation, \mathbf{r} , through the constraint that $\mathbf{X}^{(2)}(0) - \mathbf{X}^{(1)}(0) = \mathbf{r}$. Eq. (14) is in close analogy with eq. (3) for the 1-particle velocity. Here the trajectory structure tensor, $S_{T_{ij}}$, replaces the trajectory correlation tensor, $B_{T_{ij}}$, in eq. (3).

The physical meaning of eqs. (13) and (14) is clear: the relative velocity of two identical inertial particles is controlled by the particles’ memory of the flow velocity difference within a friction timescale, $\sim \tau_p$, in the past. The physical picture is illustrated in Fig. 1. The trajectory structure tensor, $S_{T_{ij}}$, is unknown, and we model it using the approach of PP10.

Since the flow velocity difference scales with the distance, $S_{T_{ij}}$ has an indirect dependence on the particle separation at τ and τ' . We denote the particle separation at τ as $\mathbf{d}(\tau) (\equiv \mathbf{X}^{(2)}(\tau) - \mathbf{X}^{(1)}(\tau))$. The vector \mathbf{d} is stochastic because of the random dispersion of the particle pair by turbulent motions. $S_{T_{ij}}$ also has a dependence on the time lag ($\tau' - \tau$). This dependence is associated with the temporal correlation of turbulent structures or eddies encountered by the two particles between τ and τ' , and the correlation time is essentially the turnover time of these eddies. To estimate $S_{T_{ij}}$, we consider the (indirect) spatial dependence on the particle separation and the temporal dependence on the time lag separately.

We use a typical particle separation $\mathbf{R}(\tau, \tau')$ between τ and τ' to model the spatial dependence. Like $\mathbf{d}(\tau)$ and $\mathbf{d}(\tau')$, $\mathbf{R}(\tau, \tau')$ is also a random vector. We approximate the dependence on the separation by the Eulerian structure tensor of the flow velocity, $S_{ij}(\mathbf{R})$, defined in eq. (7). We denote as $\Phi_2(\tau' - \tau, R)$ the temporal correlation of the flow structure at the scale R . Φ_2 is expected to be an even function of the time lag and is normalized to unity, $\Phi_2(0, R) = 1$, at zero time lag. To distinguish from the temporal correlation, $\Phi_1(\tau' - \tau)$, along the trajectory of a single particle (see §2), we have used a subscript “2” here

for the two-particle case. The trajectory structure tensor is then modeled as the product of the two dependences (PP10),

$$S_{T_{ij}}(\mathbf{r}; \tau, \tau') \simeq \langle S_{ij}(\mathbf{R}) \Phi_2(\tau' - \tau, R) \rangle_{\mathbf{R}} \quad (16)$$

where $\langle \dots \rangle_{\mathbf{R}}$ denotes the average over the statistics of the random vector, \mathbf{R} . This average is over the probability distributions of both the amplitude, R , and the direction of \mathbf{R} . Eq. (16) implicitly assumes the statistical independence of the velocity difference, $\Delta \mathbf{u}$, seen by the two particles from their separation, \mathbf{R} . Rigorously, the amplitudes of $\Delta \mathbf{u}$ and \mathbf{R} may have a correlation. If the particle pair encounters an eddy with a larger velocity, the particle separation tends to be larger. For example, if R is in the inertial range of the flow, $\Delta u \simeq \epsilon_R^{1/3} R^{1/3}$ from the refined similarity hypothesis (Kolmogorov 1962), where ϵ_R is the average dissipation rate over the scale R seen by the particle pair. A positive correlation is expected between the fluctuations in ϵ_R and R . Eq. (16) neglects this correlation and may underestimate $S_{T_{ij}}$ and hence the particle relative velocity.

The Φ_2 term in eq. (16) does not depend on the direction of \mathbf{R} , so one can first take the angular average of $S_{ij}(\mathbf{R})$ and then average the entire term over the PDF of the amplitude, R . The latter cannot be exactly performed because the PDF of R is unknown. With some simple estimates, PP10 argued that simply using the rms of R to evaluate $S_{T_{ij}}$ (instead of averaging over the PDF of R) only causes a small difference ($\simeq 10\%$) in the model prediction. Following PP10, we ignore the PDF of R and insert the rms of R to evaluate $S_{T_{ij}}$. For the simplicity of notation, we use R to denote the rms particle distance in between τ and τ' in the rest of the paper. A similar notation is adopted for $d(\tau)$ and $d(\tau')$, which will denote the rms separations at τ and τ' , respectively. We approximate R by the geometric average of $d(\tau)$ and $d(\tau')$,

$$R(\tau, \tau') = [d(\tau)d(\tau')]^{1/2}. \quad (17)$$

The rms separation $d(\tau)$ as a function of time τ will be discussed in §3.2.3.

With the above assumptions, the trajectory structure tensor is modeled as,

$$S_{T_{ij}}(\mathbf{r}; \tau, \tau') \simeq \langle S_{ij}(\mathbf{R}) \rangle_{\text{ang}} \Phi_2(\tau' - \tau, R). \quad (18)$$

The angular average of S_{ij} over the direction of \mathbf{R} will be carried out in §3.2.2. In eq. (18), the dependence of $S_{T_{ij}}$ on \mathbf{r} is through the dependence of $d(\tau)$, $d(\tau')$ and R on \mathbf{r} . We refer to \mathbf{r} as the “initial” separation, although it actually corresponds to the current or final separation of the two particles. Our formulation indicates that the separation of particle pairs backward in time is crucial for the prediction of the particle relative speed.

Inserting eq. (18) into eq. (14) gives the PP10 model for the particle structure tensor,

$$S_{p_{ij}}(\mathbf{r}) = \int_{-\infty}^0 \frac{d\tau}{\tau_p} \int_{-\infty}^0 \frac{d\tau'}{\tau_p} \langle S_{ij}(\mathbf{R}) \rangle_{\text{ang}} \times \Phi_2(\tau' - \tau, R) \exp\left(\frac{\tau}{\tau_p}\right) \exp\left(\frac{\tau'}{\tau_p}\right). \quad (19)$$

We will numerically compute this double integral after evaluating or modeling the angular average, the temporal

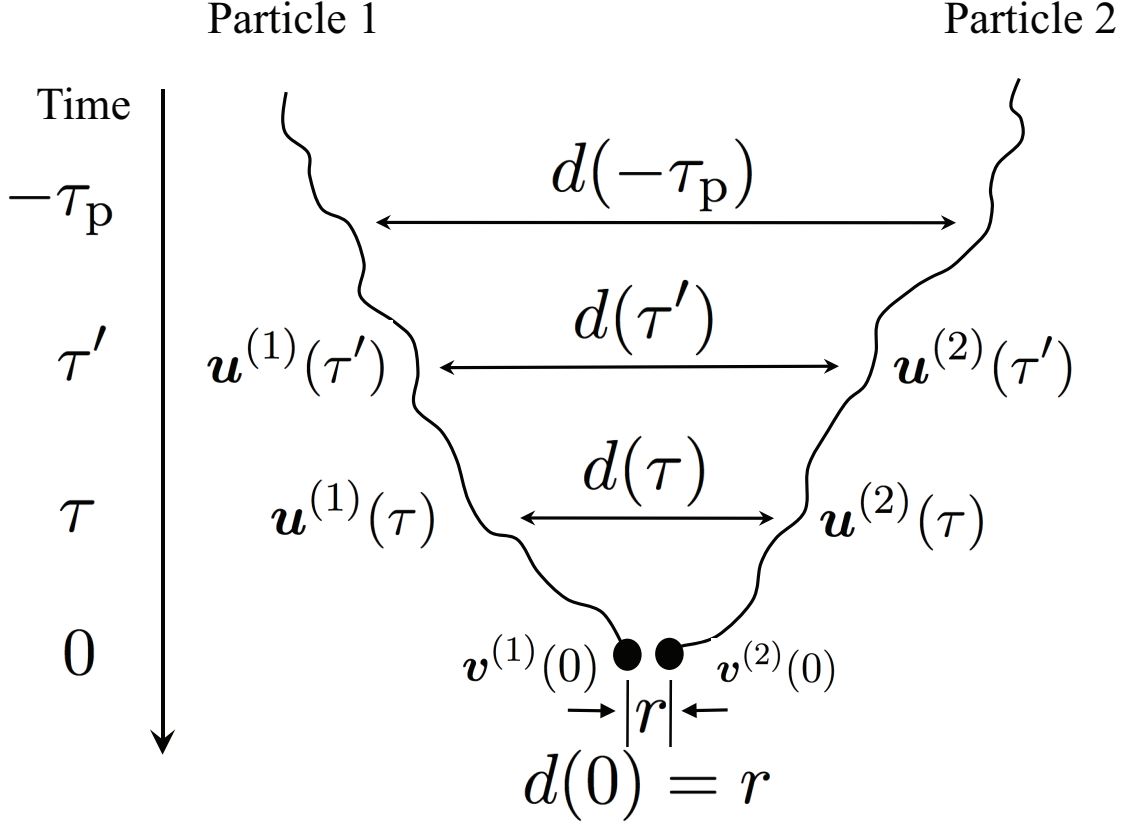


FIG. 1.— Schematic figure illustrating the physical picture of the PP10 model for the relative velocity of two equal-size particles. At time 0, the separation of particles (1) and (2) is r . The velocity, $\mathbf{v}(0)$, of each particle at $t = 0$, is determined by its memory of the flow velocity, $\mathbf{u}(\tau)$, along the particle trajectory in the past. The relative velocity of the two particles mainly depends on the flow velocity difference, $\mathbf{u}^{(2)}(\tau) - \mathbf{u}^{(1)}(\tau)$, they “saw” within about a friction timescale τ_p in the past, i.e., $-\tau_p \lesssim \tau \leq 0$. The flow velocity difference at a given time τ scales with the particle separation, $d(\tau)$. The particle separation satisfies the “initial” constraint $d(0) = r$ and increases backward in time. Due to particle inertia, a roughly ballistic separation is expected within a friction timescale. The trajectories plot here reflect a more-or-less linear separation of the two particles. The particle relative velocity also depends on the temporal correlation of the flow velocity differences the two particles “saw” at different times, say τ and τ' . The correlation timescale is associated with the turnover time of turbulent eddies encountered by the two particles.

correlation and the particle separation backward in time.

A simplification of the PP10 model is to set \mathbf{R} to one of two distances, $\mathbf{d}(\tau)$ or $\mathbf{d}(\tau')$, instead of their geometric average. We find that replacing \mathbf{R} in eq. (19) by either $\mathbf{d}(\tau)$ or $\mathbf{d}(\tau')$ leads to equivalent model prediction for the particle relative speed. This is because Φ_2 in eq. (19) is an even function of $\Delta\tau (\equiv \tau' - \tau)$, and the product of the two exponential cutoffs are invariant under the exchange of τ and τ' . If one sets $\mathbf{R} = \mathbf{d}(\tau)$ in eq. (19), the integral over τ' can be isolated, yielding,

$$S_{p_{ij}} = \frac{1}{\tau_p} \int_{-\infty}^0 \langle S_{ij}(\mathbf{d}(\tau)) \rangle_{\text{ang}} F(\tau) \exp\left(\frac{\tau}{\tau_p}\right) d\tau, \quad (20)$$

where the angular average is over the direction of $\mathbf{d}(\tau)$ and the function $F(\tau)$ is defined as,

$$F(\tau) = \frac{1}{\tau_p} \int_{-\infty}^0 \Phi_2(\tau' - \tau, d(\tau)) \exp\left(\frac{\tau'}{\tau_p}\right) d\tau'. \quad (21)$$

The factor $F(\tau)$ may be roughly viewed as a response function of the particle pair to turbulent eddies at the scale $d(\tau)$. Although not indicated explicitly, the factor $F(\tau)$ also depends on r through its dependence on $d(\tau)$. We will refer to eqs. (20) and (21) as the simplified model. In the simplified model, $F(\tau)$ can be integrated analyti-

cally using assumed function forms of Φ_2 in §3.2.1, and one only needs to numerically solve a single integral in eq. (20). On the other hand, for the original PP10 model, one must numerically evaluate the double integral in eq. (19).

3.2.1. The temporal correlation Φ_2

To estimate the temporal correlation, Φ_2 , in the trajectory structure tensor, $S_{T_{ij}}$, we first consider a special case where the particle separation, R , is much larger than the integral length scale, L , of the flow. In this case, the flow velocities, $\mathbf{u}^{(1)}$ and $\mathbf{u}^{(2)}$, “seen” by the two particles are independent, and $S_{T_{ij}}$ can be written as $\langle u_i^{(1)}(\tau) u_j^{(1)}(\tau') \rangle + \langle u_i^{(2)}(\tau) u_j^{(2)}(\tau') \rangle$ (see eq. (9)). Both terms correspond to the trajectory correlation tensor $B_{T_{ij}}$ defined below eq. (3) in §2, and for identical particles the two terms are equal. Therefore, for $R \gg L$, $\Phi_2(\Delta\tau, R)$ is the same as the temporal correlation coefficient, $\Phi_1(\Delta\tau)$, along the trajectory of one particle.

In §2, we approximated Φ_1 by the Lagrangian correlation function, Φ_L . Using the approximation again, we have $\Phi_2(\Delta\tau, \ell) = \Phi_1(\Delta\tau) \simeq \Phi_L(\Delta\tau)$ for $\ell \gg L$. Two function forms, single- and bi-exponential, were adopted for Φ_L in §2. With the single-exponential form, we set $\Phi_2(\Delta\tau, \ell) = \exp(-|\Delta\tau|/T_L)$ for $\ell \gg L$. An extension of

this function to smaller scales gives,

$$\Phi_2(\Delta\tau, \ell) = \exp\left(-\frac{|\Delta\tau|}{T(\ell)}\right), \quad (22)$$

where $T(\ell)$ is essentially the correlation time or lifetime of turbulent eddies of size ℓ . For $\ell \gg L$, we set $T(\ell) = T_L$.

At smaller ℓ , $T(\ell)$ can be estimated using the velocity scalings in the turbulent flow. For ℓ in the inertial range, we obtain $T(\ell)$ by dividing ℓ by the amplitude of the turbulent velocity fluctuations at this scale, which is $(S_{11}(\ell) + 2S_{nn}(\ell))^{1/2}$. Using the Kolmogorov scaling for structure functions, we have $T(\ell) = C_T \bar{\epsilon}^{-1/3} \ell^{2/3}$, where $C_T = (11C_K/3)^{-1/2} = 0.52C_K^{-1/2}$. The factor, $11/3$, is from the incompressibility relation $S_{nn} = 4S_{11}/3$ in the inertial range. Since the Kolmogorov constant C_K is $\simeq 2$, we set $C_T \simeq 0.4$. A similar value of C_T was adopted by Zaichik & Alipchenkov (2003). In the viscous range with $\ell \ll \eta$, the flow velocity difference goes linearly with ℓ , and $T(\ell)$ is expected to be constant. Lundgren (1981) predicted that $T(\ell) = \sqrt{5}\tau_\eta$ for $\ell \ll \eta$, which was later confirmed by numerical simulations of Girimaji & Pope (1990). We thus take $T(\ell) = \sqrt{5}\tau_\eta$ for $\ell \ll \eta$ in our model. We will use the bridging formula for $T(\ell)$ from Zaichik et al. (2006),

$$T(\ell) = T_L \left[1 - \exp\left(-\left(\frac{C_T}{\sqrt{5}}\right)^{3/2} (\ell/\eta)\right) \right]^{-2/3} \times \left[\frac{(\ell/\eta)^4}{(\ell/\eta)^4 + (T_L/(C_T\tau_\eta))^6} \right]^{1/6}, \quad (23)$$

which satisfies the scalings of $T(\ell)$ in different scale ranges.

One may also adopt a bi-exponential form for $\Phi_2(\Delta\tau, \ell)$ based on eq. (5) for the Lagrangian correlation function Φ_L (see §2). Replacing T_L in eq. (5) by $T(\ell)$ gives,

$$\Phi_2(\Delta\tau, \ell) = \frac{1}{2\sqrt{1-2z^2}} \left\{ (1 + \sqrt{1-2z^2}) \times \exp\left[-\frac{2|\Delta\tau|}{(1 + \sqrt{1-2z^2})T(\ell)}\right] - (1 - \sqrt{1-2z^2}) \times \exp\left[-\frac{2|\Delta\tau|}{(1 - \sqrt{1-2z^2})T(\ell)}\right] \right\}. \quad (24)$$

This bi-exponential form for $\Phi_2(\Delta\tau, \ell)$ was used in all the calculations in PP10. We will compute the predictions of the PP10 model using both the single- and bi-exponential correlation functions. We find the results from the two cases are close to each other, suggesting that the double integral in eq. (19) is insensitive to the function form of $\Phi_2(\Delta\tau, \ell)$. After the integration, the dependence on $\Phi_2(\Delta\tau, \ell)$ is essentially condensed to a dependence on the timescale $T(\ell)$. This is similar to the case of the one-particle velocity, which is insensitive to the form of $\Phi_1(\Delta\tau)$ (see §2). PP10 also considered the possible dependence of the parameter z on the length scale ℓ . It was found that including a reasonable length scale dependence of z barely changes the model prediction. We

will set z to be constant in this study.

We next consider the simplified model represented by eqs. (20) and (21). With a single-exponential Φ_2 (eq. (22)), the response factor $F(\tau)$ defined in eq. (21) can be integrated analytically,

$$F(\tau) = \frac{T(d)}{T(d) - \tau_p} \exp\left(\frac{\tau}{T(d)}\right) + \frac{2\tau_p T(d)}{\tau_p^2 - T^2(d)} \exp\left(\frac{\tau}{\tau_p}\right). \quad (25)$$

Since τ is negative, $F(\tau)$ is dominated by the first term if $T(d) \gg \tau_p$, and it approaches $\exp(\tau/T(d))$ in that limit. On the other hand, for $T(d) \ll \tau_p$, the leading term is $\frac{2T(d)}{\tau_p} \exp(\tau/\tau_p)$. Note that eq. (25) does not diverge at $T(d) = \tau_p$. Applying the L'Hospital's rule shows that it converges to $(\frac{1}{2} - \frac{\tau}{\tau_p}) \exp(\tau/\tau_p)$, as $T(d) \rightarrow \tau_p$. Therefore, when numerically integrating eq. (20), we set $F(\tau) = (\frac{1}{2} - \frac{\tau}{\tau_p}) \exp(\tau/\tau_p)$ for $T(d)$ around τ_p .

With the bi-exponential temporal correlation, eq. (24), the response factor, $F(\tau)$, can also be integrated analytically. The integration is straightforward, but the resulting function for $F(\tau)$ is complicated and is thus omitted here. The predictions of the simplified model with single- and bi-exponential $\Phi_2(\Delta\tau, \ell)$ are also found to be close to each other.

3.2.2. Averaging over the direction of \mathbf{R}

We evaluate the angular average of $S_{ij}(\mathbf{R})$ over the direction of \mathbf{R} . It follows from eq. (7) that $S_{ij}(\mathbf{R}) = S_{nn}(R)\delta_{ij} + [S_{11}(R) - S_{nn}(R)]R_i R_j / R^2$. The contraction of the tensor is $S_{ii}(\mathbf{R}) = S_{11}(R) + 2S_{nn}(R)$, which does not have a direct dependence on the direction of \mathbf{R} . Therefore, to predict the 3D rms relative speed, we do not need to perform the angular average. However, for the radial and tangential components, one must make an assumption for the direction of \mathbf{R} and compute the angular average for the term $\propto R_i R_j / R^2$.

In PP10, we assumed that the direction of the separation change, $\Delta\mathbf{R} \equiv \mathbf{R} - \mathbf{r}$, caused by turbulent dispersion is completely random or isotropic. One can then insert $\mathbf{R} = \Delta\mathbf{R} + \mathbf{r}$ into $S_{ij}(\mathbf{R})$ and take the average over the direction of $\Delta\mathbf{R}$. From the assumed isotropy of $\Delta\mathbf{R}$, we have $\langle r_i \Delta R_j \rangle = 0$ and $\langle \Delta R_i \Delta R_j \rangle_{\text{ang}} = \frac{1}{3}(R^2 - r^2)\delta_{ij}$, and hence $\langle R_i R_j \rangle_{\text{ang}} \simeq r_i r_j + \frac{1}{3}(R^2 - r^2)\delta_{ij}$ (see PP10). The angular average $\langle S_{ij}(\mathbf{R}) \rangle_{\text{ang}}$ is then given by²,

$$\langle S_{ij}(\mathbf{R}) \rangle_{\text{ang}} = \delta_{ij} \left[\left(\frac{1}{3} - \frac{r^2}{3R^2} \right) S_{11}(R) + \left(\frac{2}{3} + \frac{r^2}{3R^2} \right) \times S_{nn}(R) \right] + \left[S_{11}(R) - S_{nn}(R) \right] \frac{r_i r_j}{R^2}. \quad (26)$$

The equation approaches $S_{ij}(\mathbf{r})$ in the limit $R \rightarrow r$. PP10 showed that eq. (26) reproduces the S-T formula for the radial and tangential relative speeds. In the limit $R \gg r$, we have $\langle S_{ij}(\mathbf{R}) \rangle_{\text{ang}} \simeq \frac{1}{3} [S_{11}(R) + 2S_{nn}(R)]$.

² Rigorously, the amplitude, R , of \mathbf{R} and hence $S_{11}(R)$ and $S_{nn}(R)$ have a dependence on the direction of $\Delta\mathbf{R}$. However, the average of these quantities over the direction of $\Delta\mathbf{R}$ is complicated and cannot be done analytically. For simplicity, we kept R , S_{11} and S_{nn} fixed, and only accounted for the angular average of $R_i R_j$.

Here we make a simpler assumption than PP10: we take the direction of \mathbf{R} (rather than $\Delta\mathbf{R}$) to be isotropic. This means $\langle R_i R_j / R^2 \rangle_{\text{ang}} = \frac{1}{3} \delta_{ij}$, and we have,

$$\langle S_{ij}(\mathbf{R}) \rangle_{\text{ang}} = \frac{1}{3} [S_{\parallel}(R) + 2S_{\text{nn}}(R)] \delta_{ij}, \quad (27)$$

which suggests that the particle structure tensor $S_{\text{pij}} \propto \delta_{ij}$ (see eq. (19)), and hence $\langle w_r^2 \rangle = \langle w_t^2 \rangle$ (see eq. (10)) for particles of any size. A comparison of the two assumptions, eqs. (26) and (27), shows that they differ only at $R \lesssim r$.

As expected, the contraction $\langle S_{ii}(R) \rangle_{\text{ang}}$ of both eq. (26) and eq. (27), is equal to $[S_{\parallel}(R) + 2S_{\text{nn}}(R)]$, indicating that the two assumptions give the same prediction for the 3D rms relative velocity. The only difference between the two assumptions is the prediction for the radial and tangential components at $St \lesssim 1$. In §3.2.4, we will compare the model predictions by the two assumptions. The angular average $\langle S_{ij}(\mathbf{d}) \rangle_{\text{ang}}$ in the simplified model (eq. (20)) can be evaluated similarly, and the resulting expressions are in the same form as eqs. (26) and (27) with $d(\tau)$ replacing $R(\tau, \tau')$.

3.2.3. The backward dispersion of particle pairs

We finally specify the (rms) particle separation, $d(\tau)$, as a function of τ . The separation of inertial particle pairs backward in time has not been explored in the literature. Fortunately, Bec et al. (2010) carried out a detailed numerical study of the forward-in-time pair dispersion of inertial particles. Following PP10, we use their results to guide the assumption for the backward dispersion. We first consider the separation behavior of inertial-range particles with $\tau_\eta \lesssim \tau_p \lesssim T_L$.

Bec et al. (2010) found that the separation of inertial particles shows different behaviors at early and late times. At early times, a clear ballistic phase is observed for particles with $St \gtrsim 3$. In this phase, the separation increases linearly with time, and the phase lasts for about a friction timescale. The ballistic behavior is easy to understand: The particle velocity tends to be roughly constant for a memory timescale, τ_p . This also applies to the dispersion backward in time. We thus assume that, for particle pairs at an “initial” distance of r , the separation $d(\tau)$ in the time range $-\tau_p \lesssim \tau \leq 0$ is given by,

$$d^2(\tau) = r^2 + \langle w^2 \rangle \tau^2 \quad (28)$$

where $\langle w^2 \rangle$ is the 3D variance of the particle relative velocity at time 0. The particle relative speed is actually what our model aims to predict. Therefore, the dependence of $d(\tau)$ on $\langle w^2 \rangle$ in the ballistic phase leads to an implicit equation for $\langle w^2 \rangle$ (see §3.2.4).

Bec et al. (2010) also showed that, after a friction timescale, the dispersion of inertial-range particles make a transition to a tracer-like phase, where the separation variance increases as time cubed, a behavior known as the Richardson law. The Richardson law was first discovered for tracer pair dispersion at inertial-range scales. The transition to the Richardson phase at a friction timescale or so suggests the ballistic separation for a duration of τ_p already brings the average particle distance into the inertial range of the flow. The Richardson behavior was observed in the tracer pair dispersion both forward and

backward in time (Berg et al. 2006; see Appendix A). It is thus likely to exist also in the backward separation of inertial particles. We connect the Richardson phase to the ballistic phase at $\tau \simeq -\tau_p$, and use the Richardson law

$$d^2(\tau) \simeq g\bar{\epsilon}|\tau|^3 \quad (29)$$

at $\tau \lesssim -\tau_p$, where g is called the Richardson constant and $\bar{\epsilon}$ is the average dissipation rate of the flow. As the backward separation is typically faster than the forward case, the transition to the Richardson phase might occur slightly earlier than assumed here. Bec et al. (2010) did not report the value of g in the Richardson phase of inertial particle pair dispersion. As in PP10, we will take g as a parameter. In our model, we use a combined separation behavior that connects a ballistic and a Richardson phase at $\tau \simeq -\tau_p$.

The Richardson behavior would end when the separation becomes larger than the integral length scale, L , of the turbulent flow. At such a large distance, the flow velocities “seen” by the two particles is uncorrelated, and the particle separation is expected to be diffusive like in a random walk. It is thus appropriate to switch the Richardson behavior to a diffusive phase with $d^2(\tau) \propto |\tau|$ at $d \gtrsim L$. However, we find that the exact separation behavior at $d \gg L$ (or $R \gg L$) does not affect the prediction of our model. This is because at these scales both the structure functions, S_{\parallel} and S_{\perp} , and the timescale, $T(d)$ (or $T(R)$), become independent of d (or R). Therefore, eq. (19) (or eq. (20)) is insensitive to the behavior of the separation once it becomes much larger than L . This is confirmed by the numerical solutions of eqs. (19) and (20). For convenience, we keep using the Richardson’s law even after d exceeds L .

The separation behavior discussed above is based on the simulation results of Bec et al. (2010) for particles in the inertial range. For simplicity, we will use the same behavior for all particles, although its validity is questionable for small ($\tau_p \lesssim \tau_\eta$) and large ($\tau_p \gtrsim T_L$) particles. For small particles with $St \lesssim 3$, a ballistic phase is not clearly observed in the d^2 vs. time plots in Fig. 5 of Bec et al. (2010). We expect that a short ballistic phase is likely to exist if one plots $(d^2 - r^2)$ (instead of d^2) vs. time (see Fig. 20 in Appendix A for the $(d^2 - r^2)$ vs. time plot for tracer particle pairs). However, for $St \lesssim 3$ particles, the connection of the short ballistic phase to the Richardson behavior is more complicated than in the case of larger particles (Fig. 5 of Bec et al. 2010). This is because the pair separation of these particles does not enter the inertial range of the flow in a friction timescale or so. Therefore, an intermediate phase exists in between the ballistic and Richardson phases. Ideally, a three-phase behavior should be considered. Unfortunately, the separation behavior in the intermediate phase is completely unknown, and thus, to include it, one must adopt a pure parameterization. Here we take a simpler approximation: We still connect the Richardson behavior directly to the ballistic phase for $St \lesssim 3$ particles, although it cannot be justified physically. Essentially, this parameterizes the later two phases by a single Richardson law with a free parameter g . Future numerical studies for the entire separation behavior of small particles is needed to improve the approximation. For the particle distance range, $\eta/4 \lesssim r \lesssim \eta$, considered in our data analysis (see

§6.1), our model with the assumed behavior does give acceptable prediction for $St \lesssim 3$ particles. However, in the $r \rightarrow 0$ limit, a careful study of the intermediate separation phase of $St \lesssim 3$ particles is necessary to accurately model their relative velocity.

The problem of using the assumed behavior for particles with $\tau_p \gg T_L$ is that the Richardson phase does not exit. The velocities of these large particles are uncorrelated even at small distances (§3.1). Therefore, at timescales larger than τ_p , the separation is likely diffusive, i.e., $d(\tau) \propto |\tau|$. Realistically, one needs to connect the ballistic phase to a diffusive behavior rather than a Richardson law at $|\tau| \sim \tau_p$. However, it turns out that, at the end of the ballistic phase of these particles, the separation is already $\gtrsim L$. As discussed earlier, once the separation exceeds L , the exact separation behavior would not significantly affect the model prediction. This justifies using a combined separation behavior with a ballistic and a Richardson phase also for $\tau_p \gg T_L$ particles.

So far, the initial distance, r , just provides a floor value in our assumption for the particle separation d (eq. (28)). It is, however, possible that the value of r has additional effects on the separation behavior. Bec et al. (2010) only explored r above the Kolmogorov scale, and it is not clear whether the separation behavior has a qualitative difference if $r \lesssim \eta$. To model the particle collision speed, we are interested in the backward separation with $r \ll \eta$, and it would thus be helpful to systematically investigate whether and how the separation behavior changes as r decreases below η . We defer such a study to a later work. Due to the uncertainty in the separation behavior for $r \ll \eta$, we will focus on testing the model prediction for the relative velocity at significant fractions of the Kolmogorov scale ($\eta/4 \lesssim r \lesssim \eta$). We assume that the two-phase behavior discussed above applies for this range of r . Considering the existence of various uncertainties, the assumed separation behavior should be viewed more or less as a parameterization.

To constrain g in the Richardson phase, in Appendix A we measure g for the backward dispersion of tracer particle pairs in our simulated flow, which is used as a reference for inertial particles. The measured g for tracers in our flow at a limited resolution shows a dependence on r , suggesting that the Richardson constant for inertial particles may also depend on r . When comparing our model prediction to the simulation results at different r , we will adjust g to obtain best fits, and examine whether the best-fit values are consistent with the range of g measured from tracer particles. The Richardson constant for inertial particles may also have a dependence on τ_p (or St), which will be ignored for simplicity.

Finally, we point out that our model for the rms relative velocity does not directly account for the effect of the spatial clustering of the particles (see §7). Ideally, a theoretical model needs to consider the clustering and relative velocity statistics simultaneously. At a given time, the relative velocity determines the evolution of the spatial distribution of the particles, while the particle distribution may affect how the particles “see” the flow velocity and hence the evolution of the relative velocity statistics. However, modeling clustering and the relative velocity together self-consistently is very challenging, and is out of the scope of the current work.

3.2.4. Qualitative Behavior of Our Model Prediction

Our model for the particle structure tensor, S_{pij} , is now complete. Here we discuss the qualitative behavior of our model prediction. We start by considering the 3D variance, $\langle w^2 \rangle$. The contraction of eq. (19) gives,

$$\langle w^2 \rangle = \int_{-\infty}^0 \frac{d\tau}{\tau_p} \int_{-\infty}^0 \frac{d\tau'}{\tau_p} [S_{ll}(R) + 2S_{nn}(R)] \times \Phi_2(\tau' - \tau, R) \exp\left(\frac{\tau}{\tau_p}\right) \exp\left(\frac{\tau'}{\tau_p}\right), \quad (30)$$

which is an implicit equation of $\langle w^2 \rangle$ because R depends on $\langle w^2 \rangle$ in the ballistic separation phase. In §6.1, we will solve the equation numerically using an iterative method.

The qualitative behavior of the model prediction for $\langle w^2 \rangle$ can be obtained by analyzing the integrand in eq. (30). In the S-T limit ($\tau_p \rightarrow 0$), the exponential cutoff terms, $\frac{1}{\tau_p} \exp(\tau/\tau_p)$ and $\frac{1}{\tau_p} \exp(\tau'/\tau_p)$, in the integrand can be viewed as delta functions at $\tau = 0$ and $\tau' = 0$, respectively. This suggests that $\langle w^2 \rangle$ is approximately given by $\simeq (S_{ll} + 2S_{nn})$ at $R(0, 0)$. Since $R(0, 0) = r$, we have $\langle w^2 \rangle = \frac{\epsilon}{3\nu} r^2$ for r in the dissipation rate, which is consistent with the S-T prediction (see eq. (11)) for the 3D variance of the relative velocity.

The analysis of eq. (30) for larger particles is more complicated. We first note that $S_{ll}(R)$, $S_{nn}(R)$, and the timescale $T(R)$ in the correlation function Φ_2 are all increasing functions of R . Since R increases backward in time, the first factor in the integrand of eq. (30) increases with increasing $|\tau|$ and $|\tau'|$. A larger $T(R)$ also tends to increase the integral because, with increasing $T(R)$, Φ_2 allows contributions from a broader range of time lag ($\Delta\tau$). Together with the exponential cutoffs, these suggest that the contribution to the integral peaks at $\tau, \tau' \simeq -\tau_p$. We denote the particle separation at $\tau = \tau' = -\tau_p$ as R_p ($\equiv R(-\tau_p, -\tau_p)$), and refer to it as the primary distance.

In the extreme limit of large particles with $\tau_p \gg T_L$, R_p is expected to be much larger than the integral scale, L , of the flow. At $R_p \gg L$, we have $S_{ll} = S_{nn} = 2u'^2$, and $T(R_p) = T_L$. The exponential cutoff by Φ_2 indicates that only the time pairs (τ and τ') that satisfy the constraint $|\tau' - \tau| \simeq T_L$ give a significant contribution to the integral. Since $T_L \ll \tau_p$, Φ_2 reduces the range of τ and τ' that contributes to the double integral by a factor of T_L/τ_p . Assuming the main contribution to the integral is from $R \simeq R_p$ and accounting for the effect of Φ_2 , we find $\langle w^2 \rangle \simeq 6u'^2 T_L/\tau_p$. This is consistent with eq. (12), meaning that our model correctly reproduces the large particle limit.

For inertial-range particles with $\tau_\eta \lesssim \tau_p \lesssim T_L$, the primary distance, R_p , corresponds to inertial-range scales of the turbulent flow³. Using the Kolmogorov scaling

³ Roughly speaking, the role of the primary distance, R_p , is in analogy with the critical wavenumber, k^* , defined in the model of Volk et al. (1980). In the language of Volk et al., the velocity structures at scales much larger than R_p would be counted as Class I eddies, while structures below R_p would belong to Class III. However, Pan and Padoan (2010) pointed out a physical weakness in the evaluation of k^* in the Volk et al. model for the two-particle relative velocity, as the role of the separation of the two particles is not properly accounted for. The reader is referred to Section 4.1

gives $S_{\parallel}, S_{\text{nn}} \propto R_p^{2/3}$ and $T(R_p) \propto R_p^{2/3}$. From its definition, R_p is roughly the particle distance at the time when the ballistic phase connects to the Richardson phase (see §3.2.3). We thus assume that R_p is determined by a ballistic separation of duration τ_p , i.e., $R_p \simeq \langle w^2 \rangle^{1/2} \tau_p$. The effect of Φ_2 depends on how $T(R_p)$ compares to τ_p . If $T(R_p) > \tau_p$, $\Phi_2 \simeq 1$ for all time pairs in the range $-\tau_p \lesssim \tau, \tau' \lesssim 0$. On the other hand, if $T(R_p) < \tau_p$, Φ_2 provides a factor of $T(R_p)/\tau_p$, which follows from the same argument used above for the large particle limit. We find that both cases lead to the same scaling of $\langle w^2 \rangle$ with τ_p . In the first case, eq. (30) is approximated by $\langle w^2 \rangle \simeq [S_{\parallel}(R_p) + S_{\text{nn}}(R_p)] \propto R_p^{2/3}$. With $R_p \simeq \langle w^2 \rangle^{1/2} \tau_p$, we obtain $\langle w^2 \rangle^{1/2} \propto \tau_p^{1/2}$. In the second case with $T(R_p) < \tau_p$, we include a factor of $T(R_p)/\tau_p$ and estimate $\langle w^2 \rangle$ as $\simeq [S_{\parallel}(R_p) + S_{\text{nn}}(R_p)]T(R_p)/\tau_p \propto R_p^{4/3}/\tau_p$. It is straightforward to see that setting $R_p \simeq \langle w^2 \rangle^{1/2} \tau_p$ in this estimate gives the same scaling, $\langle w^2 \rangle^{1/2} \propto \tau_p^{1/2}$, as the first case. Therefore, whether $T(R_p)$ is larger or smaller than τ_p , our model predicts a $\tau_p^{1/2}$ (or $St^{1/2}$) scaling for inertial-range particles.

Using a similar argument, PP10 found that if the primary distance is determined by the Richardson's law, $R_p \simeq (g\bar{\epsilon}\tau_p^3)^{1/2}$, the model also predicts a $St^{1/2}$ scaling for inertial-range particles. Since both the ballistic and Richardson behaviors yield a $St^{1/2}$ scaling, a combination of a ballistic and a Richardson phase produces the same scaling (PP10). The $St^{1/2}$ scaling has been previously predicted by models of Volk et al. (1980), Cuzzi and Hogan (2003), Ormel and Cuzzi (2007), and Zaichik & Alipchenkov (2003). As mentioned earlier, the scaling may also be obtained from a dimensional analysis under a scale-invariant assumption. If the dimensional analysis exactly holds, then the departure from the $St^{1/2}$ scaling for inertial-range particles in a simulation of limited resolution is caused completely by the effects from dissipation or driving scales. The derivation of the $St^{1/2}$ scaling in all the models assumes a sufficiently broad inertial range. The scaling would not exist if the Reynolds number of the turbulent flow is low. In fact, the predicted $St^{1/2}$ behavior has never been confirmed by simulations due to the low numerical resolution. PP10 showed that, to see the $St^{1/2}$ scaling, the Taylor Reynolds number of the turbulent flow must be larger than $\simeq 300$. This is higher than in the 512^3 simulation used in the present study, and thus a clear $St^{1/2}$ scaling is not observed. It appears likely that the existence of this scaling can be verified at a twice larger resolution. We will conduct a 1024^3 simulation in a future work.

The above analysis for the scaling behavior of $\langle w^2 \rangle$ in different St ranges can be similarly applied to the simplified model, eqs. (20) and (21). The prediction of the simplified model is qualitatively the same as the original PP10 model.

Finally, we examine the model prediction for the radial and tangential components of the relative velocity. The prediction for $\langle w_r^2 \rangle$ and $\langle w_t^2 \rangle$ depends on the angular av-

erage of S_{Tij} in eq. (19) (or eq. 20). In §3.3.2, we made two assumptions, eqs. (26) and (27), for the angular average. Inserting the first assumption, eq. (26), into eq. (19) and comparing it with eq. (10), we find,

$$\begin{aligned} \langle w_r^2 \rangle &= \int_{-\infty}^0 \frac{d\tau}{\tau_p} \int_{-\infty}^0 \frac{d\tau'}{\tau_p} \left[\left(\frac{1}{3} + \frac{2r^2}{3R^2} \right) S_{\parallel}(R) + \right. \\ &\quad \left. \left(\frac{2}{3} - \frac{2r^2}{3R^2} \right) S_{\text{nn}}(R) \right] \Phi_2(\tau' - \tau, R) \exp\left(\frac{\tau + \tau'}{\tau_p}\right), \\ \langle w_t^2 \rangle &= \int_{-\infty}^0 \frac{d\tau}{\tau_p} \int_{-\infty}^0 \frac{d\tau'}{\tau_p} \left[\left(\frac{1}{3} - \frac{r^2}{3R^2} \right) S_{\parallel}(R) + \right. \\ &\quad \left. \left(\frac{2}{3} + \frac{r^2}{3R^2} \right) S_{\text{nn}}(R) \right] \Phi_2(\tau' - \tau, R) \exp\left(\frac{\tau + \tau'}{\tau_p}\right). \end{aligned} \quad (31)$$

In order to integrate these two equations, one needs to first solve eq. (30) for $\langle w^2 \rangle$ due to the dependence of R on $\langle w^2 \rangle$ in the ballistic phase. It is easy to show that, in the limit $\tau_p \rightarrow 0$, $R \rightarrow r$, and eq. (31) reduces to $\langle w_r^2 \rangle = S_{\parallel}(r)$ and $\langle w_t^2 \rangle = S_{\text{nn}}(r)$, reproducing the S-T formula, eq. (11). For larger particles with $\tau_p \gg \tau_\eta$, we have $R_p \gg r$, and thus eq. (31) predicts $\langle w_r^2 \rangle = \langle w_t^2 \rangle = \frac{1}{3}\langle w^2 \rangle$. Therefore, like $\langle w^2 \rangle$, both $\langle w_r^2 \rangle$ and $\langle w_t^2 \rangle$ scale as $St^{1/2}$ for inertial-range particles and as $St^{-1/2}$ in the large particle limit.

As discussed in §3.3.2, the second assumption, eq. (27), for the angular average of S_{Tij} predicts that $\langle w_r^2 \rangle = \langle w_t^2 \rangle = \frac{1}{3}\langle w^2 \rangle$ for all particles. In the S-T limit, eq. (30) gives $\langle w^2 \rangle = \frac{\bar{\epsilon}}{3\nu}r^2$, and thus $\langle w_r^2 \rangle = \langle w_t^2 \rangle = \frac{\bar{\epsilon}}{9\nu}r^2$. This means that the prediction by the second assumption for the radial and tangential relative speeds of $St \ll 1$ particles differs from the S-T formula, although it reproduces the S-T prediction for the 3D rms. We will test the model predictions for the relative velocity variances measured from our simulation data.

4. STATISTICS OF THE SIMULATED FLOW

In this section, we describe the numerical method used in our simulation and discuss the statistical properties of the simulated flow. Our simulation was conducted in a periodic 512^3 box with a length of 2π on each side. Using the Pencil code⁴ (Brandenburg & Dobler 2002, Johansen, Andersen, & Brandenburg 2004), we evolved the hydrodynamic equations,

$$\begin{aligned} \frac{\partial \rho}{\partial t} + \frac{\partial}{\partial x_i} (\rho u_i) &= 0, \\ \frac{\partial u_i}{\partial t} + u_j \frac{\partial u_i}{\partial x_j} &= \frac{1}{\rho} \frac{\partial}{\partial x_j} \left[\rho \nu \left(\frac{\partial u_i}{\partial x_j} + \frac{\partial u_j}{\partial x_i} - \frac{2}{3} \delta_{ij} \frac{\partial u_k}{\partial x_k} \right) \right] \\ &\quad - \frac{1}{\rho} \frac{\partial p}{\partial x_i} + f_i, \end{aligned} \quad (32)$$

with an isothermal equation of state, $p = \rho C_s^2$. The sound speed is set to unity, i.e., $C_s = 1$. The kinematic viscosity, ν , is taken to be constant, $\nu = 5 \times 10^{-5}$. A large-scale force, f_i , generated in Fourier space using 20 modes in the wavenumber range of $1 \leq k \leq 2$ is applied

of Pan and Padoan (2010) for a detailed discussion on this issue.

⁴ <http://pencil-code.nordita.org>

to drive and maintain the turbulent flow. The driving length scale, L_f , is thus about 1/2 box size. The balance between the energy input by the driving force and the dissipation by viscosity leads to a statistical steady state with a 1D rms velocity, u' , of 0.05, or a 3D rms of 0.085. This weakly compressible flow is suitable for the application to turbulence in protoplanetary disks. At an rms Mach number of 0.085, the flow statistics is essentially the same as incompressible turbulence (Padoan et al. 2004, Pan & Scannapieco 2011).

The integral length scale, L , in our simulated flow is found to be $\simeq 1$, i.e., about 1/6 box size. It is about 3 times smaller than the driving scale, L_f . The integral scale, L , represents the (longitudinal) correlation length of the velocity field, and we computed it from the energy spectrum, $E(k)$, of the flow, using the relation $L = \frac{\pi}{2u'^2} \int k^{-1} E(k) dk$ (Monin & Yaglom 1975). The energy spectrum, $E(k)$, is plot in the inset of Fig. (3). With $L = 1$, the large-eddy turnover time is $T_{\text{eddy}} = L/u' = 20$ in units in which the sound crossing time is 2π .

The average energy dissipation rate per unit volume by the viscosity term is given by $\bar{\epsilon} = \frac{1}{2\bar{\rho}} \langle \rho \nu (\partial_i u_j + \partial_j u_i - \frac{2}{3} \delta_{ij} \partial_k u_k)^2 \rangle$, where $\bar{\rho}$ is the average density. In our weakly compressible flow, the density fluctuations and the velocity divergence can be neglected, and the dissipation rate can be estimated by $\bar{\epsilon} = \nu \langle \omega^2 \rangle$, where $\langle \omega^2 \rangle$ is the vorticity variance. We find that $\langle \omega^2 \rangle = 0.92$, implying that $\bar{\epsilon} \simeq 4.6 \times 10^{-5}$. We also evaluated the dissipation rate from the 3rd-order longitudinal structure function using Kolmogorov's 4/5 law, $\langle \Delta u_r(\ell)^3 \rangle = -\frac{4}{5} \bar{\epsilon} \ell$, for ℓ in the inertial range. This latter method gives a larger dissipation rate, $\bar{\epsilon} = 5 \times 10^{-5}$, suggesting that a small fraction, $\simeq 8\%$, of kinetic energy is dissipated by numerical diffusion. The effective viscosity is thus larger than the adopted value by the same amount. We take the effective viscosity to be 5.4×10^{-5} and use it in our estimates of the Kolmogorov scales. We compute the Kolmogorov timescale from the vorticity variance as $\tau_\eta = \langle \omega^2 \rangle^{-1/2} = 1.04$. The Kolmogorov length scale is estimated to be $\eta = (\nu^3 / \bar{\epsilon})^{1/4} = 0.0075$, which corresponds to $\simeq 0.6$ cell size of the computation grid. The Kolmogorov velocity scale is $u_\eta = (\nu \bar{\epsilon})^{1/4} = 0.0072$ in units of the sound speed.

The Reynolds number of our simulated flow is $Re \equiv u' L / \nu \simeq 1000$. A more commonly-used Reynolds number in turbulence studies is the Taylor Reynolds number, $Re_\lambda \equiv u' \lambda / \nu$, where the Taylor micro length scale is defined as $\lambda \equiv (15 u'^2 / \langle \omega^2 \rangle)^{1/2}$. We find that $\lambda = 0.2$ in our simulated flow, and thus $Re_\lambda \simeq 200$. From the definitions of u_η and Re_λ , we have $u' / u_\eta = (Re_\lambda / \sqrt{15})^{1/2}$.

4.1. The Lagrangian Correlation Function and the Timescales

To study the Lagrangian statistics, we integrated the trajectories of 33.6 million tracer particles with zero inertia in the simulated flow. The total number of tracer particles corresponds to an average number density of 1 particle per 4 computational cells. To obtain the particle velocity inside a cell, we selected the triangular-shaped-cloud interpolation method already implemented in the Pencil code (Johansen and Youdin 2007). We output the particle positions to a data file in each

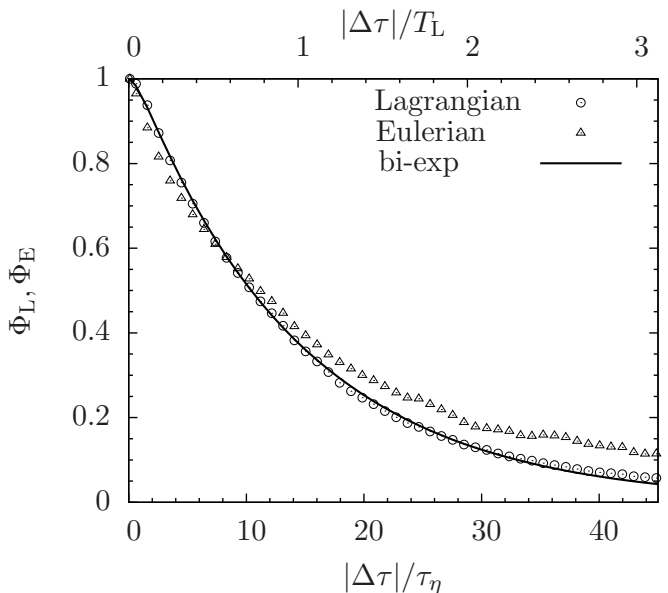


FIG. 2.— Lagrangian (Φ_L ; circles) and Eulerian (Φ_E ; triangles) temporal correlation functions in our simulated flow. The time lag, $\Delta\tau$, is normalized to the Kolmogorov timescale, τ_η and the Lagrangian correlation time, T_L , on the bottom and top X-axes, respectively. The solid line shows the best fit for Φ_L using the bi-exponential function, eq. (5).

$0.1\tau_\eta$. The Lagrangian correlation function, $\Phi_L(\Delta\tau)$, is computed as the average of the velocity correlation, $\langle u_i(\mathbf{X}(t), t) u_i(\mathbf{X}(t + \Delta\tau), t + \Delta\tau) \rangle / 3u'^2$, along the trajectories, $\mathbf{X}(t)$, of all particles. We considered both positive and negative $\Delta\tau$, corresponding to Lagrangian trajectories forward and backward in time, respectively. Our data confirmed that Φ_L is an even function of $\Delta\tau$, as expected from statistical stationarity (see §2). We find that the Lagrangian correlation timescale, $T_L (\equiv \int \Phi_L(\Delta\tau) d\Delta\tau)$, is $\simeq 15$, which is about 0.75 eddy turnover time, T_{eddy} . This is consistent with the simulation result of Yeung et al. (2006). Since $\tau_\eta = 1.04$ in our flow, we have $T_L = 14.4\tau_\eta$.

The Lagrangian correlation, Φ_L , in our flow is plot as circles in Fig. 2, where the time lag, $|\Delta\tau|$, is normalized to the Kolmogorov timescale, τ_η and the Lagrangian correlation time, T_L , on the bottom and top X-axes, respectively. The solid line shows the bi-exponential function, eq. (5), given in §2. The parameter z is set to 0.3, which suggests that the Taylor micro timescale, τ_T , is $\simeq 4.3\tau_\eta$. This value of τ_T corresponds to an acceleration variance, $a^2 \simeq 5.2(u_\eta / \tau_\eta)^2$. The bi-exponential function matches very well the simulation data. On the other hand, we find that a single exponential function could not give a satisfactory fit to Φ_L .

We also considered the Eulerian temporal correlation function, $\Phi_E(\Delta\tau)$. It is computed as the average, $\langle u_i(\mathbf{x}, t) u_i(\mathbf{x}, t + \Delta\tau) \rangle / 3u'^2$, over all grid points \mathbf{x} . The result is plot as triangles in Fig. 2. Φ_E is smaller than the Lagrangian correlation Φ_L at small time lags, and then becomes larger at $|\Delta\tau| \gtrsim 8\tau_\eta \simeq 0.55T_L$. Due to the slower decrease of Φ_E at large time lags, the Eulerian correlation time, $T_E \equiv \int \Phi_E(\Delta\tau) d\Delta\tau$, is slightly (10%) larger than T_L . We find that $T_E = 15.9\tau_\eta$. The Eulerian correlation function is of interest for large inertial particles with $\tau_p \gg T_L$. Due to their large inertia, these particles have small velocities and thus may stay around

as the flow sweeps by. Therefore, unlike small particles, the temporal series of the flow velocity “seen” by the large particles may be better described by the Eulerian velocity. This suggests that, for $\tau_p \gtrsim T_L$, it may be appropriate to replace the Lagrangian correlation used in our model by the Eulerian correlation. However, the Eulerian correlation function and timescale are quite close to the Lagrangian ones, and using the Lagrangian correlation for all particles in our model gives satisfactory predictions for both the 1-particle velocity and the 2-particle relative velocity at any St (§5 and §6.1).

We summarize the relevant timescales in the simulated flow and list them in an increasing order. The smallest timescale is Kolmogorov time τ_η , and we use it as a reference timescale. The Taylor micro scale, τ_T , was found to be $4.3\tau_\eta$ from the bi-exponential fit to the Lagrangian correlation function. The next timescale is the Lagrangian correlation time, T_L , which is $14.4\tau_\eta$. The Eulerian correlation time is slightly larger, $T_E \simeq 15.9\tau_\eta$. The large eddy turnover time, T_{eddy} , was measured to be $\simeq 19.2\tau_\eta$. Another commonly-used timescale is the dynamical time, τ_{dyn} , defined as the forcing length scale, L_f , divided by the 3D rms velocity ($\sqrt{3}u'$). We find that $\tau_{\text{dyn}} = 35\tau_\eta$.

In this work, we will express the particle friction time primarily by St and Ω . They correspond to normalizations to τ_η and T_L , which are convenient for small and large particles, respectively. One may also normalize τ_p to the large eddy turnover time, and define $\Omega_{\text{eddy}} = \tau_p/T_{\text{eddy}}$, which may be more convenient for practical applications. However, we prefer using Ω than Ω_{eddy} , because, according to our model, it is T_L that directly enters the physics of turbulence-induced particle velocity. Using the measured values of the timescales in our simulation, one may convert the normalizations by $\Omega_{\text{eddy}} = 0.75\Omega = 0.052St$.

4.2. The Flow Structure Functions and Energy Spectrum

In Fig. 3, we show the longitudinal (S_{11} ; open circles) and transverse (S_{nn} ; filled circles) structure functions in our simulated flow. The structure functions are measured from the velocity differences along the 3 directions, \mathbf{e}_1 , \mathbf{e}_2 and \mathbf{e}_3 , of the simulation grid. For $S_{11}(\ell)$, we computed and averaged the variances of $\Delta u_{11}(\ell) (\equiv u_1(\mathbf{x} + \ell\mathbf{e}_1) - u_1(\mathbf{x}))$, $\Delta u_{22}(\ell)$ and $\Delta u_{33}(\ell)$ over all the points, \mathbf{x} . Similarly, $S_{nn}(\ell)$ is obtained by averaging the variances of $\Delta u_{12}(\ell) (\equiv u_1(\mathbf{x} + \ell\mathbf{e}_2) - u_1(\mathbf{x}))$, $\Delta u_{13}(\ell)$, $\Delta u_{21}(\ell)$, $\Delta u_{23}(\ell)$, $\Delta u_{31}(\ell)$ and $\Delta u_{32}(\ell)$.

As discussed earlier, Kolmogorov’s similarity theory predicts that $S_{11}(\ell) \simeq C_K(\bar{\epsilon}\ell)^{2/3}$ for ℓ in the inertial range. We thus compensated the structure functions by $(\bar{\epsilon}\ell)^{2/3}$ in Fig. 3. A limited inertial range is seen in both S_{11} and S_{nn} . The Kolmogorov constant C_K is about 2. In the inertial range, the scaling exponent for S_{11} is found to be slightly larger than $2/3$, while the slope of S_{nn} is close to $2/3$. The ratio of the two structure functions in the inertial range is about 1.25, slightly smaller than the value, $4/3$, expected from the incompressibility condition (see §3). This is perhaps because our flow is weakly compressible. Another possibility is that the inertial range is too short to allow an accurate measurement of this ratio. Both structure functions become smooth, i.e., $\propto \ell^2$, as

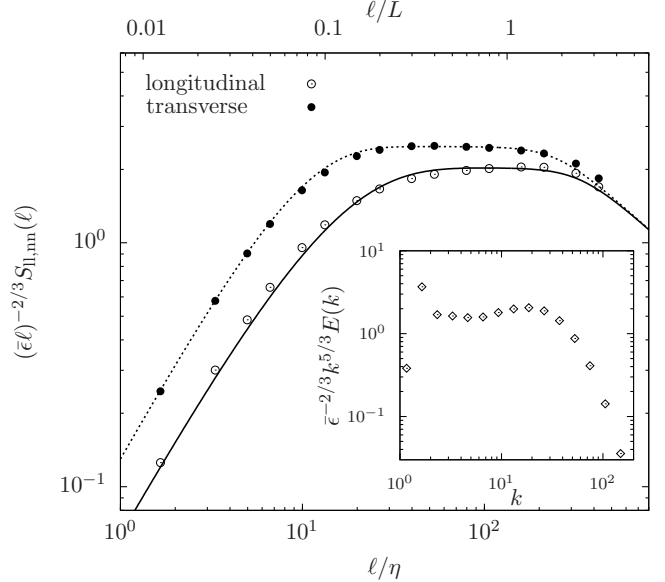


FIG. 3.— Longitudinal (open circles) and transverse (filled circles) structure functions in our simulated flow. The structure functions are compensated by the Kolmogorov scaling in the inertial range. The solid and dashed lines are fitting functions, eqs. (8) and (33), for S_{11} and S_{nn} , respectively. The bottom and top X-axes normalize ℓ to the Kolmogorov scale and the integral scale, respectively. The inset shows the energy spectrum of the flow, compensated by $\bar{\epsilon}^{2/3}k^{-5/3}$.

ℓ decreases toward the Kolmogorov scale, and approach $2u'^2$ in the limit $\ell \gg L$ (§3).

The solid line in Fig. 3 is the connecting formula, eq. (8), for S_{11} (§3). We set $C_K = 2$ in the formula. The line gives a fairly good fit to the data points. As discussed in §3, with the connecting formula for S_{11} , one may obtain a fitting function for S_{nn} using the incompressibility relation $S_{nn} = S_{11} + \frac{1}{2}ldS_{11}/d\ell$. However, the fitting function obtained this way overestimates S_{nn} in the inertial range, perhaps because the incompressibility condition does not exactly hold in our flow (see above). For a more accurate fit, we adopted a separate connecting formula for S_{nn} ,

$$S_{nn} = 2u'^2 \left[1 - \exp\left(-\frac{(\ell/\eta)^{4/3}}{(15C_{Kn}/2)}\right) \right] \times \left[\frac{(\ell/\eta)^4}{(\ell/\eta)^4 + (2u'^2/C_{Kn}u_\eta^2)^6} \right]^{1/6}, \quad (33)$$

where C_{Kn} is the scaling coefficient for S_{nn} in the inertial range. This connecting formula correctly reproduces the scaling behaviors of S_{nn} in different scale ranges. Its form is slightly different from eq. (8) for S_{11} . The dotted line in Fig. 3 corresponds to eq. (33) with $C_{Kn} \simeq 1.25C_K = 2.5$. We will use eqs. (8) and (33) in the computation of our model prediction for the particle relative velocity.

The inset of Fig. 3 shows the energy spectrum, $E(k)$, of our flow. The Kolmogorov theory predicts $E(k) = K\bar{\epsilon}^{2/3}k^{-5/3}$ in the inertial range, and we compensated the spectrum by $\bar{\epsilon}^{2/3}k^{-5/3}$. The power-law range ($3 \leq k \leq 10$) in the spectrum appears to be shorter than in the structure functions. The constant K is measured to be $\simeq 1.7$, consistent with previous studies (Ishihara et al. 2009). It is also consistent with the relation $K = 0.76C_K$ (Monin & Yaglom 1975), as the Kolmogorov constant, C_K , for S_{11} was found to be $\simeq 2$.

5. ONE-PARTICLE ROOT-MEAN-SQUARE VELOCITY

In our simulation, we included 14 species of inertial particles of different sizes. The friction timescale of the particles spans about four decades from $\simeq 0.1\tau_\eta$ to $\simeq 41T_{\text{eddy}}$ ($\simeq 54T_L$ or $\simeq 800\tau_\eta$), covering the entire scale range of the simulated flow. The friction timescale is equally spaced, increasing by a factor of two in each successive species. The number of particles contained in each species is 33.6 million, corresponding to an average particle density of one per 4 computational cells. The same number of tracer particles was included to study the Lagrangian statistics (§4.1). The integration of the particle trajectories is computationally very expensive. Using 4096 cores (512 Harpertown nodes) on the NASA/Ames Pleiades supercomputer, the simulation was run for 14 days, corresponding to a total CPU cost of 1.4 million hours.

To evolve the particle equation of motion (eq. 1), we adopted the triangular-shaped-cloud (TSC) method to interpolate the flow velocity inside the computational cells. The TSC interpolation is a well-established method (Hockney & Eastwood 1981, Johansen & Youdin 2007) that makes use of the nearest 27 grid points in a 3D simulation. In 1D, the weighting factor for the nearest 3 grid points is set to be quadratic with the distance to the points. The velocity difference in our simulated flow is linear with ℓ around and below the cell size, Δx , as seen from the ℓ^2 scaling of the structure functions toward Δx (bottom data points) in Fig. 3. This implies that the subgrid velocity field can be well approximated by a linear interpolation (Pan et al. 2011). The linear scaling is also captured by the TSC method. It is straightforward to show that, if the flow velocity is already linear around the resolution scale (approximately the case in our simulated flow), the scaling of the interpolated velocity at subgrid scales by the TSC method would be exactly linear, as the quadratic terms in the weighting functions cancel out in this special case. In comparison to the linear interpolation, the TSC method is of higher order and has the advantage of smoother connections at cell boundaries.

Initially, the 33.6 million particles in each species are distributed randomly in the simulation box. Each component of the initial particle velocity is also random, independently drawn from a uniform distribution in the range $[-0.01, 0.01]$. Therefore, the initial (1D) rms, $v'(0)$, of each velocity component of all the particles is $0.01/\sqrt{3}$, equivalent to a 3D rms of 0.01. The numerical values given here are in units of the gas sound speed, which was set to unity in the simulation. The initial particle conditions for all the 14 species are the same. We evolved the turbulent flow and the particle trajectories together right from the beginning of the simulation. At time zero, the gas velocity and density are set to zero and unity, respectively.

Our simulation run lasted for about $26T_{\text{eddy}}$ (or $35T_L$), and we saved 52 snapshots with an equal separation of $0.5T_{\text{eddy}}$. The black dotted line in Fig. 4 is the 3D rms of the flow velocity ($\sqrt{3}u'$) as a function of time, which shows that the flow is fully developed and reaches a (quasi) steady state at $t_{\text{dev}} \simeq 5 - 10T_{\text{eddy}}$. From top to bottom, the colored lines in Fig. 4 plot the 3D rms velocities of inertial particles with

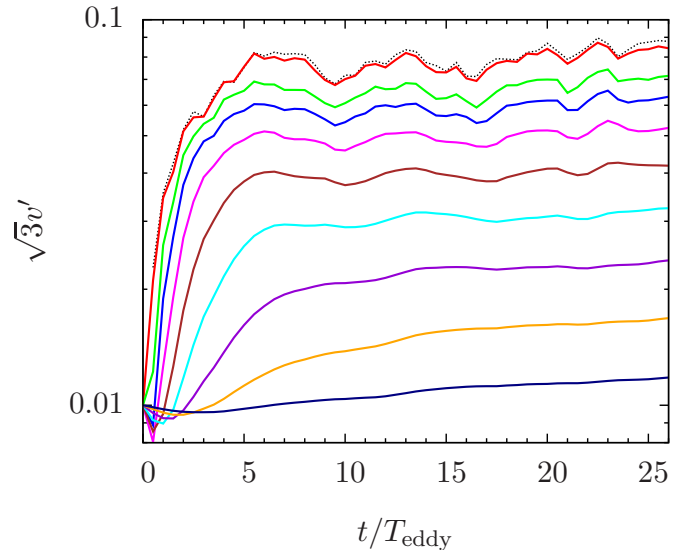


FIG. 4.— The temporal evolution of the 3D rms velocity, $\sqrt{3}v'$, of inertial particles of different sizes. The thin dotted line shows the 3D rms flow velocity, which reaches a (quasi) steady state at $t \gtrsim 5 - 10T_{\text{eddy}}$. The flow rms velocity is 0 at time zero, and the dotted line starts from $0.5T_{\text{eddy}}$ when the first snapshot is saved. From top to bottom, the color lines correspond to the rms velocity for particles with $St = 0.39, 6.12, 12.4, 24.9, 49.7, 99.4, 199, 398$ and 795 , respectively. The velocity is in units of the sound speed of the flow, which is set to unity in the simulation.

$St(\Omega)[\Omega_{\text{eddy}}] = 0.39(0.027)[0.02], 6.21(0.41)[0.32], 12.4(0.84)[0.65], 24.9(1.7)[1.3], 49.7(3.4)[2.6], 99.4(6.8)[5.2], 199(13.5)[10.4], 398(27)[20.7],$ and $795(54)[41.4]$, respectively. The numbers in the parentheses and square brackets correspond to Ω and Ω_{eddy} , respectively. We find there are dips at earlier times in the curves for relatively large particles. When our first snapshot was saved at $0.5T_{\text{eddy}}$, particles with $\tau_p \gtrsim 0.5T_{\text{eddy}}$ partially lost the memory of the initial rms velocity, and meanwhile their velocity had some contribution from the flow velocity, u' , between $t = 0$ and $0.5T_{\text{eddy}}$. However, since u' was 0 at $t = 0$, this contribution turns out to be small and does not compensate the decrease due to the memory loss of the initial velocity. This causes a decrease in v' and leads to dips at $t \gtrsim 0.5T_{\text{eddy}}$. Due to their short memory time, the small particles forgot their initial velocity, $v'(0)$, at the first snapshot, and their velocity was close to the flow velocity at $0.5T_{\text{eddy}}$, which is already slightly larger than $v'(0)$. Therefore, no dips appear for the small particles with $\tau_p \lesssim 0.5T_{\text{eddy}}$. The top six color lines appear to reach a steady state at $\simeq 10T_{\text{eddy}}$. For the bottom three lines, $v'(t)$ keeps increasing gradually but almost monotonically. This may imply that these largest particles need more time to relax. It is also possible that the slow increase of v' at late times is simply caused by the slight rise of the flow velocity (see the black dotted line).

The relaxation timescale for inertial particles in a stationary turbulent flow is essentially the time for the particles to forget the initial condition, and is roughly given by the friction timescale, if the initial velocity is not much larger than the final steady-state value (as is the case for our initial conditions). The estimate for the relaxation time in our simulation is a little complicated because the

particles are released to the flow before t_{dev} . For particles with $\tau_p \ll t_{\text{dev}}$, the dynamical relaxation is expected once the flow is fully developed, i.e., at $\simeq t_{\text{dev}}$. This is the case for the top 5-6 color lines in Fig. 4.

For the bottom 3-4 lines, $\tau_p \gtrsim t_{\text{dev}}$, and we expect these particles would be relaxed at some time in the range $(\tau_p, t_{\text{dev}} + \tau_p)$. The lower limit is the minimum relaxation time, and the upper limit is based on the consideration that, if the particle evolution started at t_{dev} instead of time 0, the particles would relax at $\simeq t_{\text{dev}} + \tau_p$. From this estimate, the third largest particles ($St = 199$) are relaxed by $\lesssim 20T_{\text{eddy}}$, and the second largest ones ($St = 398$) are likely relaxed by the end of the simulation. On the other hand, the largest ($St = 795$) particles may not have reached a relaxed state. However, the quite flat $v'(t)$ of the $St = 795$ particles indicates the possibility they are actually relaxed toward the end of the simulation. If that is the case, a likely reason for it is that the chosen initial condition (e.g., the rms velocity) happens to be very similar to the expected relaxed state of these particles. This similarity may reduce the relaxation time. We assume that all particles in our simulation are relaxed in the last 5-6 T_{eddy} .

In our data analysis, we average over three snapshots at $t = 21.5, 24$ and $26T_{\text{eddy}}$. For the uniformity of the data sample, we use the same snapshots for all particle species. Since the largest particles become relaxed around the end of the simulation, we only select late snapshots at $t \gtrsim 20T_{\text{eddy}}$. The purpose of averaging over a number of snapshots is to obtain better statistics by increasing the sample size. It is thus helpful to use well-separated snapshots with independent statistics. A temporal separation of $\simeq 2T_{\text{eddy}}$ guarantees the particle velocities at the selected snapshots are independent for the first 10 particle species. The velocities of the largest four particles remain correlated for significantly longer than $\simeq 2T_{\text{eddy}}$. Therefore, unlike the case of smaller particles, using the selected snapshots may not effectively increase the independent sample size or the measurement accuracy. If the computation resources allow, it would be ideal to run the simulation much longer and collect snapshots separated by a few friction times of the largest particles.

In Fig. 5, we show the simulation result for the 1D rms, v' , of the particle velocity as a function of St . We normalized v' by the rms velocity, u' , of the flow. The top X-axis normalizes the friction time to the Lagrangian correlation time. One may convert St (or Ω) to Ω_{eddy} by $\Omega_{\text{eddy}} = 0.052St$ (or $\Omega_{\text{eddy}} = 0.75\Omega$). The dotted and solid lines are predictions, eq. (4) and eq. (6), of our model using single- and bi-exponential forms for the temporal correlation function, respectively. The model approximates the trajectory correlation function, Φ_1 , by the Lagrangian correlation function, Φ_L (see §2). For the bi-exponential case, we set the parameter $z = 0.3$, which best fits Φ_L measured from the Lagrangian trajectories (see §4.1). The two lines almost coincide, indicating that the model prediction for v' is insensitive to the exact form of the correlation function, and depends only on the correlation timescale⁵. In both curves, we set $T_L = 15.4\tau_\eta$,

⁵ Unlike the case of the 1-particle velocity, the choice of Φ_1 is crucial for predicting the relative velocity between different particles in the S-T limit (PP10). In the bidisperse case, adopting the bi-exponential form for Φ_L and Φ_1 is needed to reproduce the

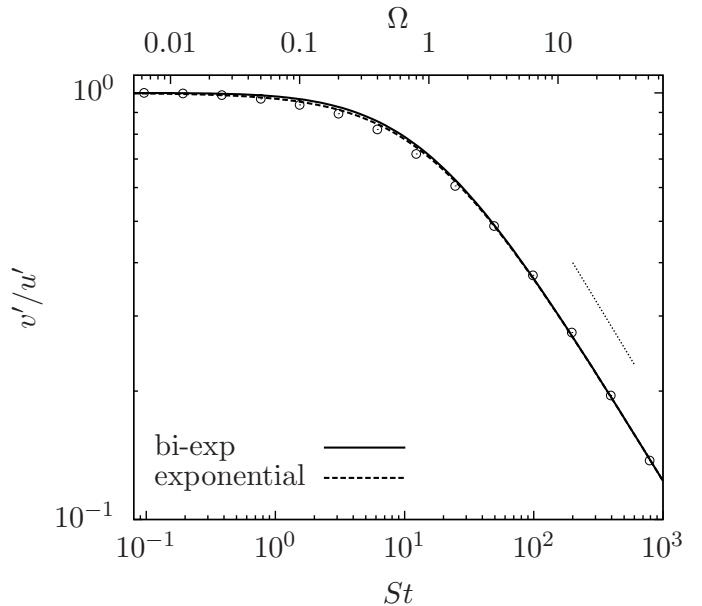


FIG. 5.— The 1-particle rms velocity, v' , as a function of the particle friction time. The bottom and top X-axes normalize τ_p to τ_η and T_L , respectively. The dotted and solid lines are the predictions, eq. (4) and eq. (6), of our model using single- and bi-exponential forms for the temporal correlation function, respectively. In both cases, T_L is set to $15.4\tau_\eta$, and the parameter z in the bi-exponential case is set to 0.3. The thin dotted line segment denotes a $St^{-1/2}$ scaling.

generally consistent with the directly measured value of $14.4\tau_\eta$ (see §4.1). As expected, v' follows the $St^{-1/2}$ scaling (the dotted line segment) at $\Omega \gg 1$. This supports our claim that the largest particles are dynamically relaxed at the end of the run.

The flow velocity “seen” by large particles with $\tau_p \gtrsim T_L$ may be closer to Eulerian than Lagrangian (§4.1), and thus using Φ_L for the trajectory correlation Φ_1 is not well justified (§2). However, the assumption is validated by our simulation result for all particles. This is because, first, based on our model prediction, v' is controlled mainly by the correlation time, not the form of the correlation function, and, second, the Eulerian correlation timescale, T_E , was found to be close to T_L . Thus, whether Φ_1 is approximated by Φ_E or Φ_L , the predicted 1-particle velocity would be similar, justifying the use of Φ_L for all particles. The best-fit correlation timescale, $15.4\tau_\eta$, used in Fig. 5 is in between the measured values of T_L ($14.4\tau_\eta$) and T_E ($15.9\tau_\eta$). This suggests that the temporal statistics of the flow velocity “seen” by a large particle is in between that along a Lagrangian trajectory and that at a fixed Eulerian point. It is interesting to note that, although a single-exponential function does not well fit either Φ_E or Φ_L (§4.1), our model prediction for the rms particle velocity with an exponential correlation is in good agreement with the simulation data.

We also computed the probability distribution of the 1-particle velocity. The velocity of small particles is expected to be Gaussian because it simply samples the 1-point PDF of the flow velocity, which is close to Gaussian. For large particles with $\tau_p \gg T_L$, the velocity would also

acceleration contribution to the relative velocity, while a single exponential form cannot correctly capture the effect of the flow acceleration on Φ_L at small time lags.

be Gaussian because their equation of motion is essentially a Langevin equation. We find the 1-particle velocity PDF is indeed nearly Gaussian at all St . The nearly Gaussian PDF for the largest particles in the three selected snapshots also supports our assumption that these particles are relaxed at $t \gtrsim 20T_{\text{eddy}}$.

6. THE RELATIVE VELOCITY OF INERTIAL PARTICLES

Now we explore the statistics of 2-particle relative velocity in our simulation, focusing on the monodisperse case of equal-size particles. Using the simulations data, we can compute the joint probability distribution, $\rho(\mathbf{r}, \mathbf{w}; St)$, of the particle separation and the relative velocity as a function of St (see, e.g., Zaichik et al. 2003, Gustavsson and Mehlig 2011, Hubbard 2013). The joint distribution is defined such that the number of particles located in a volume dV at a separation \mathbf{r} from a reference particle and moving at a relative velocity in the range $[\mathbf{w}, \mathbf{w} + d\mathbf{w}]$ is given by $\bar{n}\rho(\mathbf{r}, \mathbf{w}; St)dVd\mathbf{w}$, where \bar{n} is the average number density. Once the particle statistics become isotropic, it is convenient to study the distributions, $\rho(r, w_r; St)$, $\rho(r, w_t; St)$, and $\rho(r, |\mathbf{w}|; St)$, for the radial, tangential components and the 3D amplitude of the relative velocity. The normalization of $\rho(r, w_r; St)$ with respect to w_r is given by $\int_{-\infty}^{\infty} \rho(r, w_r; St)dw_r = g(r, St)$, where $g(r, St)$ is the so-called radial distribution function (RDF). The same normalization applies for $\rho(r, w_t; St)$ and $\rho(r, |\mathbf{w}|; St)$. The RDF represents the overall probability of finding a neighbor with any relative speed, and is a measure of the spatial clustering of inertial particles (see §7). With the joint distributions and the RDF, we define the relative speed PDFs as $P(w_r, St) = \rho(r, w_r; St)/g(r, St)$, $P(w_t, St) = \rho(r, w_t; St)/g(r, St)$, and $P(|\mathbf{w}|, St) = \rho(r, |\mathbf{w}|; St)/g(r, St)$. For the simplicity of notation, the dependence of the PDFs on r is not explicitly indicated. A systematic study of these PDFs is given in §6.2. Our simulation results for the variances of the PDFs are presented in §6.1.

For each species (St), we measure the relative velocity of particle pairs mainly at three distances, $r = 1\eta$, 0.5η and 0.25η . These distances are below the resolution scale of the simulation. Measuring the statistics at subgrid scales is justified, as the subgrid flow velocity is reliably captured by the adopted TSC interpolation (§5). For each St and r , we search the simulation box for all particle pairs in a distance shell from $r - \delta r/2$ to $r + \delta r/2$. For $r = 1\eta$ and 0.5η , we set the shell thickness δr to $0.08r$. To increase the number of particle pairs hence the measurement accuracy at $r = 0.25\eta$, we used a larger thickness, $\delta r = 0.16r$, which is likely the largest value one can reasonably adopt. If δr is increased further by a factor of 2, it would be comparable to r , and one may not safely attribute the measured statistics to a single particle distance. For $r = 0.25\eta$ and $\delta r = 0.16r$, the number of particle pairs in one snapshot is typically on the order of $\simeq 10^4$. This number of pairs is about enough to provide sufficient statistics, although the measured relative speed PDF at $r = 0.25\eta$ already shows considerable noises at the tails (see Fig. 13 in §6.2.3). A study of smaller values of r is desirable. However, at smaller r , the number of particle pairs available becomes more limited and does not allow accurate statistical analysis. We take the statistical accuracy as priority, and restrict our

data analysis to $r \geq \eta/4$.

To check the relaxation of the 2-particle statistics, we examined the temporal evolution of the particle pair counts, or equivalently the RDF, and the rms relative velocity in our simulation. The RDFs for all the 14 particle species reach a quasi steady state at $\simeq 10T_{\text{eddy}}$, when the turbulent flow is fully developed (Fig. 4). This further confirms that the dynamics of the particles in the first 10 species is well relaxed at $10T_{\text{eddy}}$. However, the steady state of the RDF is not a perfect indicator for the relaxation of the largest few particles. These particles do not show significantly clustering (see §7.1), and their RDFs are close to unity at all times. The rms of the relative velocity also reaches a quasi steady state at $\gtrsim 10T_{\text{eddy}}$ for essentially all particles. As discussed in §5, there is an uncertainty in the relaxation of the largest particles ($St = 795$) because the expected relaxation time is larger than the end time of the simulation. Our data shows that the rms relative velocity of the largest particles is about equal to $\sqrt{2}$ times the 1-particle rms velocity, consistent with the expected relaxed state (see §3.1). The relaxation of the largest particles is also supported by our later results that the rms relative speed obeys the expected $St^{-1/2}$ scaling (§6.1) and the relative velocity PDF approaches Gaussian (§6.2). In summary, there is sufficient evidence that the 2-particle statistics is well relaxed toward the end of our simulation for all particles.

Again we use the three snapshots at $21.5T_{\text{eddy}}$, $24T_{\text{eddy}}$, and $26T_{\text{eddy}}$ in our analysis. For the first 10 species with $\tau_p \lesssim 2T_{\text{eddy}}$, the velocity of each particle is independent in the three snapshots. Averaging over these snapshots increases the measurement accuracy for both the 1-particle velocity and the 2-particle relative velocity. We find that using the three snapshots also improves the relative velocity measurement for the four largest particles (unlike the case of the 1-particle rms; see §5), even though the velocity of each individual particle is correlated for longer than $2-3T_{\text{eddy}}$. To effectively increase the independent sample size, one should avoid the same two particles to appear as a pair in two successive snapshots selected (see Hubbard 2013). It turns out that, for the typical relative velocity of the four largest particles, a particle pair at $\eta/4 \lesssim r \lesssim \eta$ separates to a significant distance and no longer makes a pair in $2-3T_{\text{eddy}}$. Since the velocities of any two large particles with $\tau_p \gg T_{\text{eddy}}$ at any distance in a snapshot are independent (§3.1), the relative velocities of new pairs that appear in $2-3T_{\text{eddy}}$ are typically independent of those in the earlier snapshot. Therefore, including the three snapshots does increase the independent sample size and the measurement accuracy for the relative velocity of the largest particles.

To decompose the relative velocity, \mathbf{w} , into radial and tangential components, we set up a local coordinate system (\mathbf{e}'_1 , \mathbf{e}'_2 and \mathbf{e}'_3) for each selected particle pair. The direction \mathbf{e}'_1 is chosen to coincide with the particle separation, \mathbf{r} . In terms of the unit base vectors, \mathbf{e}_1 , \mathbf{e}_2 and \mathbf{e}_3 , of the simulation grid, \mathbf{e}'_1 is expressed as $\cos\theta \cos\phi \mathbf{e}_1 + \cos\theta \sin\phi \mathbf{e}_2 + \sin\theta \mathbf{e}_3$, where $\sin\theta = r_3/r$, $\cos\theta = (r_1^2 + r_2^2)^{1/2}/r$, $\cos\phi = r_1/(r_1^2 + r_2^2)^{1/2}$, and $\sin\phi = r_2/(r_1^2 + r_2^2)^{1/2}$. The radial component is calculated as $w_r = \mathbf{w} \cdot \mathbf{e}'_1$. For the two tangential directions, we set $\mathbf{e}'_2 = -\sin\phi \mathbf{e}_1 + \cos\phi \mathbf{e}_2$ and $\mathbf{e}'_3 = -\sin\theta \cos\phi \mathbf{e}_1 - \sin\theta \sin\phi \mathbf{e}_2 + \cos\theta \mathbf{e}_3$, which are obtained

by two consecutive rotations of the original coordinates. The first rotation is about \mathbf{e}_3 by ϕ , which moves \mathbf{e}_2 to \mathbf{e}'_2 , and the second one is about \mathbf{e}'_2 by $-\theta$, which further brings the original base vectors \mathbf{e}_1 and \mathbf{e}_3 to \mathbf{e}'_1 and \mathbf{e}'_3 . We then calculate $w_{t2} = \mathbf{w} \cdot \mathbf{e}'_2$ and $w_{t3} = \mathbf{w} \cdot \mathbf{e}'_3$. The PDFs of w_{t2} and w_{t3} are found to be almost the same, as expected from the statistical isotropy⁶. We thus take the PDF of a tangential component, w_t , to be the average PDF of w_{t2} and w_{t3} . The variance of w_t is calculated as $\langle w_t^2 \rangle = \frac{1}{2} (\langle w_{t2}^2 \rangle + \langle w_{t3}^2 \rangle)$.

6.1. The Root-mean-square Relative Speed

We first study the root-mean-square of the relative velocity. We test the prediction of the PP10 model and validate the physical picture revealed by the model. Fig. 6 shows the simulation result for the 3D rms, $\langle w^2 \rangle^{1/2}$, of the relative velocity as a function of the particle inertia. The data points correspond to the measured relative velocity at a distance of 1η . On the bottom and top X-axes, we normalize the friction timescale to the Kolmogorov timescale ($St = \tau_p/\tau_\eta$) and the Lagrangian correlation timescale ($\Omega = \tau_p/T_L$), respectively. The left and right Y-axes normalize the relative speed to the Kolmogorov velocity and the 3D rms flow velocity, respectively. As a reminder, $u' = (Re_\lambda/\sqrt{15})^{1/2} u_\eta = 7u_\eta$ in our simulated flow. Similar normalizations are adopted in most figures in the rest of the paper. The normalization to Kolmogorov scales is a convention commonly adopted in the turbulence literature, which is convenient for the study of small particles with $St \lesssim 1$ and the related phenomena at small length scales. On the other hand, the normalization to large-scale quantities is more useful for large particles, and may be more convenient for practical applications since observations constrain the large-scales properties of protoplanetary turbulence⁷.

At small St , the 3D rms relative speed is roughly constant, and its value is consistent with the S-T prediction, $\langle w^2 \rangle^{1/2} = u_\eta/\sqrt{3}$. The relative speed starts to rise at $St \simeq 1$, as the effect of the particle memory and the backward separation becomes important. For the largest particles, we find that $\langle w^2 \rangle^{1/2} \simeq \sqrt{6}u'(T_L/\tau_p)^{1/2}$, with $T_L \simeq 14\tau_\eta$, in agreement with eq. (12) for the large particle limit, $\tau_p \gg T_L$. Like the earlier result for the 1-particle rms velocity, this provides a validation for using the Lagrangian correlation function for the trajectory correlation, Φ_1 , of large particles with $\tau_p \gg T_L$, even though their trajectories may significantly deviate from Lagrangian tracers. The predicted $St^{1/2}$ scaling for inertial-range particles by various models is not observed due to the limited inertial range of the simulated flow.

The solid curve in Fig. (6) is the prediction of the PP10 model, and it is obtained by numerically solving eq. (30). In the computation, we used eq. (8) for S_{11} , eq. (33) for S_{nn} , and eq. (23) for $T(\ell)$, respec-

⁶ When selecting the local coordinate system, one may also perform a third rotation about \mathbf{e}'_1 by an arbitrary angle. This changes \mathbf{e}'_2 and \mathbf{e}'_3 . However, from the statistical isotropy, w_{t2} and w_{t3} would be statistically invariant under this third rotation.

⁷ For inertial-range particles, one may choose to normalize the physical quantities to turbulent eddies that couple to the particle friction timescale. This normalization would be convenient to examine whether the relative velocity of inertial-range particles shows a scale-invariant behavior.

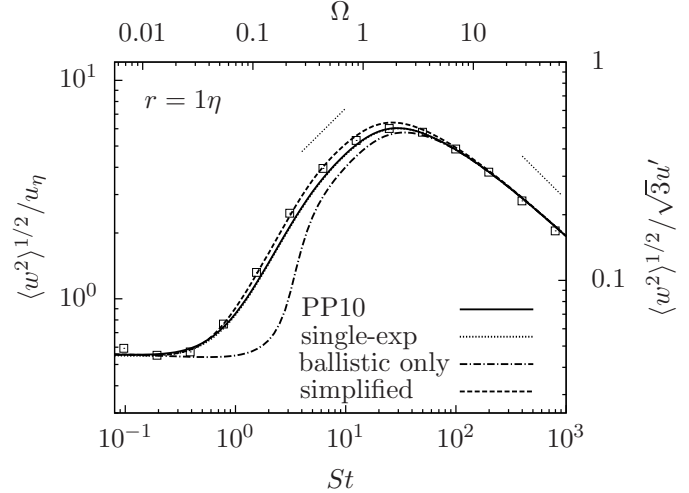


FIG. 6.— The 3D rms relative velocity, $\langle w^2 \rangle^{1/2}$, as a function of the Stokes number, St . The data points show the simulation result. The solid line is the prediction of the PP10 model (eq. 30) using a bi-exponential temporal correlation Φ_2 and a two-phase separation with $g = 1.6$ in the Richardson phase. The dotted line corresponds to the same model but with a single-exponential Φ_2 . The line is barely visible because it almost coincides with the solid line. The dot-dashed line assumes ballistic separation at all times. The dashed line is the prediction of the simplified model, eqs. (20) and (21), using single-exponential Φ_2 and a two-phase separation behavior with $g = 1.0$. The top X-axis and the right Y-axis normalize the friction timescale and the relative speed to T_L and $\sqrt{3}u'$, respectively. The left and right dotted line segments show $St^{1/2}$ and $St^{-1/2}$ scalings.

tively. The parameters in these equations were set to $C_K = 2$, $C_{Kn} = 2.5$, $C_T = 0.4$ and $T_L = 14.4\tau_\eta$. A bi-exponential form, eq. (24), is adopted for the temporal correlation Φ_2 . We used a two-phase behavior for the particle separation backward in time (§3.4.3), connecting the ballistic and Richardson phases at $\tau_c = -\tau_p$. We set $d^2(\tau) = r^2 + \langle w^2 \rangle \tau^2$ for $\tau \geq \tau_c$, and then switch to the Richardson's law, $d^2(\tau) = d^2(\tau_c) + g\bar{\epsilon}(|\tau|^3 - |\tau_c|^3)$, for $\tau < \tau_c$, where $d^2(\tau_c) = r^2 + \langle w^2 \rangle \tau_c^2$. To fit the simulation data, the Richardson constant, g , is set to 1.6. The solid line is in good agreement with the data points, confirming the validity of the physical picture of our model. Adopting a larger g could further improve the fitting quality at intermediate St .

In Appendix A, we investigate the backward separation of tracer particles in our simulated flow, and find that $0.5 \lesssim g \lesssim 1.2$. Therefore, the g value used in the solid line in Fig. 6 is significantly larger than that of tracer particles. There exist two possibilities. First, the backward separation of inertial particles in the Richardson phase is indeed faster than tracers. Second, the accuracy of our model for the trajectory structure tensor, S_{Tij} , may be inadequate. For example, approximating the correlation timescale, $T(\ell)$, in Φ_2 by the eddy turnover time at the scale of the particle separation, R , is essentially a qualitative assumption. Also there is an order-of-unity uncertainty in the adopted parameter C_T for the scaling of $T(\ell)$ in the inertia range (see eq. (23)). If a larger C_T were adopted, we could obtain a good fit to the data with a smaller g . Finally, in our model for S_{Tij} , we neglected the correlation between the particle distance, R , and the fluctuations in the flow velocity difference, $\Delta u(R)$, seen by the particle pair (see §3.2). This tends to underesti-

mate the relative velocity.

The dotted line in Fig. (6) is the prediction of the same PP10 model, but with a single-exponential Φ_2 (eq. (22)). The dotted line is actually not distinguishable from the solid line, confirming the earlier statement in §3.2.1 that our model prediction for the relative speed is insensitive to the function form of Φ_2 . This leaves us some freedom for the choice of Φ_2 , as long as the correlation timescale is accurately estimated. In particular, it provides a justification for approximating Φ_2 by the same function form, e.g., a bi-exponential function, for all particles, although realistically the form of Φ_2 may have a dependence on the particle inertia.

The dot-dashed curve plots the prediction of the PP10 model assuming that the particle separation is ballistic with $d^2(\tau) = r^2 + \langle w^2 \rangle \tau^2$ at all times. The model is otherwise the same as the solid line. A pure ballistic separation is not realistic, and we show it here just to illustrate whether the Richardson phase provides important contribution to the relative velocity. At $0.5 \lesssim St \lesssim 5$, the dot-dashed line significantly underestimates $\langle w^2 \rangle$, and, from $St \simeq 5$, it becomes close to both the data points and the solid line using a two-phase separation behavior. A possible explanation for this is that, for $0.5 \lesssim St \lesssim 5$, the relative velocity receives a significant contribution from the Richardson phase, even though this phase occurs at times beyond the particle memory timescale, i.e., at $\tau \lesssim -\tau_p$. In that case, accounting for this phase would be necessary for particles with intermediate St . However, the validity of the above interpretation is subject to future tests. There is the possibility that the discrepancy between the dot-dashed line and the data points may be caused by various uncertainties in our model for the trajectory structure tensor, S_{Tij} (see above).

The dashed line is the prediction of the simplified model, eqs. (20) and (25), using a single-exponential Φ_2 . As before, the simplified model with a bi-exponential Φ_2 gives almost the same prediction. The same two-phase separation as in the solid line for the original PP10 model is adopted. For the simplified model, the best-fit g is found to be $\simeq 1$, which is close to the g values measured from tracer particles. The simplified model also fits the data better for intermediate St , although the assumption made in the model is physically not better than the original PP10 model. The simplified model may be a preferred choice, as its prediction is easier to compute.

We find that the Stokes number, St_m , at which the rms relative velocity peaks is $\simeq 30$, corresponding to a friction timescale of $\simeq 2T_L$ (or $\simeq 1.5T_{\text{eddy}}$). The peak value of the 3D rms relative velocity is $\simeq 6.2u_\eta$, which is about half the 3D rms velocity ($\sqrt{3}u'$) of the flow. We give an explanation for the behavior of the peak relative velocity using the qualitative analysis of our model prediction discussed in §3.2.4. The analysis was based on the primary distance R_p , estimated as $R_p = \langle w^2 \rangle^{1/2} \tau_p$. R_p generally increases with τ_p . Around the relative velocity peak, $\tau_p \simeq 30\tau_\eta$ and $\langle w^2 \rangle^{1/2} \simeq 6.2u_\eta$, and thus $R_p \simeq 200\eta$. From eq. (23), the correlation time, $T(\ell)$, at $\ell \simeq 200\eta$ is about $14\tau_\eta$, which is close to T_L . For $St \gtrsim 30$, $T(R_p)$ would be constant and $\simeq T_L$. Consequently, the Φ_2 term in eq. (30) provides a factor of T_L/τ_p for all particles with $St \gtrsim 30$ (see §3.2.4). Using the same analysis as in §3.2.4, one can show that this

factor causes the relative speed to decrease with τ_p , even though the structure functions $S_{11}(R_p)$ and $S_{nn}(R_p)$ are still increasing with R_p at $R_p \simeq 200\eta$ (see Fig. 3). For particles with $St \lesssim 30$, both the structure functions and $T(R_p)$ decrease with decreasing R_p , and thus the relative speed would decrease with decreasing τ_p . Therefore a peak forms at $St_m \simeq 30$. We find that, for particles with $St \simeq 30$, the amplitude of the flow velocity difference at the primary distance ($R_p \simeq 200\eta$) is smaller than $\sqrt{3}u'$, and this is responsible for why the maximum relative velocity is significantly lower than the rms flow velocity. The discussion here shows that the relative velocity is the largest for the particles whose primary distance R_p corresponds to the size of turbulent eddies with lifetime $\simeq T_L$. Clearly, the backward particle separation plays an important role in determining the peak Stokes number, St_m .

The model of Volk et al. (1980) and its later developments predict that the relative speed reaches the maximum when τ_p is equal to a large eddy time, t_L (e.g., Markiewicz, Mizuno & Volk 1991, Cuzzi and Hogan 2003, Ormel & Cuzzi 2007). The definition of t_L in these studies is different from the timescales we used, and it is not clear whether, using parameters appropriate for our simulated flow, these models may correctly produce a peak at $St_m = 30$. Another issue is that, in the Volk et al. model, the peak relative speed is predicted to be equal or close to the rms velocity of the flow. This overestimates the relative speed around the peak by a factor of 2. A physical problem of the Volk et al. model has been discussed in the Introduction (see PP10 for details). The performance of the Volk et al. (1980) model may improve as the Reynolds number of the flow increases, which will be tested by future higher-resolution simulations.

6.1.1. Dependence on the Particle Distance

In Fig. 7, we plot the 3D rms relative velocity at different distances, r . The squares, circles and diamonds correspond to $r = 1, 0.5$ and 0.25η , respectively. In this distance range, the relative velocity shows a r -dependence at $St \lesssim 6$, while it is independent of r for $St \gtrsim 6$ particles. In the context of our physical picture, this is because the friction time, τ_p , of $St \gtrsim 6$ particles is long enough that the backward particle separation after a duration of $\simeq \tau_p$ is insensitive to the “initial” value, r . On the other hand, the relative speed of smaller particles relies on the flow velocity difference they saw in the near past, when the particle separation was still dependent on r .

The solid and dotted lines are predictions of the PP10 model with bi-exponential correlation function Φ_2 and the simplified version with single-exponential Φ_2 , respectively. The lines for $r = 1\eta$ have already been shown in Fig. (6), and the Richardson constant, g , was set to 1.6 and 1.0, respectively, in the two models. At smaller r , the best-fit value of g becomes smaller. For the PP10 model, we adopted $g = 1.3$ and 1.0 for $r = 0.5$ and 0.25η , respectively. The decrease of g with decreasing r is consistent with our result in Appendix A for the tracer particle pair dispersion. The backward separation of tracer pairs was found to be slower for smaller r . The g value used in the simplified model also decreases with decreasing r . In the dashed lines for $r = 1, 0.5$ and 0.25η , the value of g is set to 1, 0.7 and 0.5, respectively.

The relative speed of the smallest particles ($St \simeq 0.1$)

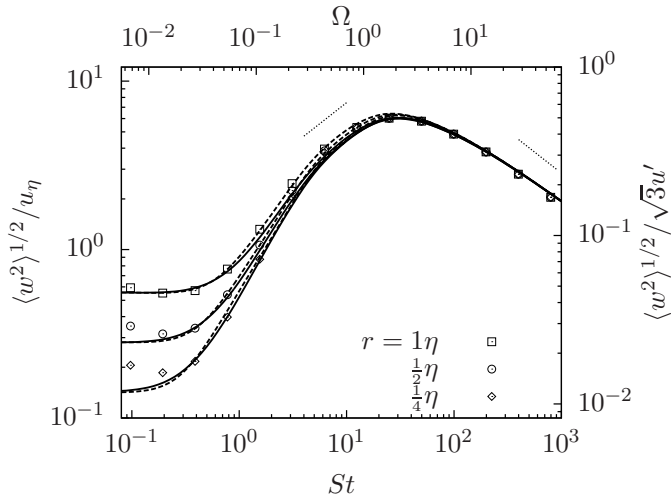


FIG. 7.— The 3D rms relative velocity, $\langle w^2 \rangle^{1/2}$, at $r = 1$ (squares), 0.5 (circles) and 0.25η (diamonds). Solid and dashed lines are predictions of the PP10 model with bi-exponential Φ_2 and the simplified model with single-exponential Φ_2 , respectively. A two-phase separation connecting at $\tau = -\tau_p$ is adopted in both models. In the PP10 model, the Richardson constant g is set to 1.6, 1.3 and 1.0 for solid lines from top to bottom. The corresponding g values used in the simplified model are 1, 0.7 and 0.5, respectively. The dotted line segments denote $St^{1/2}$ and $St^{-1/2}$ scalings.

in our simulation appears to be larger than the second smallest ones ($St \simeq 0.2$), especially at smaller r . Slight dips are seen at $St \simeq 0.2$ (Fig. 7). This is in contrast to the S-T formula, which predicts the relative speed at a given r is constant at sufficiently small St . These dips are not expected from the physical picture of our model either, and their existence is thus questionable. One possibility is that the rise of the relative speed toward $St \simeq 0.1$ is a numerical artifact. This suspicion is based on the consideration that the trajectory integration in our simulation is likely less accurate for smaller particles. The accuracy of the trajectory computation depends on the integration time step relative to the particle friction time. Since the time step is the same for all particles, the accuracy would be lower for smaller particles. This suggests the rise of the relative speed toward $St \simeq 0.1$ may be caused by numerical errors in the trajectory integration. We expect it to disappear as the computation accuracy increases. This will be tested by future simulations with a better temporal resolution for the integration of small particles.

The S-T formula predicts that $\langle w^2 \rangle^{1/2}$ scales linearly with r in the $St \ll 1$ limit. This linear scaling is not confirmed by our simulation result for the smallest particles. A rough power fit for the rms relative speed as a function of r gives $\langle w^2 \rangle^{1/2} \propto r^{0.78}$ at $St = 0.1 - 0.2$. This means that, for particles with $St \simeq 0.1 - 0.2$, the S-T formula is already invalid at $r \lesssim 0.5\eta$. At a given St , a critical particle distance is expected, below which the linear scaling does not apply. The physical reason is that, as r decreases, the local flow velocity difference across r becomes smaller, and it is easier for the particle memory of the flow velocity difference in the past to provide a significant contribution, which tends to invalidate the S-T prediction. Equivalently, at a given r , the S-T formula is valid only below a critical St . In Fig. 7, the lines for $r \lesssim 0.5\eta$ show that, as St decreases to

$\simeq 0.2$, the relative speed predicted by our model is not flat yet, suggesting a significant contribution from the particle memory. At sufficiently small St , the rms relative speed at a distance $r \lesssim 0.5\eta$ is expected to finally become constant. To verify this, a simulation of higher accuracy for small particles is needed to fix the problem of the artificial rise in the relative velocity toward $St \simeq 0.1$. As mentioned earlier, the rise is expected to disappear as the computation accuracy for the smallest particles increases.

Our model does not directly consider the sling effect (Falkovich et al. 2002, Falkovich and Pumir 2007) or the related caustic formation (Wilkinson & Mehlig 2005; Wilkinson et al. 2006; Gustavsson & Mehlig 2011). The effect of slings is usually explored for small particles with $St \lesssim 1$. As mentioned in the Introduction, it corresponds to crossing of particle trajectories that occurs at fluid streamlines with high curvature or local flow regions with large velocity gradient. In our physical picture, the effect of slings or caustics could be viewed as a contribution to the backward particle separation. In the sling events, the particle pairs come together from a farther distance than the average. Based on the model of Wilkinson et al. (2006) and Gustavsson & Mehlig (2011), the frequency of slings or caustic formation increases with St . The effect also becomes more important as r decreases, and would finally dominate over the S-T contribution at a sufficiently small r . Falkovich and Pumir (2007) showed that the sling effect is already significant at $St \simeq 0.2$. In Fig. 7, we see that our model prediction underestimates the relative velocity of $St = 0.2$ particles at $r \lesssim 0.5\eta$. A likely reason is that the sling effect is not sufficiently reflected by the assumed backward separation behavior. In principle, the effect can be better incorporated into our model by directly and accurately evaluating the frequency of such events and their contribution to the backward separation. We will discuss the effect of slings or caustics on the particle collision rate in details in §7. For $St \lesssim 1$ particles, the sling events are rare. At $St \gtrsim 3$, these events become very frequent, and essentially all particle pairs at $r \lesssim \eta$ should be counted as sling or caustic pairs (§7.2). In our physical picture, this corresponds to the fact that the backward separation of $St \gtrsim 3$ particle pairs at a friction timescale ago is significantly larger the initial distance, r .

Concerning the r -dependence of $\langle w^2 \rangle^{1/2}$ for $St \lesssim 6.2$ particles seen in Fig. 7, a fundamental question is whether the dependence disappears as r further decreases below $\eta/4$, or, equivalently, whether $\langle w^2 \rangle^{1/2}$ approaches a finite constant as $r \rightarrow 0$. Based on the prediction of Gustavsson & Mehlig (2011), it is possible that, for particles that exhibit significant clustering (see §7.1), the overall rms relative velocity may approach 0 as $r \rightarrow 0$. In the case, $\langle w^2 \rangle^{1/2}$ for $St \lesssim 6.2$ particles would not converge with decreasing r , and thus in principle could not be resolved. Intuitively, the rms relative speed, $\langle w^2 \rangle^{1/2}$, of intermediate particles with $1 \lesssim St \lesssim 6.2$ may converge at sufficiently small r , while, for $St \ll 1$ particles, $\langle w^2 \rangle^{1/2}$ may decrease to zero as $r \rightarrow 0$. The convergence of $\langle w^2 \rangle^{1/2}$ for $St \lesssim 6.2$ particles needs to be checked with larger simulations that allow accurate measurements at $r \ll \eta/4$.

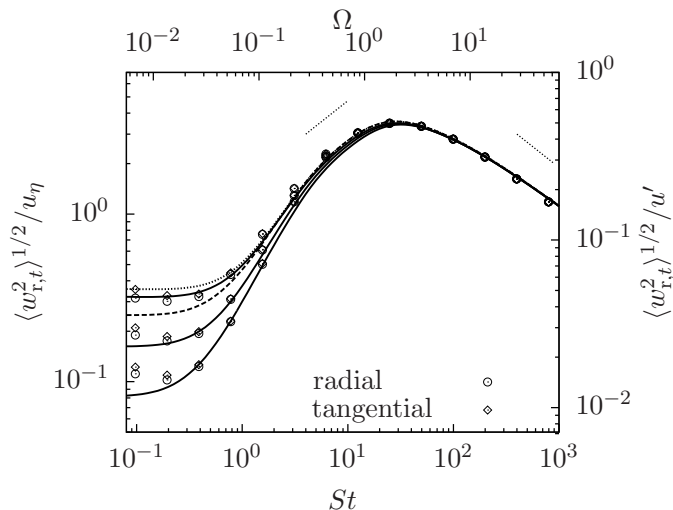


FIG. 8.— The rms relative speeds in the radial ($\langle w_r^2 \rangle^{1/2}$; circles) and tangential ($\langle w_t^2 \rangle^{1/2}$; diamonds) directions. From top to bottom, data points show simulation results at $r = 1, 0.5$, and 0.25η , respectively. Lines are predictions of the PP10 model. The solid lines adopt eq. (27) for the angular average of S_{Tij} , which predicts that $\langle w_r^2 \rangle = \langle w_t^2 \rangle = \frac{1}{3}\langle w^2 \rangle$. The particle separation behavior assumed here is exactly the same as in the solid lines in Fig. 7 for the 3D rms. The Richardson constant, g , is set to 1.6, 1.3 and 1.0 for $r = 1, 0.5$, and 0.25η , respectively. The dashed and dotted lines for $r = 1\eta$ are solutions of eq. (31) for the radial and tangential relative speeds, respectively. The two lines reproduce the S-T prediction for $\langle w_r^2 \rangle^{1/2}$ and $\langle w_t^2 \rangle^{1/2}$ at $St \ll 1$.

6.1.2. The Radial and Tangential Relative Speeds

Fig. 8 shows the rms relative speeds in the radial (circles) and tangential (diamonds) directions for particle pairs at $r = 1, 0.5$ and 0.25η . At $St \lesssim 1$, the tangential rms speed, $\langle w_t^2 \rangle^{1/2}$, is slightly larger (by $\simeq 10\%$) than the radial rms, $\langle w_r^2 \rangle^{1/2}$. This difference is considerably smaller than the prediction of the S-T formula, eq. (11), which indicates that for $St \ll 1$ particles the tangential rms relative speed should be larger than the radial rms by a factor of $\sqrt{2}$. Our data implies that this prediction is not valid at least for particles with $St \gtrsim 0.1$. It remains to be checked whether the factor of $\sqrt{2}$ difference between $\langle w_r^2 \rangle^{1/2}$ and $\langle w_t^2 \rangle^{1/2}$ would be recovered at smaller Stokes numbers. In Fig. 8, we see that $\langle w_r^2 \rangle^{1/2}$ and $\langle w_t^2 \rangle^{1/2}$ become exactly equal at $St \gtrsim 1$.

The solid lines in Fig. 8 correspond to the prediction of the PP10 model using eq. (27) for the angular average, $\langle S_{Tij} \rangle_{\text{ang}}$, of the trajectory structure tensor. The equation assumes that the direction of the particle separation \mathbf{R} at any time is completely random, and predicts that $\langle w_r^2 \rangle = \langle w_t^2 \rangle = \frac{1}{3}\langle w^2 \rangle$ for all particles (§3.2.2). This prediction is in good agreement with our simulation data. The equality of the radial and tangential rms speeds for $St \gtrsim 1$ is expected, because the separation \mathbf{R} of these particles at a friction timescale ago is significantly larger than the initial distance, r , and its direction is likely random with respect to \mathbf{r} . On the other hand, the near equality of $\langle w_r^2 \rangle^{1/2}$ and $\langle w_t^2 \rangle^{1/2}$ at $St \sim 0.1 - 0.2$ is somewhat surprising. For $r = 1\eta$, the backward separation of these particles does not contribute to make the 3D rms, $\langle w^2 \rangle^{1/2}$, of the relative velocity significantly larger than the S-T prediction. This suggests that the near equality

of $\langle w_r^2 \rangle^{1/2}$ and $\langle w_t^2 \rangle^{1/2}$ is due to a conversion of the relative velocity from the tangential to the radial direction. The conversion is probably caused by the deviation of the particle trajectories from the fluid elements. Even though the deviation does not considerably change the 3D amplitude $\langle w^2 \rangle^{1/2}$ at $r \simeq 1\eta$, it could efficiently alter the direction of \mathbf{w} with respect to \mathbf{r} . The trajectory deviation is stochastic, and thus tends to randomize the direction of \mathbf{w} and equalize its radial and tangential components. This reduces the tangential-to-radial ratio. The randomization effect is expected to be more efficient in the slings events, where the particles are shot out of the flow streamlines, and encounter the trajectories of other particles. At smaller r , the contribution from the backward separation to the 3D rms of the relative velocity is larger, and the random direction of the particle separation in the past also tends to equalize the radial and tangential components. In the $r \rightarrow 0$ limit, we would expect that $\langle w_r^2 \rangle^{1/2}$ and $\langle w_t^2 \rangle^{1/2}$ are exactly equal at all St .

When computing the solid lines, we used a bi-exponential form for Φ_2 , and the separation behavior adopted here is exactly the same as for the solid lines in Fig. 7 for the 3D rms. The solid lines shown here correspond to those in Fig. 7 divided by $\sqrt{3}$. The Richardson constant is set to 1.6, 1.3 and 1.0 in the three lines for $r = 1, 0.5$, and 0.25η , respectively.

The dashed and dotted lines for $r = 1\eta$ are the solutions of eq. (31) for the radial and tangential rms relative speeds, respectively. Eq. (31) was derived from eq. (26) for $\langle S_{Tij} \rangle_{\text{ang}}$, which assumes that the direction of the separation change $\Delta\mathbf{R}$ (rather than \mathbf{R} itself) is random. When solving eq. (31), we used the same two-phase separation behavior (with $g = 1.6$) as in the corresponding solid line. At small St , the dashed and solid lines reproduce the S-T prediction that $\langle w_t^2 \rangle = 2\langle w_r^2 \rangle$. The discrepancy between the simulation data and the S-T formula implies that, for particles with $0.1 \lesssim St \lesssim 1$, the direction of \mathbf{R} is more random than assumed in eq. (26).

The dependence of the radial and tangential rms relative speeds on r is similar to that of the 3D rms (see Fig. 7). In an attempt to roughly fit them as power-law functions of r , we find that $\langle w_r^2 \rangle^{1/2}$ and $\langle w_t^2 \rangle^{1/2}$ scale with r as $\propto r^{0.78}$ at $St = 0.1 - 0.2$. Similar to the 3D rms, the slight dips at $St \simeq 0.2$ for both $\langle w_r^2 \rangle^{1/2}$ and $\langle w_t^2 \rangle^{1/2}$ may be due to a numerical artifact.

The simulations of Wang et al. (2000) found that the tangential-to-radial variance ratio, $\langle w_t^2 \rangle / \langle w_r^2 \rangle$, is $\simeq 1.5 - 1.6$ at $St \simeq 0.1 - 0.2$. This is closer to the S-T prediction and larger than the corresponding value ($1.2 - 1.3$) in our simulation. This is probably because our flow has a much larger Reynolds number. Although Wang et al. (2000) claimed that the ratio is independent of Re_λ based on several simulations with $Re_\lambda \lesssim 75$, it is not clear if this is also true at $Re_\lambda \gg 75$. As speculated above, it is the deviation of the particle trajectories from the flow elements that tends to equalize the radial and tangential relative speeds of small particles. Clearly, the trajectory deviation would be larger in flow regions with larger velocity gradients, where the flow experiences a faster velocity change. The probability of finding large flow velocity gradients hence large trajectory deviations increases with Re_λ . Therefore, the tangential-to-radial

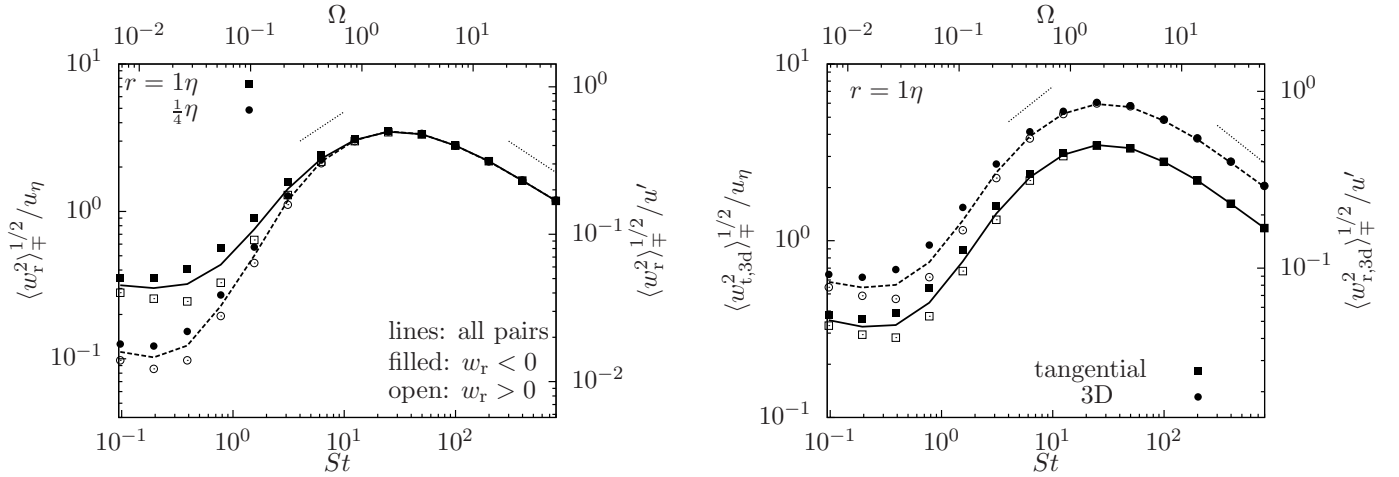


FIG. 9.— The rms relative speeds for approaching ($w_r < 0$; filled symbols) or separating ($w_r > 0$; open symbols) particle pairs. Lines correspond to the overall rms relative speeds counting all pairs. Left panel: The radial rms speed $\langle w_r^2 \rangle_{\pm}^{1/2}$ in the minus and plus groups with $r = 1\eta$ (squares) and 0.25η (circles). Right panels: the tangential (squares) and 3D (circles) rms relative speeds for particle pairs at $r = 1\eta$. The dotted line segments denote $St^{1/2}$ and $St^{-1/2}$ scalings.

ratio is likely smaller at higher Re_{λ} . For $St \lesssim 1$ particles, the sling events occur in regions with extreme flow velocity gradients, and the frequency of slings would increase with Re_{λ} (Falkovich and Pumir 2007). This also tends to reduce the tangential-to-radial ratio. However, we cannot rule out the possibility that the trajectory integration of the smallest particles in our simulation is not sufficiently accurate to allow an accurate measurement of $\langle w_t^2 \rangle / \langle w_r^2 \rangle$ at small St .

6.1.3. Approaching and Separating Particle Pairs

So far, our analysis for the particle relative velocity included all particle pairs at given distances. However, not all pairs at a small distance lead to collisions. Particles with a negative radial relative velocity, $w_r < 0$, approach each other and may collide, while particle pairs with $w_r > 0$ move away from each other. Since the final goal of our study is to examine the particle collisions, it is appropriate to split particle pairs at a given distance into two groups with $w_r < 0$ and $w_r \geq 0$, respectively. We refer to them as the minus and plus groups. Although only the first group is relevant for particle collisions, it is theoretically interesting to compare the two groups.

For the radial component, w_r , of the relative velocity, we denote the variances in the minus and plus groups as $\langle w_r^2 \rangle_-$ and $\langle w_r^2 \rangle_+$, respectively. In terms of the PDF, $P(w_r, St)$, of w_r , the variances are written as $\langle w_r^2 \rangle_- = \int_{-\infty}^0 w_r^2 P(w_r, St) dw_r / \int_{-\infty}^0 P(w_r, St) dw_r$ and $\langle w_r^2 \rangle_+ = \int_0^{\infty} w_r^2 P(w_r, St) dw_r / \int_0^{\infty} P(w_r, St) dw_r$. We denote the PDFs of the tangential component in the minus and plus groups as conditional PDFs, $P(w_t | w_r < 0, St)$ and $P(w_t | w_r > 0, St)$. The tangential variances in the two groups are then given by $\langle w_t^2 \rangle_{\pm} = \int_{-\infty}^{\infty} w_t^2 P(w_t | w_r \leq 0, St) dw_t$. Similarly, for the 3D amplitude, $|\mathbf{w}|$, the minus and plus variances are expressed as $\langle w^2 \rangle_{\pm} = \int_{-\infty}^{\infty} w^2 P(|\mathbf{w}| | w_r \leq 0, St) d|\mathbf{w}|$, where $P(|\mathbf{w}| | w_r \leq 0, St)$ are the PDFs of $|\mathbf{w}|$ for approaching and separating pairs. The PDFs, $P(w_r, St)$, $P(w_t | w_r \leq 0, St)$, and $P(|\mathbf{w}| | w_r \leq 0, St)$, will be studied in §6.2.

The data points in the left panel of Fig. (9) show the

radial rms relative speeds of particle pairs at $r = 1\eta$ (squares) and 0.25η (circles). The right panel plots the tangential (squares) and 3D (circles) rms speeds at 1η . In both panels, the filled and open symbols correspond to particle pairs in the minus and plus groups, respectively, and the lines plot the overall rms relative velocities counting all particle pairs. If the velocity of $St \ll 1$ particles closely follow the flow velocity, we expect that $\langle w_r^2 \rangle_{\pm}$ are determined by the variances of the longitudinal flow velocity increments, $\langle \Delta u_r^2 \rangle_{\pm}$, for negative and positive Δu_r , respectively. The definition of $\langle \Delta u_r^2 \rangle_{\pm}$ is given in Appendix B, and they correspond to the fluctuation amplitudes in the left and right wings of the PDF of Δu_r . In Appendix B, we find the ratio $\langle \Delta u_r^2 \rangle_- / \langle \Delta u_r^2 \rangle_+$ is 1.47 at the size, Δx , of the computation cell. This suggests that, in the $St \rightarrow 0$ limit, $\langle w_r^2 \rangle_-^{1/2}$ would be larger than $\langle w_r^2 \rangle_+^{1/2}$ by $\simeq 20\%$. The simulation result confirms this expectation. At $St \simeq 0.1$, $\langle w_r^2 \rangle_-^{1/2}$ is larger than $\langle w_r^2 \rangle_+^{1/2}$ by $\simeq 25\%$ for both $r = 1$ and 0.25η (see the left panel of Fig. 9). Using a similar analysis to the tangential component gives $\langle w_t^2 \rangle_{\pm}^{1/2} \simeq \langle \Delta u_t^2 \rangle_{\pm}^{1/2}$ for $St \ll 1$, where $\langle \Delta u_t^2 \rangle_{\pm}$ are variances of the transverse flow velocity increment, Δu_t , conditioned on the sign of the longitudinal increment Δu_r (see Appendix B). The ratio $\langle w_t^2 \rangle_-^{1/2} / \langle w_t^2 \rangle_+^{1/2}$ is found to be 1.16 at $St = 0.1 - 0.2$, consistent with the ratio of $\langle \Delta u_t^2 \rangle_-$ to $\langle \Delta u_t^2 \rangle_+$ at the grid cell size, Δx (see Appendix B). For the the 3D amplitude ($\langle w^2 \rangle_{\pm}^{1/2}$), the rms ratio between the minus and plus groups is 1.18 at $St \ll 1$.

As St increases, the relative speed for the plus group first decreases slightly and reaches a minimum at $St \simeq 0.4$ in all cases with $r = 1\eta$. This can be explained by considering the effects of the particle memory and the particle separation backward in time. Particle pairs in the plus group with $w_r > 0$ are coming from smaller distances, meaning that the separation of the particles was smaller in the near past. As St increases from 0.1 to 0.4, the contribution from the particle memory of the flow velocity difference becomes more important, and this con-

tribution tends to reduce the relative speed since the particle distance was smaller in the immediate past. However, if we look back further into the past (i.e., at larger $|\tau|$), the two particles may pass each other, and their distance would make a transition from decreasing to increasing. This explains the increase of $\langle w_r^2 \rangle_+$, $\langle w_t^2 \rangle_+$, and $\langle w^2 \rangle_+$ at $St \gtrsim 0.4$. The minimum of $\langle w_r^2 \rangle_+$ for $r = 0.25\eta$ appears at $St = 0.2$ instead of $St = 0.4$, because, for smaller r , it takes a shorter time for the particle distance in the past to change from decreasing to increasing.

For approaching particles in the minus group, the particle distance would increase monotonically toward the past. Therefore, the relative speed for this group is expected to increase monotonically as τ_p increases from 0 to $\simeq T_L$. This is confirmed by the filled data points in Fig. 9, except the slight dips at $St \simeq 0.2$. These dips are not expected, and again may be caused by insufficient numerical accuracy in the trajectory integration of the smallest particles (§6.1.1). Fig. 9 shows that approaching particles tend to have a larger relative speed than separating ones. The difference between the two groups first increases with St and then decreases at $St \geq 1$. At $St \gtrsim 6.2$, the rms relative speeds in the two groups are close and coincide with the overall rms. The reason is that, for these larger particles, the separation of the particle pairs in the two groups at a friction timescale ago becomes insensitive to the “initial” condition around $\tau = 0$.

The asymmetry in the relative velocity of $St \lesssim 6.2$ particles is related to the spatial clustering of these particles. The fact that approaching pairs move faster than separating ones may imply that particles tend to cluster at small distances to a reference particle (see also §7.1). An interesting question is whether the asymmetry found at $\eta/4 \lesssim r \lesssim \eta$ would exist also in the $r \rightarrow 0$ limit. We expect the asymmetry to decrease with decreasing r because the difference caused by the different separation behaviors in the near past for approaching and separating pairs would be smaller at smaller r . However, it is not clear whether it completely vanishes as $r \rightarrow 0$. For example, the asymmetry in the flow velocity difference, Δu , persists at any tiny but finite r , and it may leave an imprint on the relative velocity of small particles (say, with $St \lesssim 1$). The actual behavior of the asymmetry as $r \rightarrow 0$ will be checked by future simulations that allow to resolve smaller r . The prediction of the PP10 model was made only for the overall rms, and it could be modified to give separate predictions for approaching and separating pairs if the different separation behaviors of the two groups are properly specified. We also find that $\langle w_r^2 \rangle_-^{1/2}$ and $\langle w_t^2 \rangle_-^{1/2}$ almost coincide for all St , suggesting that each relative velocity component would provide equal amount of collision energy. On average, the radial component contributes 1/3 collision energy, while the rest 2/3 is from the two tangential components.

6.2. The PDF of the Particle Relative Velocity

An accurate estimate of the PDF of the particle collision velocity is important for modeling the growth and evolution of dust particles in protoplanetary disks. As mentioned in the Introduction, the outcome of particle collisions depends on the collision velocity, and due to the random nature of the turbulent-induced collision veloc-

ity, collisions of particles with exactly the same properties may have different outcomes, and thus using a single value, e.g., the rms, for the collision speed of particles of a given size is insufficient. The probability distribution of the collision velocity is needed to calculate the fractions of collisions resulting in sticking, bouncing or fragmentation.

In this section, we explore the probability distribution of the particle relative velocity. We will primarily show the PDFs at $r = \eta$, where the statistical measurements are most sufficient and accurate. The measured PDFs for $St \gtrsim 10$ particles already converge at $r \simeq \eta$. On the other hand, for smaller particles the PDFs have an r -dependence at $r \gtrsim \eta/4$, and an appropriate extrapolation to $r \rightarrow 0$ using larger simulations will be needed for the application to dust particle collisions.

The physical picture of PP10 shows that the relative velocity of inertial particles depends on the flow velocity difference the particle pairs saw within a memory timescale or so. This suggests that the statistics of the velocity difference in the carrier flow is crucial for the understanding of the relative velocity PDF of inertial particles. Therefore, we analyzed the PDFs, $P_u(\Delta u_r, \ell)$ and $P_u(\Delta u_t, \ell)$, of the longitudinal and transverse velocity increments, Δu_r and Δu_t , as functions of the length scale, ℓ , in our simulated flow. The results are discussed in details in Appendix B. The flow velocity PDFs are used in the physical explanation for the PDF of the particle relative velocity as a function of particle inertia in §6.2.2.

6.2.1. The PDFs of the radial and tangential components

In Fig. 10, we show the PDF, $P(w_r, St)$, of the radial component of the relative velocity as a function of the Stokes number. All the PDFs are measured at a particle distance of 1η . The relative speed is normalized to the Kolmogorov velocity, u_η , and the 1D flow rms velocity, u' , on the bottom and top X-axes, respectively. Each PDF is normalized to its value at the central peak. In the left panel, the thin dashed line corresponds to the PDF of tracer particles ($St = 0$) at 1η . The shape of this line is found to be identical to the PDF, $P_u(\Delta u_r, \ell)$, of the longitudinal flow velocity increment, Δu_r , at the computational cell size ($\ell = 1.7\eta$; see the top line in the left panel of Fig. 21 in Appendix B). This is expected as tracer particles exactly follow the flow velocity, and the shape of $P_u(\Delta u_r, \ell)$ is independent of ℓ in the dissipation range (Appendix B). The solid color lines of increasing width show the PDFs of larger particles. This corresponds to the increase of the rms relative speed with St for $St \lesssim 24.9$ (see Figs. 8 and 9). For $St \leq 1.55$, the PDF of w_r has a negative skewness, which is inherited from the flow velocity PDF $P_u(\Delta u_r, \ell)$. The PDF becomes symmetric at $St \gtrsim 3.21$. It is interesting to note that, as St increases, the tails of the PDFs become broader, while the innermost part remains unaffected and the same as the PDF of the tracer particles. As to be shown in §6.2.2, the amplification of the PDF tails correspond to the effect of slings or caustic formation. Due to the tail amplification, the overall PDF shape becomes fatter⁸ as St increases to $\simeq 1.55$. With increasing St , the

⁸ For definiteness, throughout the paper we use “fat” or “thin” to describe the shape of the PDF. The fatness can be quantified,

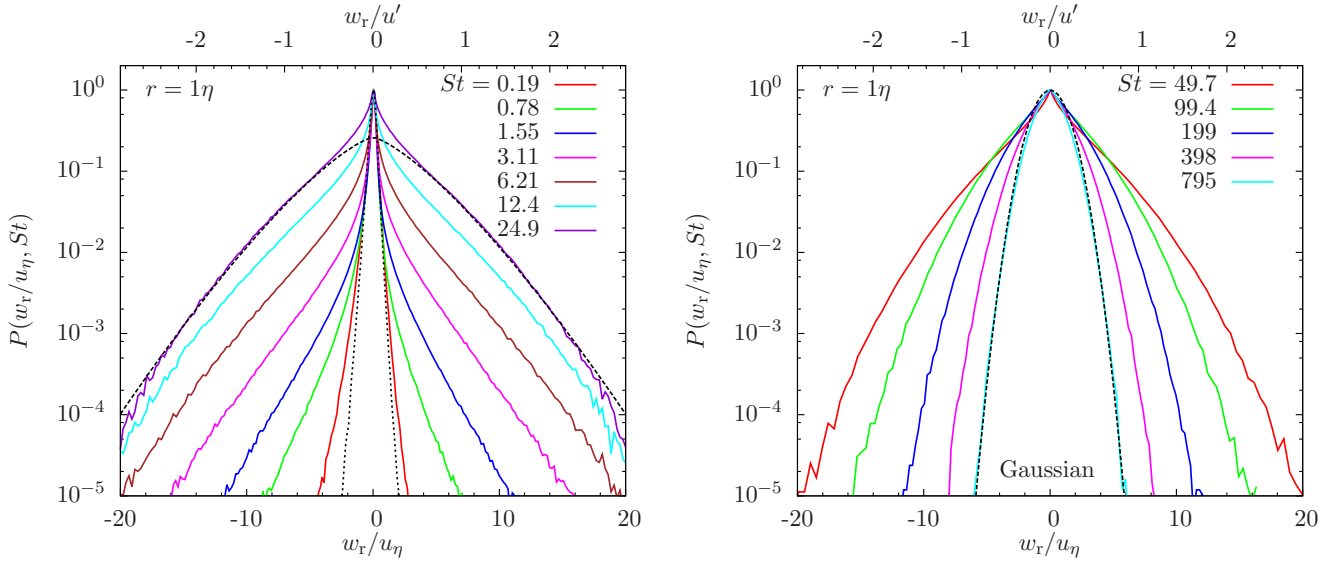


FIG. 10.— The PDF of the radial component (w_r) of the relative velocity at $r = 1\eta$ as a function of St . The relative speed is normalized by the Kolmogorov velocity, u_η , and the rms flow velocity, u' , on bottom and top axes, respectively. Each PDF is normalized to its peak value at $w_r = 0$. The left panel shows the PDFs for particles with $St \leq 24.9$, while the right panel shows results for $St \geq 49.7$ particles. The dotted line in the left panel is the PDF of the radial relative speed of tracer particles ($St = 0$). The dashed line in this panel is the stretched exponential function with $\alpha = 4/3$, which provides a good fit for the PDF tails of $St = 24.9$ particles. In the right panel, the dashed line corresponds to the Gaussian fit to the largest particles in our simulation. One can use $\Omega = St/14.4$ and $\Omega_{\text{eddy}} = St/19.2$ to convert the normalization of the particle friction time.

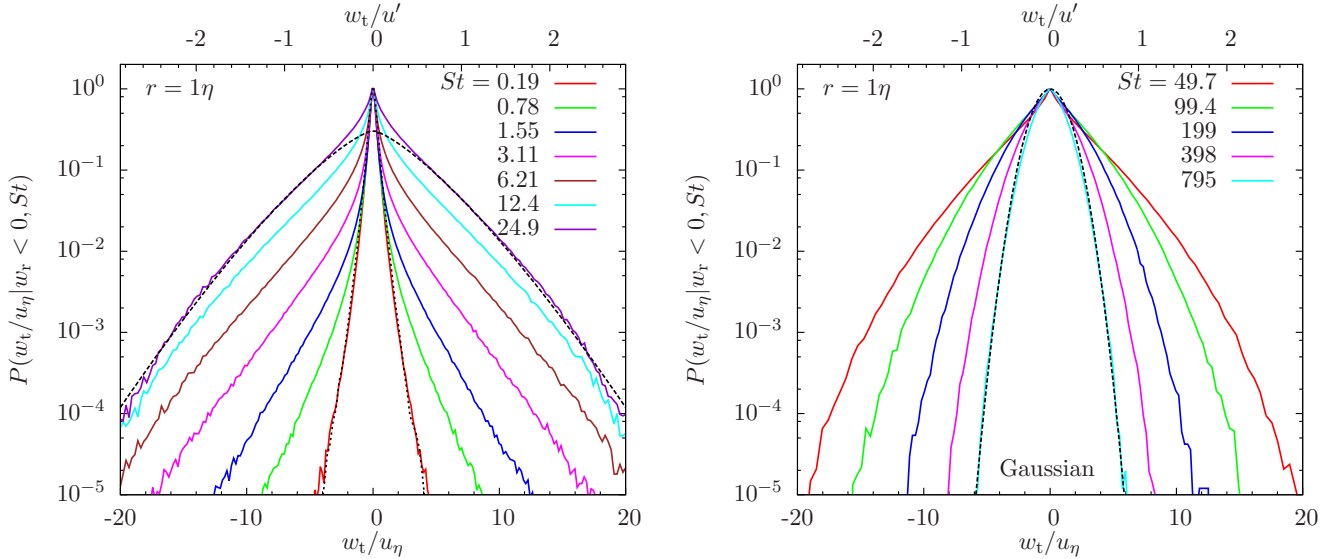


FIG. 11.— The PDFs of the tangential relative velocity, w_t , conditioned on $w_r < 0$. The PDFs are measured from approaching particle pairs. The normalizations are the same as in Fig. 10. The left and right panels show results for particles with $St \leq 24.9$ and $St \geq 49.7$, respectively. The dotted line in the left panel is the PDF of the tangential relative velocity of tracer particles ($St = 0$) conditioned on $w_r < 0$. The dashed line in this panel is a stretched exponential function with $\alpha = 4/3$. The dashed line in the right panel corresponds to the Gaussian fit for $St = 795$ particles.

amplification effect proceeds towards the inner parts of the PDF, leading to a sharp cusp-like shape at the center, especially for $St \gtrsim 3.11$. For particles with $St \gtrsim 3.11$, the slope of the outer parts of the PDF tends to steepen when extending to higher tails, i.e., the PDF shape becomes thinner at larger $|w_r|$. This thinning trend toward the high tails causes a decrease in the overall fatness of the PDF for St above 3.11.

In the right panel, the PDF becomes narrower as St

e.g., by kurtosis. On the other hand, the extension or width of the PDF, corresponding to the rms, is described as “broad” or “narrow”.

increases above 49.7, corresponding to the decrease of the rms relative velocity with St in the large particle limit (Figs. 8 and 9). For $St \geq 49.7$ ($\Omega \geq 3.4$), the friction timescale is larger than the correlation timescale (T_L) of the flow velocity at largest scales, meaning that the memory time of the flow velocity is shorter than the memory of the particles. This induces a factor of T_L/τ_p in the relative velocity variance (§3.2.4), causing a decrease of the PDF width at larger St . The dotted line in the right panel is the Gaussian fit to the PDF of the largest particles ($St = 795$; or $\Omega = 54$) in our simulation. For these particles, τ_p is 54 times larger than T_L , suggesting

that the assumption of a Gaussian relative velocity PDF applies only in the extreme limit $\tau_p \gg T_L$.

Fig. 11 shows the PDF, $P(w_t|w_r < 0, \tau_p)$, of a tangential component of the relative velocity conditioned on $w_r < 0$. The measurement of $P(w_t|w_r < 0, \tau_p)$ only counts particle pairs approaching each other. The figure is plot in the same way as Fig. 10 for the radial component. Again, the thin dashed line in the left panel is for tracer particles ($St = 0$). It corresponds to the PDF of the transverse difference, Δu_t , of the flow velocity conditioned on $\Delta u_r < 0$. The shape of $P(w_t|w_r < 0, 0)$ for tracer particles at $r = 1\eta$ is close to the dashed line in the right panel of Fig. 21 for $P_u(\widehat{\Delta u}_t|\Delta u_r < 0, \ell)$ at $\ell = 1.7\eta$ (Appendix B). The qualitative behavior of $P(w_t|w_r < 0, St)$ as a functions of St is similar to that of $P(w_r, St)$.

For $St = 0.19$ particles, the radial PDF tails are significantly amplified with respect to tracers (Fig. 10), while the conditional PDF of the tangential component almost coincides with the tracer PDF (Fig. 11). From the physical picture for the PDF behavior given in §6.2.2, the effects of the particle memory and the backward separation tend to amplify the PDF tails of $St = 0.19$ particles. For the tangential PDF, this amplification effect is counteracted by the conversion of the relative velocity from the tangential to the radial direction, which reduces the PDF width of the tangential component. As discussed in §6.1.2, the conversion is caused by the deviation of inertial particle trajectories from the flow elements and the particle memory of the flow velocity in the past, which randomize the direction of \mathbf{w} relative to the particle separation, \mathbf{r} . The conversion is expected to be more efficient at the PDF tails (corresponding to the sling events). It appears that the two opposite effects cancel out for the tangential PDF of $St \simeq 0.19$ particles, as it almost coincides with the dotted line for tracers. On the other hand, both effects broaden the PDF of the radial component, leading to significantly amplified tails with respect to tracers.

Unlike $P(w_r, St)$, which has a negative skewness for $St \leq 1.55$ particles, $P(w_t|w_r < 0, St)$ is symmetric at all St . As mentioned earlier, the symmetry of the tangential PDF is expected from the statistical isotropy. We find that the left wing of the radial PDF $P(w_r, St)$ almost coincides with that of $P(w_t|w_r < 0, St)$ at all St . This is apparently due to the randomization of the relative velocity direction discussed above. On the other hand, the right wing of $P(w_r, St)$ is narrower than that of $P(w_t|w_r < 0, St)$, until it becomes symmetric at $St \gtrsim 3.11$. To study particle collisions, we are mainly interested in the PDFs for approaching pairs, i.e., the left wing of $P(w_r, St)$ and the entire tangential PDF, $P(w_t|w_r < 0, St)$, conditioned on $w_r < 0$.

We give a more quantitative description for the shape of $P(w_t|w_r < 0, St)$. The description also applies to the left wing of $P(w_r, St)$, as it coincides with the left wing of $P(w_t|w_r < 0, St)$. We first quantify the fatness of $P(w_t|w_r < 0, \tau_p)$ by computing the kurtosis, defined as $\langle w_t^4 \rangle_- / \langle w_t^2 \rangle_-^2$. At $r = 1\eta$, the kurtosis for $St = 0.1$ and 0.19 particles is $\simeq 11$, which is already much larger than 3 for a Gaussian PDF. With increasing St , the kurtosis first increases due to the tail amplification. It reaches a maximum value of 36 at $St = 0.78$, indicating extremely

high non-Gaussianity. The kurtosis decreases slightly to 32 at $St = 1.55$, and then drops rapidly and approaches $\simeq 3$ for the largest particles ($St = 795$). This decrease corresponds to the thinning trend of the high PDF tails for the large particles. We also measured the kurtosis for the PDFs at smaller r , and found that, for $St \lesssim 6.2$ particles, it keeps increasing as r decreases to $\eta/4$. The PDFs of these particles are fatter at smaller r because the effect of the tail amplification on the PDF shape is relatively stronger (see more detailed discussions in §6.2.3).

Following Sundaram & Collions (1997) and Wang et al. (2000), we attempted to fit $P(w_t|w_r < 0, \tau_p)$ with stretched exponential PDF. The generic stretched exponential function is given by,

$$P_{se}(x) = \frac{\alpha}{2\beta\Gamma(1/\alpha)} \exp\left[-\left(\frac{|x|}{\beta}\right)^\alpha\right], \quad (34)$$

where Γ is the Gamma function. The variance of P_{se} is given by $\beta^2\Gamma(3/\alpha)/\Gamma(1/\alpha)$. Thus, to fit a given PDF by eq. (34) with a chosen α , one can fix β by the variance of the PDF. The index α controls the PDF shape, and smaller α corresponds to fatter tails. The PDFs for $St = 0.1$ and 0.19 at $r = 1\eta$ almost have the same shape, and both can be fit by a stretched exponential with $\alpha = 0.67$. This value of α is consistent with that (0.7) used to fit the PDF tails of the flow velocity difference at $\ell = 1.7$ (see Appendix B and Fig. 21). At $St = 0.39, 0.78$ and 1.55 , the best-fit α is 0.52, 0.48, and 0.49, respectively. The decrease of α in the St range from 0.1 to 0.78 indicates increasing fatness of the PDF. The PDF shape at $St = 1.55$ is very close to that at $St = 0.78$.

For particles with $3.11 \leq St \leq 49.7$, the PDFs are more complicated, due to the existence of sharp cusps at the center and the steepening trend of the PDF slope toward to the far tails. These features cannot be captured simultaneously by a single stretched exponential function. It is, however, possible to fit these PDFs with a combination of two different stretched exponential functions for the cusp and the tails respectively. We postpone a detailed study of fitting functions for these intermediate particles to a future work. To give a quantitative idea for the PDF shape of these particles, here we simply list the best-fit α for the far tails without accounting for the central cusp. At $St = 3.11, 6.21, 12.4, 24.9$ and 49.7 , the best-fit α for the PDF tails is found to be 1, 1.1, 1.3, 1.33, and 1.45, respectively. The stretched exponential fits for the PDF tails of $St = 24.9$ ($\Omega = 1.7$) particles are shown as dotted lines in Figs. 10 and 11, where the index α is set to 4/3. Such a 4/3 stretched exponential PDF was predicted by Gustavsson et al. (2008) assuming an exact Gaussian flow velocity field with Kolmogorov scaling and a rapid temporal decorrelation. An alternative derivation for the 4/3 stretched exponential is given in §6.2.2 using the physical picture of the PP10 model. Our derivation does not assume a short temporal correlation for the flow velocity, and is thus more general than that of Gustavsson et al. (2008).

Starting from $St = 99$ ($\Omega = 6.8$), the central cusp becomes sufficiently small, leading to simpler PDF shapes. This allows the entire PDF to be satisfactorily fit by a single stretched exponential again. The measured α values for $St = 99, 199, 397$ and 795 are 1.5, 1.65, 1.75 and 1.9, respectively. Note that the PDF at $St = 795$

is close to Gaussian, but the best-fit value for α is actually 1.9 instead of 2. A similar trend of the PDF fatness and the best-fit α as a function of St was found in previous studies with low-resolution simulations (Sundaram & Collions 1997; Wang et al. 2000).

6.2.2. Physical picture for the PDF behavior

We give an explanation for the behavior of the relative velocity PDF using the physical picture of PP10, which was illustrated in Fig. 1. We first consider particles with $\tau_p \lesssim T_L$. In §3.2.4, we showed that the 3D relative velocity variance of these particles may be roughly estimated by $\langle w^2 \rangle \simeq S_{ii}(R_p)$, where S_{ij} is the flow structure tensor and R_p is the primary distance. For simplicity, we have neglected the effect of the temporal correlation function, Φ_2 , which may provide a factor, $\min(1, T(R_p)/\tau_p)$, of order of unity for particles with $\tau_p \lesssim T_L$. R_p was estimated by $R_p^2 = r^2 + \langle w^2 \rangle \tau_p^2$, assuming a ballistic backward separation within a friction timescale.

This picture for the rms relative velocity can be generalized to understand the behavior of the full PDF as a function of St . Consider a pair of particles at a distance r at time 0, and suppose their relative velocity is w . Applying the above physical picture to this particular pair, the relative speed, w , is estimated as $w \simeq \Delta u(r_p)$, where Δu is the flow velocity difference the two particles “saw” at $\tau = -\tau_p$ and r_p is the primary distance of this pair. We have used w and Δu to represent either the radial or the tangential component. The generalized picture suggests that the particle relative velocity samples the PDF of the flow velocity difference in a certain way. An immediate implication is that the particle relative velocity would inherit intermittency of the turbulent flow. Assuming a ballistic separation again, r_p is estimated by $(r^2 + \zeta w^2 \tau_p^2)^{1/2}$, where $\zeta \simeq 3$ corresponds to the difference between the 3D separation speed of the particle pair and the 1D speed in the radial or tangential direction. We point out that, for particles with $0.8 \lesssim St \lesssim 6.2$, it may not be valid to assume the contribution to the particle relative speed is dominated by the ballistic separation phase. As discussed in §6.1, the Richardson phase may provide a crucial contribution for these particles (see Fig. 6). However, using the ballistic assumption to estimate r_p would be sufficient for a qualitative understanding of the relative velocity PDF.

The above argument provides a satisfactory explanation for our simulation results for the relative speed PDF, $P(w, \tau_p)$, of particles with $\tau_p \lesssim T_L$. At $St \ll 1$, the primary distance $r_p (= (r^2 + \zeta w^2 \tau_p^2)^{1/2})$ for particle pairs in the inner part of the PDF (i.e., at $|w| \simeq 0$) would be close to r . As a result, the central PDF follows the PDF, $P_u(\Delta u, \ell)$, of the flow velocity difference at $\ell = r$, as observed in the left panels of Figs. 10 and 11. At the tails of $P(w, \tau_p)$, r_p is larger, and w samples the flow velocity PDF $P_u(\Delta u, \ell)$ at larger ℓ . This implies that higher tails broaden faster because $P_u(\Delta u, \ell)$ is wider at larger ℓ . The effect may be viewed as a “self-amplification” of the PDF tails. The tail amplification makes the overall shape of $P(w, \tau_p, St)$ at $St \lesssim 1$ considerably fatter than the PDF of tracer particles. As St increases, r_p becomes larger at the same value of w , and the “amplification” proceeds deeper into the inner part of the PDF, as seen in the left panels of Figs. 10 and 11. The overall PDF

broadening appears to be driven by the tail amplification. The amplification in the far PDF tails of $St \lesssim 1$ particles actually corresponds to the effects of slings or caustic formation. This is because the tail of $P(w, \tau_p)$ is associated with local flow regions with large velocity gradients, which are indeed where the slings or caustics are expected to occur. The tail amplification of $St \lesssim 1$ particles thus corresponds to the caustic contribution to the collision kernel in the model of Wilkinson et al. (2006).

As St increases above 1, the range of the central PDF that follows $P_u(\Delta u, \ell)$ becomes narrower, and the outer parts continue to get more extended. As discussed in §6.2.1, for $St \simeq 3.11$, the PDF tails show slope changes as they extend to high values of $|w|$. This is because different parts of the relative velocity PDF samples the flow velocity difference PDF, $P_u(\Delta u, \ell)$, at different length scales. As the fatness of $P_u(\Delta u, \ell)$ decreases with increasing ℓ (see Appendix B and Fig. 21), the shape of $P(w, \tau_p)$ at higher tails becomes thinner. This thinning trend occurs at smaller values of $|w|$ for particles with larger τ_p . The trend explains why the overall shape of the PDF becomes less fat as St increases above $\simeq 1$. Note that the central cusp for $3.11 \lesssim St \lesssim 24.9$ keeps a sharp shape, corresponding to $P_u(\Delta u, \ell)$ at small ℓ .

The fact that the broadening of the PDF starts from the tail amplification is not captured by the PP10 model for the rms relative velocity (§3.2). The model only considers the 2nd-order moments of the flow velocity increment, the particle separation and the particle relative velocity. This essentially assumes that the PDF shape does not considerably change with St , or the shape change of the PDF at the outer or tail parts does not have significant effects on the variance of the PDF. This gives rise to uncertainties in the prediction for the rms relative velocity because the PDF $P(w, St)$ is found to be very fat especially for $St \simeq 1$. Even the far tails give considerable contribution to the variance. The tail amplification also provides evidence for a positive correlation between the fluctuations in the flow velocity increment “seen” by the particle pair and the particle separation. The tails of $P(w, \tau_p)$ correspond to the PDF tails of both the flow velocity difference, Δu , and the the primary distance, r_p . In other words, in flow regions with Δu larger than its rms value, the backward separation of particles is also faster than the rms separation rate. As discussed in §3.2 and §6.1, the PP10 model neglects this correlation, and thus tends to underestimate the rms relative speed. The effect of the PDF tail amplification on the variance of the relative speed may be incorporated in the PP10 model if the correlation between Δu and the particle separation is properly accounted for. As mentioned in §6.1, accounting for this correlation, our model may fit the rms relative velocity with a smaller Richardson constant.

In principle, if the PDF, $P_u(\Delta u, \ell)$, of the flow velocity increment as a function of the scale ℓ is provided, one can derive the particle relative velocity PDF as a function of τ_p . For illustration, we consider a simplified example. We assume the flow velocity is exactly Gaussian, i.e.,

$$P_u(\Delta u, \ell) = \frac{1}{\sqrt{2\pi S(\ell)}} \exp\left(-\frac{\Delta u^2}{2S(\ell)}\right), \quad (35)$$

where $S(\ell)$ is the flow structure function or the variance of Δu at ℓ . To estimate the PDF, $P(w, \tau_p)$, of the particle

relative speed w , we ask the question what the probability is for two nearby particles to see a flow velocity difference of w at a friction timescale ago, i.e., at $\tau \simeq -\tau_p$. The probability is roughly estimated by $\propto P_u(w, r_p)$. Using eq. (35) for P_u and setting $r_p^2 = r^2 + \zeta w^2 \tau_p^2$, we have,

$$P(w, \tau_p) \propto \exp \left[-\frac{w^2}{2\xi S ((r^2 + \zeta w^2 \tau_p^2)^{1/2})} \right], \quad (36)$$

where it is assumed all uncertainties in the rough estimate can be absorbed in a parameter ξ . If r_p is in the inertial range of the flow, we may apply the Kolmogorov scaling $S(\ell) \propto \ell^{2/3}$. Further assuming that ξ is independent of w , we find that eq. (36) corresponds to a stretched exponential with $\alpha = 4/3$ (see eq. (34)) at $w \gg r/\tau_p$. This suggests that the relative speed of inertial-range particles would be non-Gaussian even if the flow statistics were exactly Gaussian. This non-Gaussianity originates purely from the particle dynamics, and is thus distinct from that inherited from the intermittency of the turbulent flow. In other words, we identified two sources, namely, the turbulent intermittency and the particle dynamics, that contribute to the non-Gaussianity of the particle relative velocity.

The predicted stretched exponential with $\alpha = 4/3$ was found to satisfactorily fit the PDF tails of $St = 24.9$ ($\Omega = 1.7$) particles (see dashed lines in the left panels of Figs. 10 and 11). For these particles, the two assumptions made in the derivation of the stretched exponential, i.e., Gaussianity and Kolmogorov scaling of the flow velocity, are both satisfied. We point out that these assumptions are strong, and thus the validity of the $4/3$ stretched exponential is quite limited. In fact, the prediction applies only to particles around the peak Stokes number, $St_m \simeq 30$. As discussed in §6.1, for particles with $St \simeq St_m$ in our simulation, the typical primary distance is around 200η . From Fig. 21 (Appendix B), we see that, above this length scale, the PDF of the flow velocity increment is close to Gaussian. Therefore, the Gaussian assumption made in eq. (36) is valid for $St \gtrsim St_m$. Also, Fig. 3 shows that 200η is toward the end of but still within the inertial range of the flow, meaning that, only for particles with $St \lesssim St_m$, can one apply the Kolmogorov scaling around the primary distance, r_p . These suggest that the two assumptions are simultaneously met only at $St \simeq St_m$. Our finding that the $4/3$ stretched exponential fits the PDF tails of $St = 24.9$ particles confirms the validity of our physical picture. The $4/3$ stretched exponential can also acceptably fit the PDF tails of $St = 12.4$ particles, but not for other particles. At the central part of the PDF of $St = 24.9$ (or 12.4) particles, both assumptions break down, and the $4/3$ stretched exponential does not apply.

We next consider large particles with $St \gtrsim St_m$. The friction time of these particles is much larger than T_L , and, accounting for the effect of the memory time of the flow velocity, the relative velocity of a given particle pair is roughly estimated by $w \simeq \Delta u(r_p)(T_L/\tau_p)^{1/2}$ (see §3.2.4). Due to the large friction time, r_p is typically comparable to or even larger than the integral scale, L , of the turbulent flow, and thus $P_u(\Delta u, \ell)$ at $\ell \simeq r_p$ is close to Gaussian. Since the flow velocity “seen” by $St \gtrsim St_m$ particles is typically Gaussian, the

PDF shape for their relative velocity is simpler than particles with intermediate τ_p (see Figs. 10 and 11). Using eq. (35) and the same analysis that led to eq. (36), we find $P(w, \tau_p) \propto \exp(-(w^2 \tau_p)/(2\xi S(r_p)T_L))$ for $St \gtrsim St_m$. The structure function, $S(\ell)$, starts to become constant at $\ell \gtrsim L$. Therefore, as τ_p increases, the typical r_p increases, and $S(r_p)$ becomes less dependent on r_p or w . As a consequence, the shape of the relative velocity PDF becomes less fat. In the limit $\tau_p \rightarrow \infty$, $S(r_p) \rightarrow 2u'^2$, and $P(w, \tau_p)$ finally approaches a Gaussian PDF with a variance $\propto u'^2 T_L/\tau_p$. As observed in Figs. 10 and 11, a nearly Gaussian PDF is indeed observed for the largest particles in our simulation.

The physical interpretation of the relative velocity PDF at the beginning of this subsection suggests that the PDF can be split into two parts. We use the PDF of w_r as an example, and, in particular, we consider the left wing of $P(w_r, St)$, corresponding to approaching particle pairs. We divide the PDF into two parts using a critical value, w_r^c . We choose w_r^c such that the inner PDF at $w_r^c \lesssim w_r \leq 0$ follows the flow velocity difference PDF, while in the outer part ($w_r \lesssim w_r^c$) the effects of the particle memory and the backward separation dominate. At a given r , w_r^c is roughly estimated by $-r/\tau_p$. This critical value is consistent with the physical picture of Falkovich et al. (2002) for the sling effect. Falkovich et al. (2002) showed that the velocity gradient of small particles ($St \lesssim 1$) blows up in a finite time once it exceeds τ_p^{-1} , leading to the sling events. At a given scale, r , this gradient criterion can be written as $|w_r|/r \gtrsim \tau_p^{-1}$. The model of Gustavsson & Mehlig (2011) suggests the same criterion for caustic formation. A similar critical value was proposed by Hubbard (2013) for inertial-range particles. Following Wilkinson et al. (2006), we name the central part ($w_r^c \lesssim w_r \leq 0$) and the tail part ($-\infty < w_r \lesssim w_r^c$) of the PDF as the continuous (or S-T) part and the caustic (sling) part, respectively. The terminology is based on the geometry in the position-momentum phase diagram of inertial particles (see Fig. 1 of Gustavsson and Mehlig 2011). Because the two parts have different scaling behaviors with r , the division is especially useful for the prediction of particle collisions in the $r \rightarrow 0$ limit, appropriate for applications to dust particles. In §7, we evaluate the collision kernel and show the contribution from the continuous part vanishes as $r \rightarrow 0$. Only the caustic particle pairs contribute to the collisions of nearly point-like particles. Therefore, to obtain the collision velocity PDF for the application to dust particles, one may exclude the contribution of the continuous part, and meanwhile push r to as small values as possible (e.g., Hubbard 2013). A detailed study of this topic will be conducted in a future work. Our study for the rms relative velocity in §6.1 did not split the particle pairs into the two types, and the main purpose was to understand the general physics of turbulence-induced relative velocity and to validate the physical picture of PP10.

6.2.3. The normalized PDF of the radial component

To see the shape of the PDF more clearly, we show in Fig. 12 the PDF of the radial component normalized to have unit variance. The radial relative speed is normalized to its rms value, $\langle w_r^2 \rangle^{1/2}$. The solid, dashed and dotted lines are the PDFs at $r = 1\eta, 0.5$ and

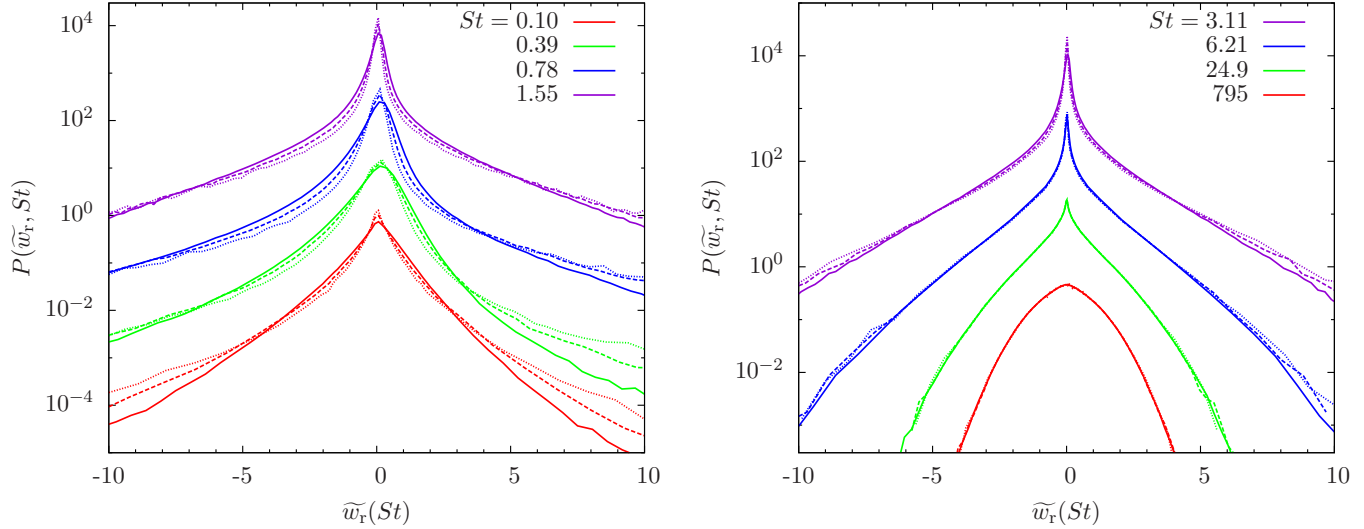


FIG. 12.— The normalized PDF of the radial relative velocity, w_r , as a function of the Stokes number St and the particle distance, r . All PDFs are normalized to have unit variance. The normalized relative speed is defined as $\tilde{w}_r = w_r / \langle w_r^2 \rangle^{1/2}$. The solid, dashed and dotted lines correspond to particle distance $r = 1, 0.5$ and 0.25η , respectively. The left panel plots the PDFs for particles with $St \leq 1.55$, while the right panel shows the results for larger particles with $St \geq 3.11$. In each panel, the bottom lines (i.e., $St = 0.1$ and $St = 795$) show the actual PDF values, and, for clarity, the upper lines for each larger St are shifted upward by a factor of 16. One may change the normalization of the friction time using $\Omega = St/14.4$ and $\Omega_{\text{eddy}} = St/19.2$.

0.25η , respectively, and the curves of different colors correspond to different St . The bottom curves in the left and right panels plot the actual PDF values for $St = 0.1$ and $St = 795$ ($\Omega = 54$), respectively. For clarity, the PDF curves are shifted upward by a factor of 16 for each larger St in the left panel or each smaller St in the right panel. The asymmetry of the PDFs at $St \lesssim 1.55$ is clearly seen.

As St increases from 0.1 to 1.55, the central part of the normalized PDF $P(\tilde{w}_r, St)$ becomes sharper. Before normalization, the innermost part of the PDF follows the PDF of the flow velocity difference, and is thus essentially the same for particles in the range $0.1 \leq St \leq 1.55$ (see Fig. 10). Since the rms of w_r increases with St due to the tail amplification, normalizing w_r by its rms tends to make the central part of the PDF sharper. At $St = 3.11$ and 6.21, the central cusp in the normalized PDF is very sharp. For St above 3.11, the outer PDF parts become less fat with increasing St . The shape of the normalized PDF is helpful to understand the behavior of the ratio $\langle |w_r| \rangle / \langle w_r^2 \rangle^{1/2}$ with St discussed in §7.1.

It is interesting to note that, as St increases from 0.1 to 0.39, the PDF, $P(\tilde{w}_r, St)$, at small to intermediate \tilde{w}_r in the right wing decreases. This corresponds to the decrease of $\langle w_r^2 \rangle_+^{1/2}$ in the St range from 0.1 to 0.39 (see the left panel of Fig. 9). The physical reason is that the right wing corresponds to separating particle pairs, and the particle distance decreases toward the near past. This leads to a decrease in the primary distance, r_p , for separating pairs with small to intermediate \tilde{w}_r , as St increases from 0.1 to 0.39. For the far right tail with large w_r , the particle pairs may quickly move past each other, and their distance starts to increase within a friction time in the past. This explains why the far right tail of $St = 0.39$ particles becomes slightly broader than that for $St = 0.1$. As St increases to 0.78, the PDF at immediate to large \tilde{w}_r in the right wing is significantly amplified, while the effect of the “initial” decrease of the

particle distance is still visible at small positive \tilde{w}_r . For $St > 0.78$, the particle memory is longer, and the “initial” separation phase does not cause a significant difference in the primary distances r_p of separating and approaching particle pairs. The two wings become almost symmetric at $St \gtrsim 3.11$.

For particles with $St \lesssim 3.11$, the normalized PDF has a dependence on the distance r for the range of r shown here. As r decreases, the central part of the normalized PDF becomes sharper, and the outer parts become slightly broader, leading to a fatter PDF shape at smaller r . Before the normalization, the central part of the PDF follows the flow velocity difference at r , and its width thus decreases linearly with r . On the other hand, the dependence of the tails on r is weaker because the primary distance, r_p , for particle pairs in the outer parts of the PDF has a larger contribution from backward separation. Also, as r decreases, the contribution from the outer parts of the PDF to the variance increases. Consequently, normalizing the PDF to unit variance gives a sharper central part and broader tails at smaller r . The fattening of the PDF with decreasing r can also be viewed as due to the relatively larger contribution of caustics at the tails. The critical value $|w_r^c|$ decreases with decreasing r , suggesting that, for a given St , there are more caustic pairs at smaller r . We also observe that the asymmetry in the two wings decreases with decreasing r . However, it is remains to be verified whether it exactly disappears as $r \rightarrow 0$. At $St \gtrsim 12.4$, the PDF is essentially independent of r , and thus directly applicable for dust particle collisions. For these larger particles, r_p is mainly contributed by the backward separation even for pairs lying around the central part of the PDF, and thus the PDF is independent of r for w_r in any range.

6.2.4. The tangential PDFs: the r -dependence and approaching & separating pairs

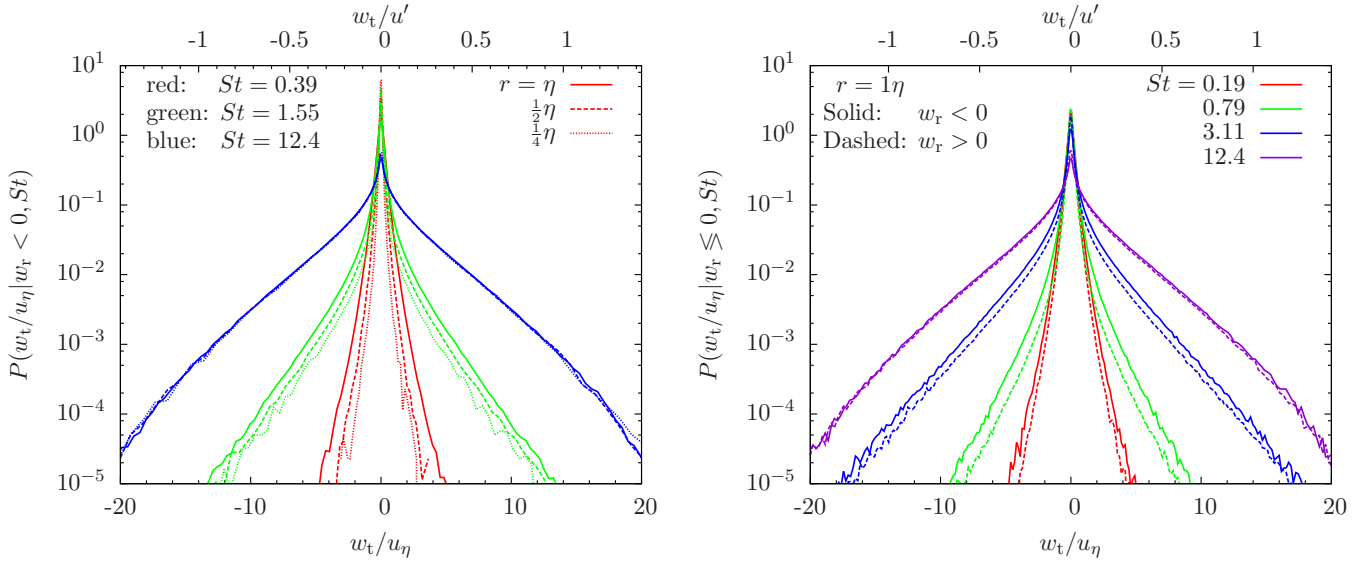


FIG. 13.— Left panel: The PDF of tangential relative speed for approaching pairs at three distances for $St = 0.39, 1.55$ and 12.4 particles. The PDF becomes independent of r at $St \gtrsim 12.4$. Right panel: the tangential PDF for approaching ($w_r < 0$; solid) and separating ($w_r > 0$; dashed) particle pairs at $r = 1\eta$. For $St < 12.4$ particles, the PDF, $P(w_t|w_r < 0, St)$, of approaching pairs is wider than that of separating pairs ($w_r > 0$). Above $St = 12.4$, the two conditional PDFs almost coincide.

The left panel of Fig. 13 shows the PDFs of the tangential relative speed at $r = 1, 0.5$, and 0.25η for three values of St . At smaller r , the number of particle pairs available is smaller, leading to a decrease in the sample size. As a consequence, the PDFs become quite noisy at $r = \eta/4$, especially for small particles. For the r range shown here, the PDF width decreases with decreasing r for $St \lesssim 6.21$ particles. The difference between the PDF tails at $\eta/4$ and $\eta/2$ appears to be smaller than that between $\eta/2$ and η , indicating relatively stronger contribution from caustic formation at smaller r . Like the radial PDF (Fig. 12), the PDF becomes independent of r for $St \gtrsim 12.4$.

In the right panel of Fig. 13, we compare the PDFs of the tangential relative velocity for approaching ($P(w_t|w_r < 0, St)$) and separating ($P(w_t|w_r > 0, St)$) particle pairs at $r = 1\eta$. For $St \lesssim 6.2$, the PDF of approaching particles is broader than the separating ones, consistent with our earlier result for the rms relative speeds, $\langle w_t^2 \rangle_{\mp}^{1/2}$ (see the right panel of Fig. 9). Again, this is because, for a given “initial” value r , the distance of approaching particles was larger in the near past than the separating ones. Therefore, the PDF of the relative velocity for approaching pairs samples the PDF, $P_u(\Delta u, \ell)$, of the flow difference at larger ℓ . Since the width of $P_u(\Delta u, \ell)$ increases with ℓ , $P(w_t|w_r < 0, St)$ is expected to be broader than $P(w_t|w_r > 0, St)$. At $St \gtrsim 12.4$, the PDFs for approaching and separating pairs are almost equal. For these larger particles, the primary distance at $\tau \simeq -\tau_p$ is insensitive to the initial conditions around $\tau = 0$. Although $P(w_t|w_r > 0, St)$ for separating particle pairs is not relevant for particle collisions, a comparison of $P(w_t|w_r < 0, St)$ with $P(w_t|w_r > 0, St)$ provides an interesting illustration for the role of the backward separation of particle pairs in determining their relative velocity.

6.2.5. The normalized PDF of the 3D amplitude

Fig. 14 plots the PDF of the 3D amplitude, $|\mathbf{w}|$, of the relative velocity for approaching particle pairs at $r = 1\eta$.

For each St , the amplitude $|\mathbf{w}|$ is normalized to the rms value $\langle w^2 \rangle_-^{1/2}$, i.e., $|\widetilde{\mathbf{w}}| = |\mathbf{w}|/\langle w^2 \rangle_-^{1/2}$, so that all the normalized PDFs have unit variance. The rms of the 3D amplitude, $\langle w^2 \rangle_-^{1/2}$, for approaching pairs has been shown in Fig. 9. The left and right panels of Fig. 14 show simulation results for small ($St \leq 1.55$) and large ($St \geq 3.11$) particles, respectively. The thin dashed line in the left panel corresponds to approaching tracer particles ($St = 0$), while the dashed line in right panel is the normalized PDF for a Gaussian vector with three independent components of equal variance. The PDF for tracer particles in the left panel is already highly non-Gaussian, as can be seen from a comparison with the dashed line in the right panel. In the left panel, the degree of non-Gaussianity increases as St increases from 0 to $\simeq 1$. At larger St , the PDF peaks at smaller $|\widetilde{\mathbf{w}}|$. The PDF around the rms value (i.e., $|\widetilde{\mathbf{w}}| \simeq 1$) decreases with increasing St , and more probability is distributed toward smaller and larger values of $|\widetilde{\mathbf{w}}|$. This corresponds to the sharpening of $P(w_r, St)$ and $P(w_t|w_r < 0, St)$ in the central part and the broadening of the tail parts in this St range (see Figs. 10, 11 and 12). The trend is reversed as St increases further above $St \simeq 3.11$. The peak of the PDF moves back to around the rms value, $|\widetilde{\mathbf{w}}| \simeq 1$, at $St \gtrsim 49.7$ ($\Omega = 3.5$). The PDF eventually approaches Gaussian in the limit $\tau_p \gg T_L$. However, note that, even for $St = 795$ ($\Omega = 54$) particles, the PDF shows a difference from the Gaussian distribution at small relative speeds.

We find that, for St in the range from 0.78 to 6.22, the PDF shows an extended power-law range at intermediate values of $|\widetilde{\mathbf{w}}|$. For example, at $St = 0.78$, the PDF goes like $|\widetilde{\mathbf{w}}|^{-2.4}$ in the range $0.5 \leq |\widetilde{\mathbf{w}}| \leq 4$. The slope of the PDF in the power-law range becomes shallower with increasing St . For $St = 1.55$, $St = 3.11$ and $St = 6.22$, the power-law exponent of the PDF in the intermediate $|\widetilde{\mathbf{w}}|$ range is -1.8 , -1.3 , and -0.8 , respectively. The

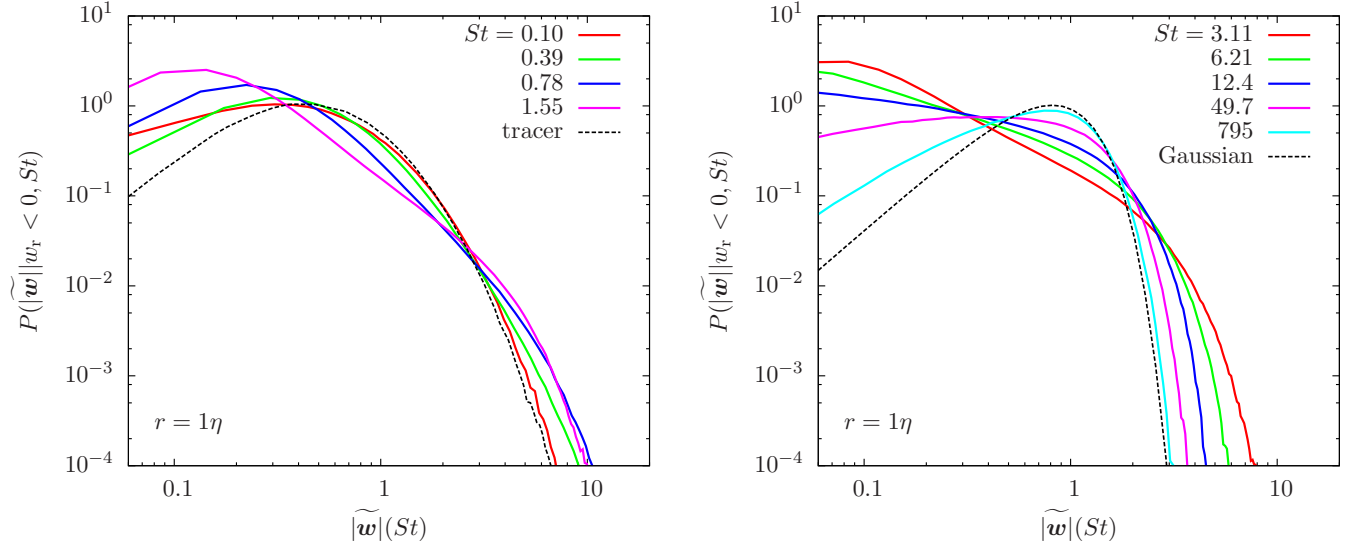


FIG. 14.— The PDF of the 3D amplitude, $|\mathbf{w}|$, of the relative velocity for approaching particle pairs with $w_r < 0$. For each St , the amplitude, $|\mathbf{w}|$, is normalized to its rms value, and the PDF is normalized to have unit variance. In the left panel, the solid lines show results for $St \leq 1.55$, and the dashed line corresponds to the PDF for tracer particles ($St = 0$). The right panel plots PDFs for $St \geq 3.11$. The dashed line in this panel is the normalized PDF, $\sqrt{\frac{54}{\pi}}|\widetilde{\mathbf{w}}|^2 \exp(-3|\widetilde{\mathbf{w}}|^2/2)$, with unit variance for the amplitude of a Gaussian vector.

PDF of $|\mathbf{w}|$ can be easily computed from the PDFs of the radial and tangential components, if the three components are completely independent. In that case, one may obtain fitting functions for $P(|\mathbf{w}|)$ using the fitting functions discussed earlier for the PDFs, $P(w_r, St)$ and $P(w_t | w_r < 0, St)$, of approaching particle pairs. One could also directly fit the PDF of $|\mathbf{w}|$ with simple function forms or tabulate it as a function of St . We will provide fitting functions for $P(|\mathbf{w}|, St)$ in a future paper.

The strong non-Gaussianity in the amplitude of the relative velocity has interesting implications for the growth and evolution of dust particles in planetary disks. We assume that the shape of the collision velocity PDF of dust particles at $r \rightarrow 0$ is more or less similar to the measured PDFs at $r \simeq \eta$ in our simulation, even though the PDFs of $St \lesssim 12.4$ particles have not converged at $r \simeq \eta/4$. The shape of the PDFs shown in Fig. 14 suggests that there would more collisions with extremely large ($|\widetilde{\mathbf{w}}| \gg 1$) or small ($|\widetilde{\mathbf{w}}| \ll 1$) relative speeds than estimated from a Gaussian distribution. The higher probability for collisions with small relative speed would favor sticking, while there are also more collisions that would result in fragmentations. The competition of the two opposite effects would determine whether the non-Gaussian PDF of the collision velocity accelerates or slows down the particle growth. A coagulation model incorporating the non-Gaussian statistics of the collision speed would give a more realistic prediction for the evolution of the size distribution of dust particles.

7. THE COLLISION KERNEL

The prediction of the collision rate is one of the main goals of our study of the particle relative velocity. If the mean number density of inertial particles of a given size is \bar{n}_p , the collision rate per unit volume between these identical particles is estimated by $\frac{1}{2}\bar{n}_p^2\Gamma$, where Γ is the collisional kernel and the factor 1/2 is used to avoid counting the same pair twice. Saffman and Turner (1956) presented two formulations for the collision kernel. The

formulations were based on spherical and cylindrical geometries, respectively, and were thus named as the spherical and cylindrical formulations by Wang et al. (1998).

For the spherical formulation, we make use of the joint distribution, $\rho(r, w_r; St)$, of the particle distance and the radial relative speed, defined at the beginning of §6. The collision kernel for identical particles is written as (e.g., Saffman and Turner 1956),

$$\Gamma^{\text{sph}} = -4\pi d_p^2 \int_{-\infty}^0 \rho(d_p, w_r; St) w_r dw_r \quad (37)$$

where d_p is the diameter of the particle, and the integral limits include only particle pairs moving toward each other. Using the definition of the radial PDF, $P(w_r, St)$ as $\rho(r, w_r; St)/g(r, St)$, eq. (37) can be expressed in a simpler form, $\Gamma^{\text{sph}} = 4\pi d_p^2 g(r, St) F_r^-$, where F_r^- is the inward flux of particles toward a given reference particle defined as $F_r^- = -\int_{-\infty}^0 w_r P(w_r, St) dw_r$.

The particle statistics become stationary when the dynamics is fully relaxed. In the steady state, the inward flux, F_r^- , is equal to the outward flux F_r^+ ($\equiv \int_0^\infty w_r P(w_r, St) dw_r$) (Wang et al. 2000), which is confirmed by our simulation data⁹. This is because the average radial velocity $\langle w_r \rangle = 0$, as expected from statistical isotropy, and $\langle w_r \rangle = F_r^+ - F_r^-$ by definition. We thus have $F_r^+ = F_r^- = \frac{1}{2}\langle |w_r| \rangle$ where $\langle |w_r| \rangle$ is the ensemble average of the absolute value of the radial relative velocity.

⁹ Similar to the variances, $\langle w_r^2 \rangle_{\mp}$, of approaching and separating pairs, one can also define $\langle w_r \rangle_- = F_r^- / \int_{-\infty}^0 P(w_r, St) dw_r$ and $\langle w_r \rangle_+ = F_r^+ / \int_0^\infty P(w_r, St) dw_r$. Using the same reasoning in §6.1.3, we expect $\langle w_r \rangle_- > \langle w_r \rangle_+$ for inertial particles, which is confirmed by the simulation data. Together with the steady-state condition $F_r^- = F_r^+$, we have $\int_{-\infty}^0 P(w_r, St) dw_r < \int_0^\infty P(w_r, St) dw_r$. This means that there tend to be more particles coming out from a reference particle, suggesting a larger particle density at small distances to the reference particle. This provides an interesting physical perspective for the origin of particle clustering.

ity. The collision kernel can then be written as (Wang et al. 2000),

$$\Gamma^{\text{sph}} = 2\pi d_p^2 g(d_p, St) \langle |w_r| \rangle. \quad (38)$$

The cylindrical formulation assumes that all particles inside a cylinder of length $\langle |w| \rangle dt$ located at a distance d_p from a given particle will collide with the particle in a time interval dt . Similar to eq. (38), the cylindrical collision kernel can be written as $\Gamma^{\text{cyl}} = \pi d_p^2 g \langle |w| \rangle$, with $\langle |w| \rangle$ being the average of the 3D amplitude of the relative velocity.

To evaluate the collision kernel, one can start directly from eq. (37) using the joint distribution, $\rho(r, w_r; St)$. However, previous studies have shown that considering the RDF and $\langle |w_r| \rangle$ separately provides interesting insights on the estimate of the particle collision rate (e.g., Sundaram & Collins 1997, Wang et al. 2000). In §7.1, we compute the RDF and the absolute average of the relative speed from our simulation data.

7.1. The Overall RDF and Absolute Average of the Relative Speed

The RDF represents the probability of finding a neighboring particle at a distance of r with any relative velocity, and is a measure for the spatial clustering of the particles. Due to their finite inertia, inertial particles do not exactly follow the flow velocity and have been found to exhibit inhomogeneous distribution even in incompressible turbulence. Turbulent clustering of inertial particles has been extensively investigated in the literature (see e.g., Maxey 1987, Sundaram and Collins 1997, Wang et al. 2000, Cuzzi et al. 2001, Hogan & Cuzzi 2001, Balkovsky et al. 2001, Zaichik et al. 2003, Falkovich and Pumir 2004, Cuzzi et al. 2008, Pan et al. 2011). The general physical interpretation for turbulent clustering is that vortical structures in turbulent flows tend to expel inertial particles. The particles are pushed out of high-vorticity regions by the centrifugal force, leading to the formation of clusters in strain-dominated regions.

Fig. 15 plots the RDF as a function of St at $r = 1, 0.5$ and 0.25η . Consistent with previous studies, the RDF is largest for $St \simeq 1$ particles, whose friction timescale couples with the smallest scale of the turbulent flow. For r in the dissipation range, the RDF increases toward smaller r as a power-law, i.e., $g(St, r) \propto r^{-\mu}$. The scaling exponent μ peaks at $St \simeq 1$, and approaches zero in the limits $St \ll 1$ and $St \gg 1$. We measured μ using the values of r shown in Fig. 15, and found that $\mu = 0.73$ for $St = 0.78$, consistent with the result of Pan et al. (2011). The interested reader is referred to Pan et al. (2011) for the scaling exponent, μ , as a function of St .

In the left panel of Fig. (16), we plot the simulation result for $\langle |w_r| \rangle$ at $r = 1, 0.5$, and 0.25η . For comparison, we also show the data (circles) for the rms of the radial relative speed at $r = 1\eta$. Qualitatively, $\langle |w_r| \rangle$ as a function of St and r is similar to the rms. It is smaller than the rms, as it corresponds to the 1st-order moment of the PDF, $P(w_r, St)$, of w_r . Most theoretical models, including our own, for the particle relative velocity are based on the computation of the variance (e.g., $\langle w_r^2 \rangle$), and cannot be directly applied to predict $\langle |w_r| \rangle$. The conversion between $\langle w_r^2 \rangle$ and $\langle |w_r| \rangle$ relies on the shape of the PDF of w_r , which is difficult to predict. We thus

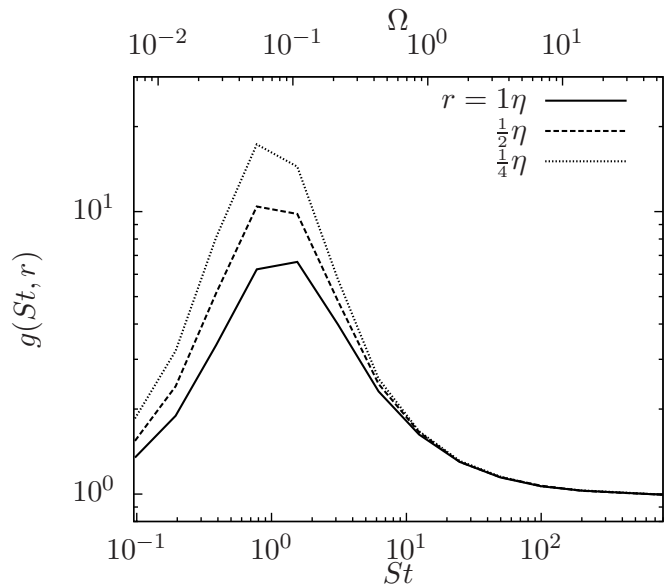


FIG. 15.— The radial distribution function, $g(St, r)$, as a function of the Stokes number at $r = 1$ (solid), 0.5 (dashed) and 0.25η (dotted).

did not attempt to fit $\langle |w_r| \rangle$ with a model prediction.

Similar to the S-T formula (eq. 11) for the variances of the relative velocity, we would predict that $\langle |w_r| \rangle = \langle |\Delta u_r| \rangle$ in the $St \ll 1$ limit, where $\langle |\Delta u_r| \rangle$ is the absolute average of the longitudinal flow velocity increment. At $\ell \lesssim \eta$, $\langle |\Delta u_r| \rangle$ is expected to scale linearly with ℓ . We find that, for $St \ll 1$, $\langle |w_r| \rangle \propto r^{0.9}$, which is slightly shallower than the linear scaling. This is likely caused by the contribution from the effect of slings or caustics. The scaling is steeper than $r^{0.78}$ for the radial rms velocity (see §6.1.2), suggesting that $\langle |w_r| \rangle$ follows the flow velocity scaling better. The behavior of $\langle |\Delta u_r| \rangle$ at small St also appears to be more regular than that of $\langle w_r^2 \rangle^{1/2}$. For all three values of r , the $\langle |w_r| \rangle$ curves become flat at $St \lesssim 0.4$. The likely reason is that $\langle |w_r| \rangle$ represents statistics at a lower order than the variance (or rms), and is thus less affected by the rare and extreme sling events, or by the numerical uncertainty in the particle trajectory computation.

The inset of the left panel shows the ratio of the absolute average to the rms. The ratio depends on the PDF shape of w_r , and particularly on the central part of the PDF because both $\langle |w_r| \rangle$ and the rms are lower-order moments. As a reference, if the PDF $P(w_r, St)$ is Gaussian, we have $\langle |w_r| \rangle / \langle w_r^2 \rangle^{1/2} = (2/\pi)^{1/2} = 0.80$ (e.g., Wang et al. 2000), and for an exponential PDF it is equal to $1/\sqrt{2}$. The ratio from a Gaussian PDF was usually used to convert the model predictions for the rms to $\langle |w_r| \rangle$ (Wang et al. 2000, Zaichik et al. 2003, 2006). Generally, the ratio is smaller if the central PDF is sharper and the tails are fatter. As seen in the inset, the ratio reaches a minimum at $St \simeq 1$, corresponding to a maximum fatness of the PDF at $St \simeq 1$ (see §6.2.3). At $r \leq \eta$, the minimum is smaller than 0.45, corresponding to highly non-Gaussian PDF. At $St \simeq 800$, $\langle |w_r| \rangle / \langle w_r^2 \rangle^{1/2}$ reaches 0.78, close to the expected value for a Gaussian PDF. For the range of r shown here, the ratio also decreases with decreasing r for $St \lesssim 6$, which is expected from the trend of the PDF

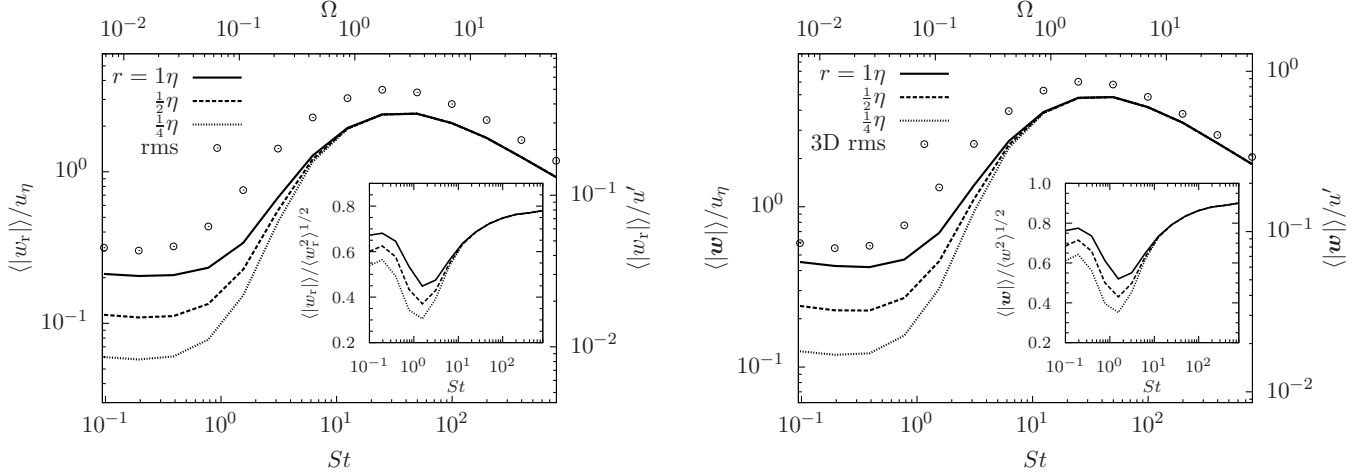


FIG. 16.— Left panel: The average of the absolute value of the radial relative speed, $\langle |w_r| \rangle$, as a function of the Stokes number. Solid, dashed and dotted lines correspond to the particle distance $r = 1, 0.5$ and 0.25η , respectively. For comparison, the circles show the rms, $\langle w_r^2 \rangle^{1/2}$, of the radial relative speed at $r = 1\eta$. The inset plots the ratio, $\langle |w_r| \rangle / \langle w_r^2 \rangle^{1/2}$, at $r = 1$ (solid), 0.5 (dashed) and 0.25η (dotted). Right panel: same as the left panel, but for the 3D amplitude, $|\mathbf{w}|$, and the 3D rms, $\langle w^2 \rangle^{1/2}$, of the relative velocity.

shape with r for these particles (§6.2.3).

Our simulation result for $\langle |\mathbf{w}| \rangle$ is shown in the right panel of Fig. (16), which is very similar to the left panel for $\langle |w_r| \rangle$. At $St \lesssim 0.4$, we find $\langle |\mathbf{w}| \rangle$ also scales as $r^{0.9}$ with r . The ratio of $\langle |\mathbf{w}| \rangle$ to $\langle w^2 \rangle^{1/2}$ also shows a dip at $St \simeq 1$. The ratio approaches 0.9 at the largest St , as expected from a 3D Gaussian distribution.

In Fig. 17, we plot Γ^{sph} and Γ^{cyl} normalized to $\pi d_p^2 u_\eta$. The normalized kernels correspond to the product $2g(St, r)\langle |w_r| \rangle / u_\eta$ (solid lines) for the spherical formulation and $g(St, r)\langle |\mathbf{w}| \rangle / u_\eta$ (dashed lines) for the cylindrical formulation. We will also refer to these products as the collision kernel per unit cross section. At each r , the solid and dashed lines almost coincide, meaning that Γ^{sph} and Γ^{cyl} are nearly equal at all St and r . This suggests that $\langle |w_r| \rangle \simeq 0.5\langle |\mathbf{w}| \rangle$ since $\Gamma^{\text{sph}}/\Gamma^{\text{cyl}} =$

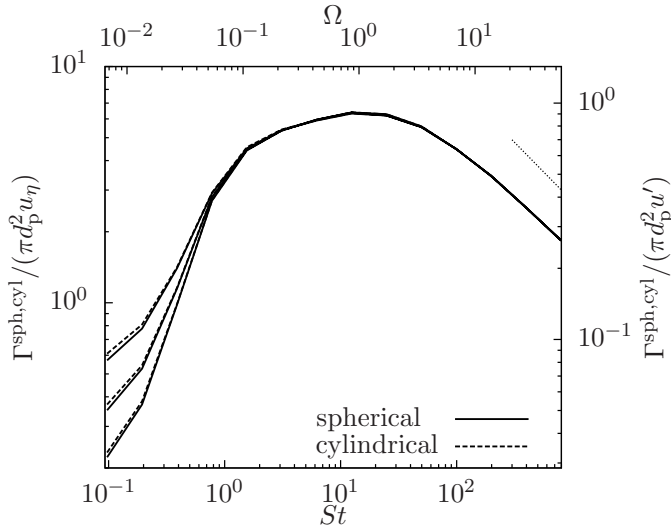


FIG. 17.— The collision kernels normalized to $\pi d_p^2 u_\eta$. The solid lines plot $2g(St, r)\langle |w_r| \rangle / u_\eta$ for the spherical formulation, and the dashed lines show $g(St, r)\langle |\mathbf{w}| \rangle / u_\eta$ for the cylindrical formulation. The lines from bottom to top correspond to normalized kernels measured at $r = 0.25, 0.5$ and 1η , respectively. The dotted line segment corresponds to a $St^{-1/2}$ scaling.

$2\langle |w_r| \rangle / \langle |\mathbf{w}| \rangle$. The two collision kernels have a noticeable difference only at $St = 0.1 - 0.2$, where Γ^{sph} is smaller than Γ^{cyl} by $\lesssim 5\%$. This is consistent with the result of Wang et al. (2000). Wang et al. (2000) also showed that the spherical formulation provides an almost exact description for the particle collision rate. The near equality of Γ^{sph} and Γ^{cyl} at all St and r suggests that one can apply either formulation to evaluate the collision rate.

Fig. 17 shows that $2g(St, r)\langle |w_r| \rangle$ and $g(St, r)\langle |\mathbf{w}| \rangle$ are independent of r for $St \geq 1$. Apparently, this is because, at $St \gtrsim 1$, the r -dependences of the RDF $g(St, r)$ and the absolute average $\langle |w_r| \rangle$ (or $\langle |\mathbf{w}| \rangle$) almost cancel out (see Figs. 15 and 16). A more interesting perspective is that the inverse scaling of $g(St, r)$ and $\langle |w_r| \rangle$ is expected from the intuition that the normalized kernel approaches a finite constant, corresponding to a finite collision rate, at sufficiently small r . Therefore, the scalings of $g(St, r)$ and $\langle |w_r| \rangle$ must cancel out once the kernel converges (see more discussions in §7.2). At $St = 1.55$, $g(St, r)$ increases with decreasing r as $\propto r^{-0.55}$, while both $\langle |w_r| \rangle$ and $\langle |\mathbf{w}| \rangle$ scale with r as $\propto r^{0.57}$. Note that, if the $r^{0.57}$ scaling of the relative speed persists in the $r \rightarrow 0$ limit, it does mean the collision energy is zero for nearly-point particles. This is because $\langle |w_r| \rangle$ or $\langle |\mathbf{w}| \rangle$ does not represent the collision energy. The average collision energy per collision is expected to be finite even if $\langle |w_r| \rangle$ or $\langle |\mathbf{w}| \rangle$ approaches zero at $r \rightarrow 0$ (see §7.2). The cancellation between the overall $g(St, r)$ and $\langle |w_r| \rangle$ for $St \gtrsim 1$ particles needs to be interpreted with care. As discussed in §6.2, at a given r , there are two types of particle pairs, i.e., continuous and caustic pairs. The two types have different properties, and the inverse scalings of the overall RDF and relative velocity could be an artifact of not properly splitting the two types of particle pairs¹⁰. In §7.2, we will evaluate the contribution from each type of pairs.

We find that the collision kernel per unit cross section

¹⁰ For example, if for $St \gtrsim 1$ particles one type of pairs dominates the contribution to the RDF, while the other provides a dominant and r -independent contribution to the collision kernel, then the cancellation of the scaling exponents of the overall RDF and relative velocity would not be meaningful physically.

shows an abrupt increase as St increases toward 1 (see, e.g., Sundaram & Collins 1997), increases only slightly for St between 1 and $St_m \simeq 30$, and starts to decrease at $St \simeq 30$. It finally scales with St as $St^{-1/2}$ at $\tau_p \gg T_L$. A physical discussion for the behaviors is given in §7.2.

The r -independence of the kernel of $St \geq 1$ particles at $r \simeq \eta$ implies that one may apply our result to estimate the collision kernel of $St \gtrsim 1$ dust particles in protoplanetary turbulence, even though the dust particle diameter d_p is smaller than η by orders of magnitude. On the other hand, at $St \lesssim 1$, the measured collision kernel depends on r in the range of r considered, and is thus not directly applicable for dust particles with $St \lesssim 1$. To achieve a general understanding of the $r \rightarrow 0$ limit, it would be useful if one could isolate an r -independent contribution. For this purpose, we make a preliminary attempt to separate the contributions from the continuous and caustic pairs.

7.2. Decomposing the Continuous and Caustic Contributions

As discussed in §6.2, at a given distance, r , there are two types of particle pairs, corresponding to the continuous (inner) and caustic (tail) parts of the relative velocity PDF. For the radial relative speed PDF of approaching particle pairs, the two parts can be roughly divided by a critical value, $w_r^c \simeq -r/\tau_p$. In this section, we separate the contributions of the two types of pairs to the collision kernel in the spherical formulation. Using the relation $\rho(r, w_r; St) = g(r, St)P(w_r, St)$, and splitting the left wing of $P(w_r, St)$ into two parts, the collision kernel, eq. (37), is written as,

$$\Gamma^{\text{sph}} = \Gamma^{\text{con}} + \Gamma^{\text{cau}}, \quad (39)$$

where $\Gamma^{\text{con}} = -4\pi d_p^2 g(r, St) \int_{w_r^c}^0 w_r P(w_r, St) dw_r$ and $\Gamma^{\text{cau}} = -4\pi d_p^2 g(r, St) \int_{-\infty}^{w_r^c} w_r P(w_r, St) dw_r$. The continuous and caustic contributions can be expressed in more convenient forms,

$$\begin{aligned} \Gamma^{\text{con}} &= 4\pi d_p^2 g^{\text{con}} \langle w_r^{\text{con}} \rangle \\ \Gamma^{\text{cau}} &= 4\pi d_p^2 g^{\text{cau}} \langle w_r^{\text{cau}} \rangle \end{aligned} \quad (40)$$

where $g^{\text{con}}(r, St) \equiv g(r, St) \int_{w_r^c}^0 P(w_r, St) dw_r$ and $g^{\text{cau}}(r, St) \equiv g(r, St) \int_{-\infty}^{w_r^c} P(w_r, St) dw_r$ are the RDFs of continuous and caustic pairs, corresponding to the probabilities of finding an approaching neighbor that makes a continuous and caustic pair, respectively. The sum of g^{con} and g^{cau} is given by $g^- \equiv g(r, St) \int_{-\infty}^0 P(w_r, St) dw_r$. Because there are more separating pairs than approaching ones, g^- is smaller (by 10-20%) than $0.5g(r, St)$ at $St \lesssim 10$. It becomes equal to $0.5g$ at $St \gtrsim 10$. The average radial relative speeds for the two types of pairs are defined as $\langle w_r^{\text{con}} \rangle = -\int_{w_r^c}^0 w_r P(w_r, St) dw_r / \int_{w_r^c}^0 P(w_r, St) dw_r$, and $\langle w_r^{\text{cau}} \rangle = -\int_{-\infty}^{w_r^c} w_r P(w_r, St) dw_r / \int_{-\infty}^{w_r^c} P(w_r, St) dw_r$. The four quantities, g^{con} , g^{cau} , $\langle w_r^{\text{con}} \rangle$, and $\langle w_r^{\text{cau}} \rangle$, depend on w_r^c , whose exact value is uncertain. We will set $w_r^c = -r/\tau_p$ here, and defer a study on the effect of the choice of w_r^c to a later work.

In the formulation of Falkovich et al. (2002) for the collision kernel of $St \lesssim 1$ particles, the clustering effect enters only for the S-T (continuous) contribution. The RDF was theoretically modeled and evaluated by considering the continuous-type particles only. For the continuous pairs, $\langle w_r^{\text{con}} \rangle$ scales linearly with r , as in the S-T prediction. The continuous contribution to the kernel is amplified by the clustering effect. On the other hand, the Falkovich et al. formulation suggests that clustering plays no role for the sling (caustic) contribution. Both $\langle w_r^{\text{cau}} \rangle$, and the normalized kernel $\Gamma^{\text{cau}}/(\pi d_p^2)$ due to the slings are independent of the particle distance (Falkovich et al. 2002). These also imply that g^{cau} is r -independent. The model of Gustavsson & Mehlig (2011) provides a similar formulation for the collision kernel. The continuous contribution is essentially the same as that in Falkovich et al. (2002). They also predicted an r -independent caustic contribution to the normalized kernel. However, unlike Falkovich et al. (2002), their derivation accounts for the possibility that both g^{cau} and $\langle w_r^{\text{cau}} \rangle$ may depend on r . But their scaling exponents exactly cancel out, giving an r -independent contribution to the kernel.

In the left panel of Fig. 18, we plot g^{con} (blue) and g^{cau} (red) computed from our simulation data at three distances. At $St \lesssim 1$, the number of caustic pairs is small, and most particle pairs belong to the continuous type. The continuous-type particles show significant clustering at $St \lesssim 3$, and the RDF g^{con} increases toward smaller r with similar scaling exponents as the overall RDF. These suggest that the origin of strong clustering at $St \lesssim 3$ corresponds to the continuous-type particles (Falkovich et al. 2002). Similar to the overall RDF (Fig. 15), g^{con} peaks at $St \simeq 1$. At larger St , g^{con} decreases rapidly with St , and becomes comparable to g^{cau} at $St \simeq 3$. The fast drop of g^{con} at $St \gtrsim 3$ is because it becomes sensitive to the critical value, w_r^c , as the range $(w_r^c, 0)$ narrows with increasing St . This range also becomes narrower with decreasing r , and this causes g^{con} to slightly decrease with decreasing r at $St \gtrsim 3$. At $St \simeq 6.2$, g^{con} is significantly smaller than g^{cau} , and essentially all particle pairs are of the caustic type. The caustic RDF g^{cau} increases with decreasing r for particles with $St \lesssim 10$, and is r -independent at larger St .

Concerning the r -dependence of g^{cau} at $St \lesssim 10$, there are several possibilities. The first is that this dependence is generic, and $g^{\text{cau}} \rightarrow \infty$ as $r \rightarrow 0$, as considered by Gustavsson & Mehlig (2011). Second, the r -dependence of g^{cau} may disappear at sufficiently small r , and g^{cau} finally converges to a finite constant, as assumed in Falkovich et al. (2002). In this case, one may in principle achieve a converged g^{cau} by using a larger number of $St \lesssim 10$ particles in the simulation to resolve smaller scales. We checked $r = \eta/8$ in our simulation and found that the convergence is not reached yet. Third, the r -dependence of g^{cau} may be an artifact of our selected value for w_r^c . We attempted to vary w_r^c around $-r/\tau_p$ by a factor 4, but were not able to find a considerable decrease in the r -dependence of g^{cau} . It is also possible that the transition from the continuous to the caustic type is gradual, and thus exactly splitting two types by a single critical value (w_r^c) is impossible at least at the scales explored here. We note that g^{cau} is larger than 0.5 at $St \simeq 3.11$, suggesting some degree of clustering for caustic-type par-

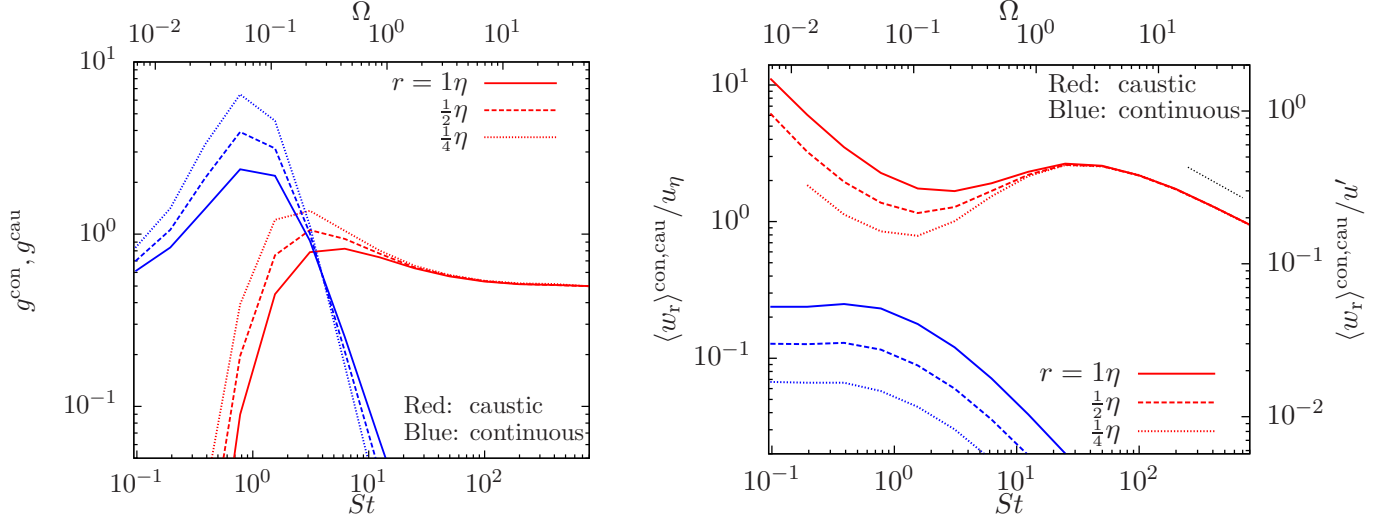


FIG. 18.— Left panel: RDFs for continuous (blue) and caustic (red) particle pairs at $r = 1\eta$ (solid), 0.5η (dashed) and 0.25η (dotted), respectively. Right panel: Average velocities, $\langle w_r^{\text{con}} \rangle$ and $\langle w_r^{\text{cau}} \rangle$, of continuous and caustic pairs at the same three distances. The dotted line segment denotes a $St^{1/2}$ scaling. In both panels, the critical value, w_r^c , is set to $-r/\tau_p$. The red dotted-curve in the right panel lacks a point at $St = 0.1$ because no caustic pairs were found for $St = 0.1$ particles at $r = \eta/4$ in the simulation. For the corresponding curve in the left panel, g^{cau} drops to zero at $St = 0.1$, which is not visible due to the selected Y-range in the figure.

ticles. This, however, could be an artifact that the two types of pairs are not split precisely.

The right panel of Fig. 18 shows the average relative speeds, $\langle w_r^{\text{con}} \rangle$ and $\langle w_r^{\text{cau}} \rangle$, for continuous (blue) and caustic (red) pairs. At $St \ll 1$, $\langle w_r^{\text{con}} \rangle$ is constant with St and decreases linearly with r , as in the S-T prediction. At $St \gtrsim 1$, $\langle w_r^{\text{con}} \rangle$ decreases with St . This is because the number of continuous pairs becomes small and the average relative speed starts to have a sensitive dependence on the lower limit w_r^c , which becomes closer to zero as St increases. By definition, the caustic pairs have larger relative velocity than continuous pairs. At $St \ll 1$, the sling events or caustic formation occur only in regions with very large velocity gradient, and this is responsible for the large relative velocity for caustic pairs at small St . As St increases, the criterion for the sling events to occur becomes weaker, as reflected by the decrease of $|w_r^c|$. This results in a decrease in $\langle w_r^{\text{cau}} \rangle$ toward $St \simeq 1$. At $St \gtrsim 3$, most particles belong to the caustic type, and thus the trend of $\langle w_r^{\text{cau}} \rangle$ as a function St becomes similar to the overall relative speed $\langle |w_r| \rangle$ (see Fig. 16). It first increases with St for $3 \lesssim St \lesssim St_m \simeq 30$, and then decreases at $St \gtrsim St_m$. At the three distances shown here, $\langle w_r^{\text{cau}} \rangle$ decreases with decreasing r for $St \lesssim 10$ particles, as the condition to have a caustic pair is weaker at smaller r . Again, the r -dependence of $\langle w_r^{\text{cau}} \rangle$ may disappear at much smaller r and/or with a better method to split the two types of pairs. At $St \gtrsim 10$, both g^{cau} and $\langle w_r^{\text{cau}} \rangle$ are independent of r , indicating full resolution of their statistics in our simulation.

In Fig. 19, we show the continuous (blue) and caustic (red) contributions to the collision kernel per unit cross section. In the r range shown here, the continuous and caustic contributions dominate for $St \lesssim 1$ and $St \gtrsim 1$, respectively. The continuous contribution decreases with r , corresponding to the r -dependence of the overall kernel, Γ^{sph} , in Fig. 17. The decrease of the continuous contribution with r is expected from the scaling exponents of g^{con} and $\langle w^{\text{con}} \rangle$. With decreasing r , $\langle w^{\text{con}} \rangle$ decreases linearly, which is faster than the increase of g^{con} . In

the limit $r \rightarrow 0$, the continuous contribution is expected to vanish for all particles. This means that, although amplified by clustering, the continuous-type particles do not significantly contribute to the collision rate of dust particles, as pointed out by Hubbard (2012).

The contribution of the caustic-type particles to the normalized kernel is found to be approximately r -independent. The differences in three red lines are small, and one may claim achieving numerical convergence at $r = \eta/4$ for all particles. The r -independence of $\Gamma^{\text{cau}}/(\pi r_p^2)$ for $St \lesssim 10$ particles at the distances explored here is related to the cancellation of the scalings of g^{cau} and $\langle w_r^{\text{cau}} \rangle$. Intuitively, one would expect that the collision rate of inertial particles converges to a finite constant in the $r \rightarrow 0$ limit. Therefore, g^{cau} and $\langle w_r^{\text{cau}} \rangle$ must have inverse scalings with r , once the caustic kernel converges. On the other hand, one may prove the intuition of a finite constant caustic kernel at sufficiently small r by showing that g^{cau} and $\langle w_r^{\text{cau}} \rangle$ scale inversely with r , which was actually predicted by the theoretical model of Gustavsson & Mehlig (2011). As discussed earlier, both g^{cau} and $\langle w_r^{\text{cau}} \rangle$ may become independent of r at much smaller r . However, it is also possible that, as $r \rightarrow 0$, $g^{\text{cau}} \rightarrow \infty$ and $\langle w_r^{\text{cau}} \rangle \rightarrow 0$, especially for $St \lesssim 1$ particles. Note that $\langle w_r^{\text{cau}} \rangle$ does not represent the collisional energy at all. Even if $\langle w_r^{\text{cau}} \rangle \rightarrow 0$, it does not suggest the average collisional energy is zero. In fact, a computation of the average collision energy per collision (i.e., the relative velocity variance weighted by the collision rate; see, e.g., Hubbard 2012) by caustic pairs for particles with $1 \lesssim St \lesssim 10$ in our simulation shows that it already converges to a finite constant at $r = \eta/4$. The collision energy (velocity) of $St \lesssim 10$ particles by caustic pairs in the $r \rightarrow 0$ limit will be examined systematically in a future study.

The r -independence of the caustic contribution is responsible for that of the overall normalized kernel at $St \gtrsim 1$ observed in Fig. 17. Because the continuous contribution vanishes as $r \rightarrow 0$, and due to the convergence

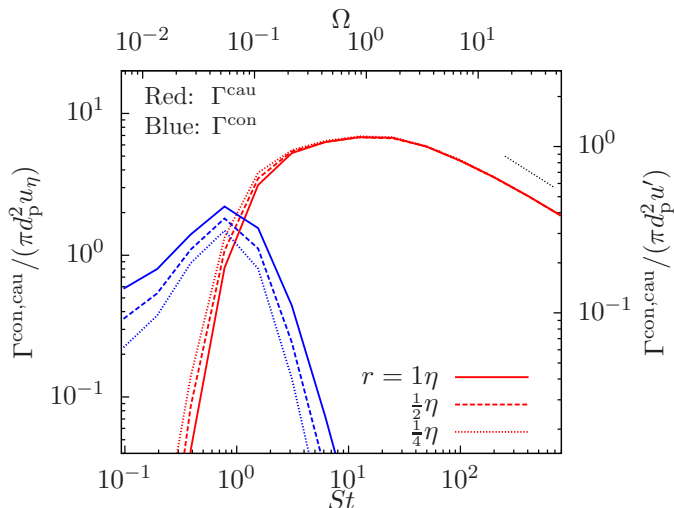


FIG. 19.— The continuous (Γ^{con} ; blue) and caustic (Γ^{cau} ; red) contributions to the kernel normalized to $\pi d_p^2 u_\eta$ or $\pi d_p^2 u'$ on the left and right Y-axis, respectively. The solid, dashed and dotted lines correspond to normalized kernels measured at $r = 1, 0.5$ and 0.25η , respectively. The dotted line segment shows a $St^{-1/2}$ scaling.

of the caustic contribution, one may use our result for Γ^{cau} to estimate the collision rate of nearly point-like dust particles. One caveat, however, is that Γ^{cau} has a dependence on the critical value, w_r^c , for $St \lesssim 1$ particles, an issue that will be refined in a future work.

From the behaviors of Γ^{con} and Γ^{cau} with r , there exists a distance, r_c , below which the caustic contribution dominates. The critical distance r_c is generally a function of St . As seen in Fig. 19, $r_c \gtrsim 1\eta$ for $St \gtrsim 1$. At $St = 0.78$, the two contributions become about equal at $r_c \simeq \eta/4$. Below $St = 0.78$, r_c decreases very rapidly. For example, $r_c \lesssim 0.01\eta$ for $St = 0.39$. Achieving sufficient statistics at such a small distance is computationally challenging, as it requires a huge number of particles. Directly resolving Γ^{sph} for nearly point particles with $St \lesssim 0.8$ would be extremely difficult, and the best approach is thus to properly isolate the caustic and continuous contributions.

The normalized caustic kernel experiences a sharp rise as St increase from 0.1 to 1, suggesting that the collision frequency greatly accelerates as the particle size grows toward $St \simeq 1$. The rise corresponds to the fast increase of g^{cau} (see the left panel of Fig. 18), which has been interpreted as due to the rapid caustic formation (Wilkinson et al. 2006). It has been claimed that the effect of caustic formation may be modeled as an activation process. If we fit the normalized caustic kernel by $\exp(-A/St)$ (Wilkinson et al. 2006, Falkovich & Pumis 2007), the activation value, A , is found to be around 1.7. The sling events or caustic formation occur at places where the flow velocity gradient is larger than τ_p^{-1} (Falkovich et al. 2002). At these locations, the flow velocity changes faster than the response of the particle. For small particles with $\tau_p \ll \tau_\eta$, the probability of the sling events corresponds to the high PDF tail of the flow velocity gradient. With increasing τ_p , the probability becomes larger as it samples toward the inner parts of the flow velocity gradient PDF. Since the rms flow gradient is on the order of τ_η^{-1} , the probability would increase rapidly as τ_p^{-1} approaches τ_η^{-1} , leading to a sharp rise in the sling frequency and

the caustic kernel at $St \simeq 1$.

For St between 1 and the peak Stokes number, $St_m \simeq 30$, the normalized caustic kernel is almost constant, increasing only by 50%. This is apparently due to the opposite trends of g^{cau} and $\langle w_r^{\text{cau}} \rangle$ with St in this range. The kernel starts to decrease at $St \simeq 30$ due to the decrease of $\langle w_r^{\text{cau}} \rangle$. It finally scales with St as $St^{-1/2}$ (dotted line segment in Fig. 19) for particles with $\tau_p \gg T_L$.

We finally comment on the collision kernel commonly used in coagulation models for the dust particle growth in protoplanetary disks. In these models, the kernel is typically set to $\Gamma^{\text{coa}} = \pi d_p^2 \langle w^2 \rangle^{1/2}$ (e.g., Dullemond and Dominik 2005). The models usually adopt the rms collision velocities based on the model of Volk et al. (1980) or its later developments. Γ^{coa} is of the cylindrical type discussed in §7.1. However, it would be more appropriate to use $\langle |\mathbf{w}| \rangle$, rather than the 3D rms, $\langle w^2 \rangle^{1/2}$, in the cylindrical formulation (Wang et al. 2000; see the inset in the right panel of Fig. 16 for the difference between $\langle |\mathbf{w}| \rangle$ and $\langle w^2 \rangle^{1/2}$). We argue that Γ^{coa} cannot sufficiently capture the wealth of physics for the turbulence-induced collision rate, especially the interesting phenomena that occur at small St . The prediction of Volk et al. for $\langle w^2 \rangle^{1/2}$ should be viewed as for the $r \rightarrow 0$ limit, as it does not consider the r -dependence of the relative speed. Thus, we compare Γ^{coa} with our simulation result for Γ^{cau} , which provides the dominant contribution in the $r \rightarrow 0$ limit. We point out several problems in the qualitative behavior of the commonly-used collision kernel.

First, Volk et al.'s model predicts that $\langle w^2 \rangle^{1/2}$ drops exactly to zero for small particles with τ_p below the turnover time of the smallest eddies in the assumed flow energy spectrum (e.g., Cuzzi & Hoggan 2003). However, our simulation result shows that, for any finite $St \lesssim 1$, Γ^{cau} is nonzero, and it can be estimated from the activation formula, $\propto \exp(-A/St)$. Clearly, the Volk et al. model does not capture the sling effect, and cannot accurately estimate the kernel at $St \lesssim 1$. Second, based on Fig. 5 of Cuzzi & Hoggan (2003), Γ^{coa} would increase quite rapidly as St increases from 1 to 2-3, and then connect to a $St^{1/2}$ scaling at $St \gtrsim 3$. This is in contrast to Γ^{cau} found in our simulation, which changes quite slowly in the range $1 \lesssim St \lesssim 10$. This suggests that the commonly-used Γ^{coa} is inaccurate for $St \lesssim 10$. This range of St may include particle sizes up to chondrules for typical disk parameters at a radius of 1 AU. It remains to be checked by simulations at higher resolutions whether and how Γ^{coa} switches to a $St^{1/2}$ scaling for inertial-range particles. Finally, the Volk et al. model overestimates the peak relative speed at St_m (§6.1.1), and would thus overestimate the collision rate by a factor of 2 or so for inertial-range particles and/or large particles with $St > St_m$.

8. CONCLUSIONS

We investigated the turbulence-induced relative velocity of inertial particles using both theoretical modeling and numerical simulations. We conducted a 512^3 simulation of a weakly compressible turbulent flow with an rms Mach number of $\simeq 0.1$, and evolved 14 species of inertial particles with friction timescales, τ_p , covering the entire scale range of the flow. The Stokes number, St , of the particles spans about 4 order of magnitudes, ranging

from 0.1 to 800. The friction time of the largest particles is about 41 times the large eddy turnover time, or 54 times the Lagrangian correlation time. We used the simulation to test the theoretical model for the rms relative velocity of inertial particles by Pan & Padoan (2010), in the case of identical particles (equal friction times). We explored the probability distribution function (PDF) of the relative velocity. Consistent with previous studies, our simulation result for the PDF indicates two different types of particle pairs, named as the continuous and caustic pairs, respectively. In this work, the relative velocity statistics is measured at distances, r , in the range from $\eta/4$ to η . An accurate measurement at smaller scales would require a larger simulation with a larger number of particles. Our study for the relative velocity helps reveal the fundamental physics, and provides a theoretical preparation toward modeling the collision velocity of nearly-point dust particles at $r \rightarrow 0$. Using the simulation data, we computed the particle collision kernel, and, in particular, we evaluated the contributions from the continuous and caustic pairs. Distinguishing the two types of contributions is crucial for the estimate of the kernel at $r \rightarrow 0$. We summarize the main results of this work.

1. We introduced the formulation for the particle relative velocity by Pan & Padoan (2010), which reveals an insightful physical picture. The relative velocity of two nearby identical particles is determined by the memory of the flow velocity difference along their trajectories in the past, and hence depends on the separation behavior of particle pairs backward in time. We adopted a two-phase separation behavior consisting of a ballistic and a Richardson phase, and showed that the model predicts a $St^{1/2}$ scaling for inertial-range particles in turbulent flows with an extended inertial range. The model can correctly reproduce the expected behaviors in the extreme limits of small and large particles. The model prediction for the rms relative velocity is in good agreement with the simulation results for $\eta/4 \lesssim r \lesssim \eta$. The physical picture also provides a successful explanation for the relative velocity PDF as a function of St .
2. To improve the understanding of the inertial particle statistics, we analyzed both Lagrangian and Eulerian temporal correlation functions in the simulated flow. While the flow velocity along the trajectory of a small particle is close to Lagrangian, the velocity seen by a very large particle may be better approximated by Eulerian. The Eulerian and Lagrangian correlation timescales, T_E and T_L , were found to be close to each other, with T_E slightly larger (by 10%). Our model predictions for both 1-particle rms velocity and the rms relative speed between two identical particles depend mainly on the correlation timescale and are insensitive to the function form of the temporal correlation. These provides a validation for using the Lagrangian correlation function form for all particles.
3. Our simulation data shows that, in the small particle limit ($St \ll 1$), the 3D rms relative velocity

of particle pairs at a distance $r = \eta$ is constant, $\simeq u_\eta/\sqrt{3}$, consistent with the Saffman-Turner prediction. It starts to rise at $St \gtrsim 1$, and peaks for particles with $\tau_p \simeq 2T_L$, corresponding to $St = St_m \simeq 30$ in our simulated flow. As expected, the relative velocity scales with St as $St^{-1/2}$ in the limit $\tau_p \gg T_L$. The PP10 model with reasonable parameters provides an excellent fit to the simulation result for the 3D rms. The maximum relative speed at St_m is twice smaller than the rms velocity of the turbulent flow, indicating a factor of $\simeq 2$ overestimate by the commonly-used model of Volk et al. (1980) and its later developments (e.g., Markiewicz et al. 1991; Cuzzi & Hogan 2003; Ormel & Cuzzi 2007).

The rms relative speed of particles with $St \lesssim 6$ shows a r -dependence in the range $\eta/4 \lesssim r \lesssim \eta$. The dependence for the smallest particles ($St = 0.1 - 0.2$) in our simulated flow at $r < \eta$ was found to be slower than the linear scaling predicted by the Saffman-Turner formula, suggesting considerable contributions from the sling events or caustic formation. For larger particles with $St \gtrsim 6$, the backward separation at a friction timescale ago becomes insensitive to the initial distance r , and the rms relative speed is independent of r . It remains to be examined whether and at which scale the rms relative velocity of $St \lesssim 6$ particles would converge and become r -independent as $r \rightarrow 0$.

The rms relative speeds in the radial and tangential directions are nearly equal for all $St \gtrsim 0.1$ particles. For $St \ll 1$ particles, this is in contrast to the Saffman-Turner formula, which predicts the tangential rms is larger than the radial rms by $\sqrt{2}$. This near equality is due to the randomization of the relative velocity direction with respect to the particle separation \mathbf{r} , which is caused by the deviation of particle trajectories from the fluid elements and/or the stochastic backward separation of particle pairs.

In the distance range explored, we find an asymmetry in the relative speed of $St \lesssim 6$ particles: approaching pairs that may lead to collisions have a larger relative speed than separating ones. The asymmetry is related to the phenomenon of turbulent clustering. The asymmetry is expected to decrease with decreasing r , but it remains to be tested whether it completely vanishes as $r \rightarrow 0$.

4. The probability distribution function for the particle relative velocity is highly non-Gaussian, exhibiting extremely fat tails. For small particles with $St \lesssim 1$, the effects of the particle memory and the backward separation lead to a self-amplification starting at the far tails, corresponding to the effect of slings or caustic formation. As St increases, the amplification becomes stronger and proceeds toward the inner part of the PDF, causing an increase in the fatness of the overall PDF shape. On the other hand, as St increases above $\simeq 1$, the PDF shape becomes less fat. For the larger particles, the relative velocity samples the PDF, $P_u(\Delta u, \ell)$, of the flow velocity increment, Δu , at larger scales,

ℓ . As the fatness of P_u decreases with increasing ℓ , the PDF of $St \gtrsim 1$ particles keeps thinning with increasing St . At a particle distance of $r \simeq 1\eta$, the PDF shape is fattest at $St \simeq 1$, with a kurtosis of $\simeq 30$.

We identified two sources of non-Gaussianity for the particle relative velocity: the imprint of intermittency of the turbulent flow and an intrinsic contribution from the particle dynamics. We predicted a 4/3 stretch exponential PDF, $\propto \exp(-(|w|/\beta)^{4/3})$, for inertial-range particles in an exactly Gaussian velocity field with Kolmogorov scaling. This 4/3 stretched exponential is observed in the PDF tails of particles with $St \simeq St_m$ (or $\tau_p \simeq T_L$), confirming the validity of the physical picture of PP10.

Based on the PP10 picture and our simulation result for the PDF, the particle pairs at a give distance can be split into two types, namely, the continuous type and the caustic type (Wilkinson et al. 2006). The two types correspond to the inner part of the PDF that follows the flow velocity difference, and the outer PDF part that is affected by the particle memory and the backward separation, respectively.

The PDF of the particle collision velocity is expected to play a crucial role in the growth of dust particles in protoplanetary turbulence, as it determines the fractions of collisions resulting in sticking, bouncing and fragmentation. The relative velocity PDFs of $St \gtrsim 12.4$ particles already converge at $r \simeq \eta/4$. On the other hand, the PDFs of smaller particles show r -dependence at $r \gtrsim \eta/4$, and an appropriate extrapolation is needed for the application to dust particle collisions at $r \rightarrow 0$. The shape of the measured PDFs provides interesting clues for the collisional energy. For example, the PDF of the 3D amplitude of the relative velocity suggests much higher probabilities of extremely small and large collision speeds than estimated from a Gaussian PDF. Only for very large particles with $\tau_p \gtrsim 50T_L$ does the PDF approach Gaussian. The highly non-Gaussian nature of the relative/collision velocity needs to be incorporated into dust coagulation models for protoplanetary disks. Pushing the PDF toward smaller r and finally to $r \rightarrow 0$ will be pursued in a future work.

5. We computed the particle collision kernel from the simulation data using both spherical and cylindrical formulations. It was found that the two formulations give nearly equal predictions for all particles. Adopting the formulation of Falkovich et al. (2002) and Gustavsson and Mehlig (2011), we

calculated the contributions to the collision kernel from continuous and caustic particle pairs separately. We showed that, although amplified by the effect clustering, the collision kernel due to the continuous-type pairs decreases with r , and would vanish in the $r \rightarrow 0$ limit. Consistent with the theoretical prediction of Gustavsson and Mehlig (2011), the contribution to the normalized kernel by caustic pairs is found to be r -independent, and the convergence is reached at $r = \eta/4$. This caustic contribution is dominant at sufficiently small r , and can be used to estimate the collision rate of nearly point-like dust particles.

The caustic contribution to the collision kernel per unit cross section shows an abrupt rise as St increases toward 1, which may be viewed as an activation process corresponding to the rapid formation of caustics. As St increases from $\simeq 1$ to St_m , the normalized caustic kernel is roughly constant, increasing only slightly by 50%. It finally decreases as $St^{-1/2}$ for large particles with $\tau_p \gg T_L$. Coagulation models for dust particle growth need to incorporate these important features. We will provide fitting functions for the caustic collision kernel and the collisional energy as a function of St in a separate study.

In this work, we have focused on the monodisperse case with identical particles. A systematic analysis for the relative velocity of different particles will be conducted in a follow-up paper. Future simulations at higher resolutions will further improve our understanding of the problem. For example, a 1024^3 simulation would help verify the existence of the predicted $St^{1/2}$ scaling for inertial-range particles by various models, which is not yet confirmed numerically. We have only partially addressed the $r \rightarrow 0$ limit, necessary for the application to dust particle collisions. A computationally more demanding simulation with a larger number of inertial particles would allow us to examine the particle statistics at smaller scales. With such simulations and by isolating the caustic pairs from the continuous ones, we can systematically evaluate the collision rate and the PDF of the collisional energy at $r \rightarrow 0$. The results of these future studies will significantly improve the formulation of coagulation models to compute the dust particle evolution in protoplanetary disks.

We thank the referee, Alexander Hubbard, for an extensive report that helped us improve the paper, and Anders Johansen for useful discussions and for support with the Pencil code. PP is supported by the FP7-PEOPLE-2010-RG grant PIRG07-GA-2010-261359. The simulations were carried out on the NASA/Ames Pleiades supercomputer.

APPENDIX

A: SEPARATION OF TRACER PARTICLE PAIRS

Our model for the relative velocity of inertial particles depends on the particle pair dispersion backward in time (§3.2.3). We adopted a two-phase behavior, consisting of a ballistic and a Richardson phase. To constrain the Richardson constant, g , in the latter phase, we study the dispersion of tracer particles in our simulated flow, and take the measured value of g as a reference for inertial particles.

In Fig. 20, the three solid lines from bottom to top show the backward-in-time separation of tracer particle pairs with “initial” distance $r = 1\eta$, 2η and 4η , respectively. We subtracted r^2 from the separation variance, $d^2(\tau)$. The “initial” time is set to 0, and τ is negative for the backward separation. As seen in Fig. 20, the particle separation at small $|\tau|$ shows a ballistic behavior with $d^2(\tau) - r^2$ increasing as τ^2 . The physical origin of the ballistic behavior is that the velocity at which two tracer particles separate is determined by the flow velocity difference across the initial distance, r , and remains roughly constant before the particle distance becomes significantly larger than r . This ballistic phase of the tracer particles is physically different from that of inertial particles discussed in §3.2.3. For inertial particles, the duration and the separation speed of the ballistic phase depend on the particles’ memory timescale. But for tracer particles, the ballistic phase is determined purely by the initial distance. For $r \lesssim 4\eta$, the ballistic phase lasts for a few Kolmogorov timescales.

The Richardson separation behavior (the $|\tau|^3$ scaling) is observed at large $|\tau|$ after the particle separation enters the inertial range of the flow. In the bottom solid curve for $r = 1\eta$, a $|\tau|^3$ scaling exists in a very limited range. A rough estimate of the Richardson constant in that range gives $g \simeq 0.5$. Consistent with previous studies (e.g., Sawford et al. 2008), the time range that exhibits the Richardson scaling becomes broader as r increases to 4η . This allows a more accurate estimate of g , and we find $g \simeq 1.2$ for $r = 4\eta$, consistent with the experimental results of Berg et al. (2006). Similar to Sawford et al. (2008), the measured g has a dependence on r . If the inertial range of the flow is considerably broader and the Richardson behavior exists in a larger time range, the curves for different initial distances are expected to converge at sufficiently large time lags, with g eventually approaching a universal value.

The dashed line in Fig. 20 plots the forward-in-time pair dispersion of tracer particles at $r = 4\eta$. A comparison with the top solid line shows that the forward separation is slower than the backward separation. For $r = 4\eta$, g is estimated to be 0.5 in the forward separation, about twice smaller than the value (1.2) for the corresponding backward separation. This is consistent with the result of Berg et al. (2006). A physical explanation for the faster backward separation will be given in Appendix B. In our model for the relative velocity of inertial particles, it is the backward separation that is relevant, and the purpose of showing an example for the forward separation in Fig. 20 is to illustrate the difference between the forward and backward separations.

The Richardson constant, g , in the tracer-like phase of inertial particle separation may be different from tracers. However, it is reasonable to assume that g for the backward separation of inertial particles lies in a similar range. Like tracers, the value of g for inertial particles may also depend on the initial distance, r . In §6.1, we adjusted the value of g in our model to obtain best fits to the simulation results for the rms relative velocity at different r .

B: THE PDFS OF THE TURBULENT VELOCITY FIELD

In this Appendix, we analyze the probability distribution functions (PDF) of the flow velocity increments. We measure the PDFs, $P_l(\Delta u_r, \ell)$ and $P_t(\Delta u_t, \ell)$, of the longitudinal and transverse increments as a function of the length scale, ℓ . Similar to the computation of the structure functions in §4.2, the PDF measurement also uses the velocity

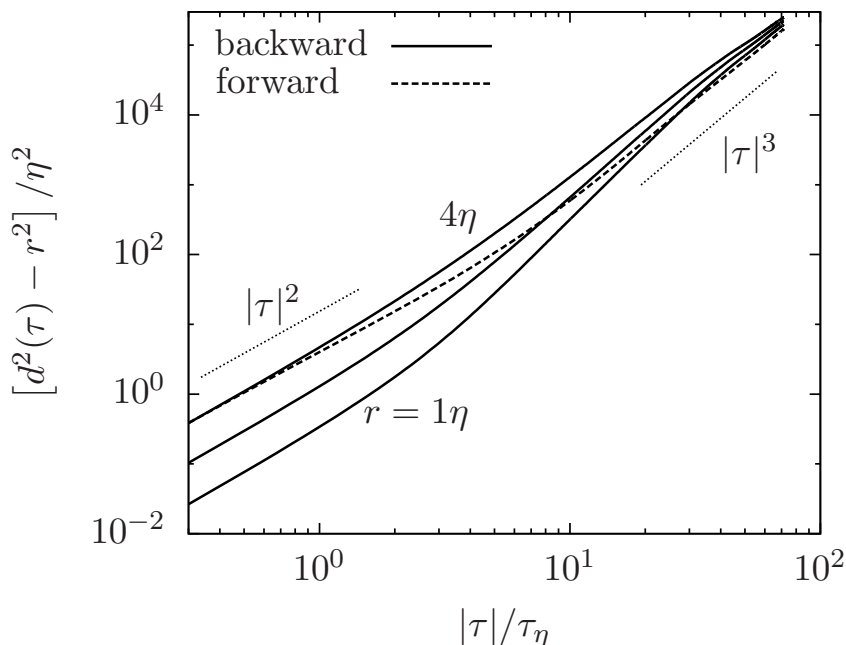


FIG. 20.— Separation of tracer particle pairs in our simulated flow. The time lag and the particle separation are normalized to Kolmogorov time and length scales. Solid lines from top to bottom correspond to the backward separation of particle pairs with “initial” distance $r = 1$, 2 and 4η , respectively. The dashed line plots the forward separation with $r = 4\eta$. The initial time is set to 0, and τ is negative (positive) for the backward (forward) separation. The separation shows a ballistic phase and a Richardson behavior at small and large $|\tau|$, respectively.

differences along the three directions of the simulation grid. The variances of $P_u(\Delta u_r, \ell)$ and $P_u(\Delta u_t, \ell)$ correspond to the longitudinal ($S_{\parallel}(\ell)$) and transverse ($S_{\text{nn}}(\ell)$) structure functions, which have been shown in Fig. 3 (see §4.2). Clearly, the PDFs are wider at larger scales. Also, $P_u(\Delta u_t, \ell)$ is wider than $P_u(\Delta u_r, \ell)$ because $S_{\text{nn}}(\ell) \geq S_{\parallel}(\ell)$ at all ℓ (see Fig. 3).

To better see the PDF *shape* as a function of ℓ , we normalized the PDFs at each scale to have unit variance. The radial and transverse velocity increments are normalized to their rms values, i.e., $\widetilde{\Delta u}_r(\ell) \equiv \Delta u_r(\ell)/S_{\parallel}^{1/2}(\ell)$ and $\widetilde{\Delta u}_t(\ell) \equiv \Delta u_t(\ell)/S_{\text{nn}}^{1/2}(\ell)$. The left panel of Fig. 21 shows the normalized PDF, $P_u(\widetilde{\Delta u}_r, \ell)$, of the radial increment. Except at the largest scales, the PDF is negatively skewed. For inertial-range scales, this can be understood from Kolmogorov’s 4/5 law, $\langle \Delta u_r(\ell)^3 \rangle = -\frac{4}{5}\bar{\epsilon}\ell$, which indicates a negative skewness for the PDF of Δu_r . The connection of the 3rd order moment of Δu_r to the energy dissipation rate suggests that the skewness originates from the dissipative nature of turbulence. The skewness of the PDF of Δu_r also provides an explanation for the faster backward separation found in Appendix A. The left and right tails of $P_u(\widetilde{\Delta u}_r, \ell)$ correspond to tracer pairs receding from each other backward and forward in time, respectively. The broader left tail of the PDF thus suggests that the backward separation of tracer particles is faster than the forward case. Unlike $P_u(\widetilde{\Delta u}_r, \ell)$, the PDF, $P_u(\widetilde{\Delta u}_t, \ell)$, of the transverse increment in the right panel is symmetric at all ℓ , as expected from statistical isotropy.

Both $P_u(\widetilde{\Delta u}_r, \ell)$ and $P_u(\widetilde{\Delta u}_t, \ell)$ are close to Gaussian at the largest scales, $\ell = 211\eta$ (1/4 box size, or 1.6 times the integral scale, L) and 422η (1/2 box size, or $3.1L$), of the simulated flow. This is consistent with the Gaussian 1-point statistics in fully developed turbulence. At smaller ℓ , the PDFs become non-Gaussian, and the tails keep getting fatter with decreasing ℓ , a phenomenon known as intermittency in turbulence theory (Frisch 1995). As mentioned in the text, we use the word “fat” (or “thin”) specifically for the shape of the PDF, while “broad” (or “narrow”) refers to the extension or width of the PDF. The smallest scale, 1.7η , in the figure corresponds to the size, Δx , of the computational cell. The shape of the normalized PDF is expected to remain unchanged once ℓ becomes smaller than $\sim \eta$. Physically, the viscosity acts to smooth the velocity field and makes it differentiable in the dissipation range, and thus the velocity increment at any scale $\ell \lesssim \eta$ is proportional to the local velocity gradient, whose PDF is fixed. In our simulation, the velocity field inside a computation cell is obtained by interpolation, and thus the PDF of the velocity difference below the cell size is controlled by the velocity gradient PDF at Δx . In §6.2, we showed that the trend of the PDF shape of the flow velocity difference with ℓ has interesting effects on the PDF of the relative velocity of inertial particles as a function of the particle inertia.

The tails of $P_u(\widetilde{\Delta u}_t, \ell)$ for the transverse increment can be approximately described by stretched exponentials, P_{se} (see eq. (34) in §6.2). At largest scales, $P_u(\widetilde{\Delta u}_t, \ell)$ are nearly Gaussian, and $\alpha = 2$. With decreasing ℓ , α decreases, corresponding to fatter tails. For example, the best-fit α for $P_u(\widetilde{\Delta u}_t)$ at $\ell = 26\eta$ is $\simeq 1$, and it further decreases to $\simeq 0.72$ at $\ell = 1.7\eta$. Due to the asymmetry of the radial PDF, $P_u(\widetilde{\Delta u}_r, \ell)$, one needs to obtain the fits separately for the left and right wings. Comparing the left wing of $P(\widetilde{\Delta u}_r, \ell)$ with $P_u(\widetilde{\Delta u}_t, \ell)$, we see that their shape has a similar level of fatness at the same scale ℓ . In fact, the best-fit α for the left tail of $P_u(\widetilde{\Delta u}_r, \ell)$ is very close to that for $P_u(\widetilde{\Delta u}_t, \ell)$.

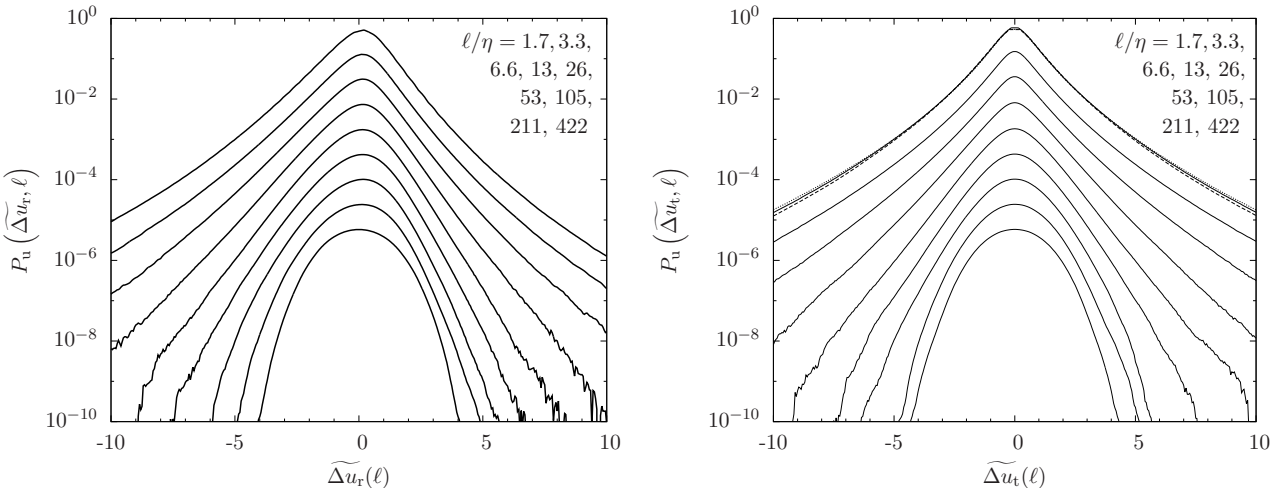


FIG. 21.— The normalized PDFs of the flow velocity increment in the radial (left panel) and transverse (right panel) directions at different length scales, ℓ . The normalized velocity increments are defined as $\widetilde{\Delta u}_r(\ell) \equiv \Delta u_r(\ell)/S_{\parallel}^{1/2}(\ell)$ and $\widetilde{\Delta u}_t(\ell) \equiv \Delta u_t(\ell)/S_{\text{nn}}^{1/2}(\ell)$. The top line in each panel plots the exact PDF at $\ell = 1.7\eta$ (the cell size), and, for clarity, the PDF at each larger ℓ is shifted downward by a factor of 4. Except at the largest scales, the PDF, $P_u(\widetilde{\Delta u}_r, \ell)$, of the radial increment has a negative skewness, whereas $P_u(\widetilde{\Delta u}_t, \ell)$ for the transverse increment is symmetric at all scales. The PDF tails are highly non-Gaussian at small scales. With increasing ℓ , the PDFs become less fat and finally approach Gaussian. In the right panel, the dashed and dotted lines for $\ell = 1.7\eta$ are the normalized PDFs of the transverse increment conditioned on $\Delta u_r < 0$ and $\Delta u_r > 0$, respectively. One may change the normalization of ℓ to the integral scale, L , using $L = 135\eta$.

We also find that the best-fit values of α for the left and right tails of $P_u(\widetilde{\Delta u_r}, \ell)$ are close, indicating that the two tails have a similar shape and differ only in the fluctuation amplitude.

To quantify the fluctuation amplitudes in the left and right wings of $P_u(\Delta u_r, \ell)$, we define the variances in the two wings as $\langle \Delta u_r^2 \rangle_- = \int_{-\infty}^0 \Delta u_r^2 P_u(\Delta u_r, \ell) d\Delta u_r / \int_{-\infty}^0 P_u(\Delta u_r, \ell) d\Delta u_r$ and $\langle \Delta u_r^2 \rangle_+ = \int_0^{\infty} \Delta u_r^2 P_u(\Delta u_r, \ell) d\Delta u_r / \int_0^{\infty} P_u(\Delta u_r, \ell) d\Delta u_r$. The definition of $\langle \Delta u_r^2 \rangle_{\mp}$ is similar to $\langle w_r^2 \rangle_{\mp}$ for the relative velocity of inertial particles (§6.1.3). We find that the ratio of $\langle \Delta u_r^2 \rangle_-$ to $\langle \Delta u_r^2 \rangle_+$ is $\simeq 1.47$ at $\ell = 1.7\eta$. This ratio decreases with increasing ℓ , and reaches unity at the largest scales. The variances of the left and right wings of $P_u(\Delta u_r, \ell)$ was used in the discussion on the relative velocity of approaching and separating particle pairs in the $St \ll 1$ limit (see §6.1.3). We also considered the PDF of Δu_t conditioned on the sign of Δu_r . We denote two conditional PDFs as $P_u(\Delta u_t | \Delta u_r \leq 0, \ell)$ and their variances as $\langle \Delta u_t^2 \rangle_{\mp} \equiv \int_{-\infty}^{\infty} \Delta u_t^2 P_u(\Delta u_t | \Delta u_r \leq 0, \ell) d\Delta u_t$. At $\ell = 1.7\eta$, $\langle \Delta u_t^2 \rangle_-$ is found to be larger than $\langle \Delta u_t^2 \rangle_+$ by 28%. In the right panel of Fig. 21, the dashed and dotted lines show the normalized conditional PDFs, $P_u(\Delta u_t | \Delta u_r < 0, \ell)$ and $P_u(\widetilde{\Delta u_t} | \Delta u_r > 0, \ell)$, at $\ell = 1.7\eta$. The conditional variances and PDFs of Δu_t are useful to understand the tangential relative velocity of approaching and separating particle pairs with $St \ll 1$ (§6.1.3 and 6.2.4).

REFERENCES

- Abrahamson, J. 1975, Chem. Eng. Sci. 30, 1371
Ayala, O., Rosa, B. & Wang, L.-P. 2008, New J. Physics, 10, 075016
Balkovsky, E., Falkovich, G., & Fouxon, A. 2001, Phys. Rev. Lett., 86, 2790
Bec, J., Biferale, L., Cencini, M., Lanotte, A. S., & Toschi, F. 2009, arXiv: 0905.1192v1 [physics.fly-dyn]
Bec, J., Biferale, L., Lanotte, A. S., Scagliarini, A., & Toschi, F. 2010, J. Fluid Mech., 645, 497
Berg, J., Luthi, B., Mann, J. & Ott, S. 2006, Phys. Rev. E., 74, 016304
Birnstiel, T., Ormel, C. W., & Dullemond, C. P. 2011, A&A, 525, 11
Blum, J. & Wurm, G. 2008, ARAA, 46, 21
Brandenburg, A. & Dobler, W. 2002, Computer Physics Communications, 147, 471
Chambers, J. E. 2010, Icarus, 208, 505
Chiang, E. 2008, ApJ, 675, 1549
Cuzzi, J. N. & Hogan R. C. 2003, Icarus, 164, 127
Cuzzi, J. N., Hogan, R. C., & Bottke, W. F. 2010, Icarus, 208, 518
Cuzzi, J. N., Hogan, R. C., Paque, J. M., & Dobrovolskis, A. R. 2001, ApJ, 546, 496
Cuzzi, J. N., Hogan, R. C. & Shariff, K. 2008, ApJ, 687, 1432
de Jong J., Salazar, J. P. L. C., Woodward, S. H., Collins, L. R., & Meng, H. 2010, Int. J. Multiphase Flow, 36, 324
Dullemond, C. P. & Dominik, C. 2005, A&A, 434, 971
Falkovich, G., Fouxon, A., & Stepanov, M. G. 2002, Nature, 419, 151
Falkovich, G., & Pumir, A. 2004, Physics of Fluids, 16, L47
Falkovich, G. & Pumir, A. 2007, J. Atmos. Sci. 64, 4497
Freytag, B., Allard, F., Ludwig, H.-G., Homeier, D., & Steffen, M. 2010, A&A, 513, A19
Frisch, U. 1995, Turbulence. The Legacy of AN Kolmogorov (Cambridge University Press, Cambridge)
Garaud, P., Meru, F., Galvagni, M., & Olczak, C. 2013, ApJ, 764, 146
Girimaji, S. S. & Pope, S. B. 1990, J. Fluid. Mech., 220, 427
Goldreich, P., & Ward, W. R. 1973, ApJ, 183, 1051
Gustavsson, K. & Mehlig, B. 2011, Phys. Rev. E, 84, 045304(R)
Gustavsson, K., Mehlig, B., Wilkinson, M. & Uski, V. 2008, Phys. Rev. Lett., 101, 174503
Gustavsson, K., Meneguz, E., Reeks, M. & Mehlig, B. 2012, New J. Physics, 14, 115017
Guttler, C., Blum, J., Zsom, A., Ormel, C. W., & Dullemond, C. P. 2010, A&A, 513, A56
Helling, Ch., Jardine, M. & Mokler, F. 2011, ApJ, 737, 38
Hockney, R. W., & Eastwood, J. W. 1981, Computer Simulation Using Particles, New York: McGraw-Hill
Hogan, R. C., & Cuzzi, J. N. 2001, Phys. Fluids, 13, 2938
Hubbard, A. 2012, MNRAS, 426, 784
Hubbard, A. 2013, MNRAS, 432, 1274
Ishihara, T., Gotoh, T. & Kaneda, Y. 2009, Annu. Rev. Fluid Mech., 41, 165
Johansen, A., Andersen, A. C., & Brandenburg, A. 2004, A&A, 417, 361
Johansen, A., Klahr, H., & Henning, Th. 2011, A&A, 529, A62
Johansen, A., Oishi, J. S., Low, M.-M. M., et al. 2007, Nature, 448, 1022
Johansen, A. & Youdin, A. N. 2007, ApJ, 662, 627
Johansen, A., Youdin, A., & Mac Low, M.-M. 2009, ApJ, 704, L75
Kolmogorov, A. N. 1962, J. Fluid. Mech., 13, 82
Kruis, F. E. & Kusters, K. A. 1997, Chem. Eng. Comm., 158, 201
Lee, A. T., Chiang, E., Asay-Davis, X., & Barranco, J. 2010, ApJ, 725, 1938
Lundgren, T. S. 1981, J. Fluid Mech. 111, 27
Markiewicz, W. J., Mizuno, H. & Voelk, H. J. 1991, A&A, 242, 286
Maxey, M. R. 1987, J. Fluid Mech., 174, 441
Monin, A. S. & Yaglom, A. M. 1975, Statistical Fluid Mechanics: Mechanics of Turbulence, vol. 2. MIT press.
Ormel, C. W., & Cuzzi, J. N. 2007, A&A, 466, 413
Ormel, C. W., Paszun, D., Dominik, C., & Tielens, A. G. G. M. 2009, A&A, 502, 845
Padoan, P., Jimenez, R., Nordlund, A. & Boldyrev, S., 2004, Phys. Rev. Lett. 92, 191102
Pan, L. & Padoan, P. 2010, J. of Fluid Mech., 661, 73 (PP10)
Pan, L., Padoan, P., Scalo, J., Kritsuk, A. G., & Norman, M. L. 2011, ApJ, 740, 21
Pan, L. & Scannapieco, E. 2011, Phys. Rev. E, 2011, 83, 045302(R)
Pinsky, M. B. & Khain, A. P. 1997, J. Aerosol Sci. 28, 1177
Pruppacher, H. R., & Klett, J. D. 1997, Microphysics of Clouds and Precipitation (Dordrecht: Kluwer)
Rossow, W. B., 1978, Icarus, 36, 1
Saffman, P. G. & Turner, J. S. 1956 J. Fluid Mech., 1, 16
Sawford, B. L. 1991, Phys. Fluids, 3, 1577
Sawford, Yeung & Hackl | saw08 Sawford, B. L., Yeung, P. K. & Hackl, J. F. 2008, Phys. Fluids, 20, 065111
Shaw, R. A. 2003, Annu. Rev. Fluid Mech., 35, 183
Squires, K. D., & Eaton, J. K. 1991, Phys. Fluids, 3, 1169
Sundaram, S., & Collins, L. R. 1997, J. of Fluid Mech., 335, 75
Volk, H. J., Jones, F. C., Morfill, G. E. & Roeser, S. 1980, A&A, 85, 316–325
Wang, L.-P., Wexler, A. S., & Zhou, Y. 1998, Phys. Fluids, 10, 2467
Wang, L.-P., Wexler, A. S., & Zhou, Y. 2000, J. of Fluid Mech., 415, 117
Weidenschilling, S. J. 1980, Icarus, 44, 172
Wilkinson, M. & Mehlig, B. 2005, Europhys. Lett., 71, 186
Wilkinson, M. Mehlig, B., & Bezuglyy, V. 2006, Phys. Rev. Lett., 97, 048501
Williams, J. J. E. & Crane, R. I. 1983, Int. J. Multiphase Flow, 9, 421
Windmark, F., Birnstiel, T., Ormel, C. W., & Dullemond, C. P. 2012, A&A, 544, L16
Yeung, P. K., Pope, S. B. & Sawford, B. L. 2006, J. Turbulence, 7, 58
Youdin, A. N. 2011, ApJ, 742, 38
Yuu, S. 1984, AIChE J., 30, 802
Zaichik, L. I., & Alipchenkov, V. M. 2003, Phys. Fluids, 15, 1776

- Zaichik, L. I. & Alipchenkov, V. M. 2009, *New J. Phys.*, 11, 103018
- Zaichik, L. I., Simonin, O. & Alipchenkov, V. M. 2003, *Phys. Fluids*, 15, 2995
- Zaichik, L. I., Simonin, O. & Alipchenkov, V. M. 2006, *Phys. Fluids*, 18, 035110
- Zhou, Y., Wexler, A. S., & Wang, L.-P. 2001, *J. Fluid Mech.*, 433, 77
- Zsom, A., Ormel, C. W., Dullemond, C. P., & Henning, T. 2011, *A&A*, 534, A73
- Zsom, A., Ormel, C. W., Güttler, C., Blum, J., & Dullemond, C. P. 2010, *A&A*, 513, A57